UNIVERSITÀ DEGLI STUDI DI MILANO

DIPARTIMENTO DI CHIMICA

Scuola di Dottorato in Scienze e Tecnologie Chimiche
Corso di Dottorato in Chimica Industriale – XXVI Ciclo
CHIM/02

TOWARDS THE PHOTOCATALYTIC PRODUCTION OF SOLAR FUELS

Nanostructured Titanium Dioxide for Photocatalysis & Photo-Electrochemistry

Tutor: Prof. Elena Selli
Coordinatore: Prof. Dominique Roberto

Tesi di Dottorato di:
Marco ALTOMARE
Matr. N° R09041

A.A. 2012-2013

Table of Contents

Abstract

In spite of many efforts given during the last decades to find new alternative photocatalytic materials, titanium dioxide (TiO_2) still represents the most widely employed semiconductor for photocatalytic applications, being photoactive, cheap, easily available, non-toxic, inert and, most of all, chemically stable. However, although exhibiting a powerful combination of extraordinary and attractive physico-chemical properties, it suffers from some issues, common to all semiconductors, related to the dynamic of the charge carriers. Precisely, trapping and recombination of valence band holes and conduction band electrons occur at a certain extent, anyway resulting in a drop of the process efficiency. Therefore, in view of limiting these detrimental phenomena, the charge transfer and the electric conductivity of a semiconductor can be enhanced, thus leading to an overall improvement of the photocatalyst performance.

In the first part of the work, homemade and commercial TiO_2 powders were studied as photocatalysts for different applications, including the liquid-phase photocatalytic oxidation of ammonia and formic acid, and the H_2 production through photocatalytic reforming of water-methanol vapors. In this context, a dopant (NH_4F) was used during the sol-gel synthesis of the semiconductor to stabilize the formation of the TiO_2 anatase phase (typically more active than rutile TiO_2 because of its higher electron mobility), especially when crystallization of the amorphous oxides was performed at high temperature (700 ˚C). Furthermore, the effects induced by noble metal nanoparticles deposition on TiO_2 anatase powders were also investigated. *In situ* electron spin resonance spectroscopy was employed to determine the amount of electrons and holes trapping centers formed under irradiation, in the absence and in the presence of noble metal co-catalysts at the surface of TiO_2, hence assessing also the ability of Au and Pt nanoparticles in trapping conduction band electrons. The results were of great usefulness not only to interpret the different H_2 production rates but also to understand some mechanistic aspects concerning the selectivity towards the different oxidation products in the methanol photo-steam reforming reaction.

In the second part of the work, the nanostructuring of the semiconductor was explored by fabricating TiO_2 nanotube arrays through electrochemical anodization. The anodic oxides were employed for both photocatalytic and photo-electrochemical H_2 production. In view of large-scale application, the anodization approach was studied on wide Ti substrate surfaces, in order to

assess the feasibility of the scale up. Moreover, TiO_2 nanotubes were also grown on Ti-based alloys. When fabricating the nanotubes under optimized conditions on Ti-Ta alloys, highly photoactive Ta-doped TiO_2 nanotubes were obtained, exhibiting superior water splitting ability. When anodizing Ti-Au alloys, the TiO_2 nanotubes resulted decorated with Au nanoclusters. These Au-decorated TiO_2 nanotube arrays were used as efficient photocatalyst for H_2 production from ethanol-water solutions. Finally, the fabrication of short TiO_2 nanotube layers exhibiting an unprecedented level of self-ordering was achieved through an innovative anodization approach. The highly ordered topography allowed the subsequent self-ordering dewetting of Au, leading to Au nanoparticles of controllable size and distribution. These short, Au nanoparticles-filled TiO_2 nanotubes exhibited advanced photoactivity ascribed to their reaction vessel-like geometry, fulfilling the requirements in terms of solid state charge carriers diffusion and liquid phase diffusion of oxidizing radicals.

1. Outline

1.1 Overview – TiO_2 Photo-Electrochemistry & Photocatalysis

Since the 1970s we have been observing an outburst of academic research concerning photocatalysis and photo-electrochemistry on metal oxide semiconductors. The explosion has been triggered by the report on the photo-electrochemical solar energy conversion in 1972 [1] and has shifted afterwards into the area of environmental photocatalysis, including wastewater purification and fabrication of self-cleaning/anti-fogging surfaces [2].

In this context, regardless of the huge extent of efforts given during the last decades to widen the range of exploitable materials, titanium dioxide (TiO_2) has been playing and still plays the role of the main character.

Although the "Honda-Fujishima Effect" became a well-known photo-electrochemical phenomenon and Fujishima and Honda's paper published in Nature in 1972 [1] had certainly addressed and fostered subsequent studies in the field, the first report (in the bibliographic sense) on photocatalysis dates back to 1921, when C. Renz reported on titania blackening upon sun light exposure in the presence of some organics (he also observed quite similar phenomena on other metal oxides) [3].

Interestingly, this and subsequent reports from those ages drew attention to photocatalysis by simply speculating around the nuisance involving the chalking of titania-based paints [3,4]. A recent review by A. Fujishima *et al.* [5] gives a thorough historical overview on TiO_2 photocatalysis.

However, though learnt by observing and interpreting practical daily-life issues, (titania) photocatalysis and related phenomena gradually transformed into a highly powerful, yet popular, tool for air and water purification and surface sterilization, besides being also an innovative approach to maintain the surfaces well clean. Along the way, photocatalysis has been applied not only for splitting water into hydrogen and oxygen [1], as already mentioned, but also to perform selective oxidation reactions in organic chemistry [6] and also for cancer treatment [7].

On the basis of such a broad range of applications, where photocatalytic phenomena have been successfully exploited, one might say by quoting Prof. B. Ohtani that "it would seem unnecessary to explain the importance of photocatalysis in both fundamental and application studies" [8].

1.2 The Current Scenario – TiO_2 is the Main Character

Needless to say, as the scientific community recognized the valuable physico-chemical properties of some metal oxide semiconductors and their extremely wide potentiality when used in photocatalysis and photo-electrochemistry, a huge number of materials have been investigated for an as-much-high number of light-assisted reactions, processes and applications. As a consequence, the number of scientific reports on photocatalysis has been exponentially increasing, hence approaching 25,000 in the Fall 2013 [9]. This extensive knowledge gained during the development of semiconductor photo-electrochemistry and photocatalysis explicitly pointed out that TiO_2 is (up-to-now) a unique material, which best behaves as the ideal photocatalyst for several aspects. For example, titanium dioxide is relatively inexpensive, easily available and able to act as a strong oxidizing/reducing agent, hence capable of splitting water into H_2 and O_2 upon light irradiation [2]. Yet, it's important to draw attention to another property of titania which is rather unmentioned, *i.e.*, its chemical and photo-(electro)chemical stability [10]. In fact, in view of a real application in the field of photocatalysis or photo-electrochemistry, all the other good properties of titania would not result exploitable (at all) if in the absence of its chemical stability.

1.3 The Aim of the Work – Tuning TiO_2 Properties

The acquired knowledge in photocatalysis and photo-electrochemistry not only proved titanium dioxide to be "the best one" (in comparison with other semiconductors) but also revealed its limits and, most importantly, the margins and directions where improvements can be gained (in terms of a better performance, so to speak). This has driven a quite big portion of the recent work in the field. In fact, TiO_2, as a semiconductor, intrinsically suffers from some issues related to the charge carrier transport (these issues pool titania together with all semiconductors).
Upon irradiation of the semiconductor with light of the proper wavelength, *i.e.*, sufficiently energetic to promote an electron from the valence band to the conduction band, the charge carriers can undergo different phenomena. The transfer of holes towards the surface of the semiconductor, for instance, would most likely result in the oxidation of either absorbed water molecules or organic species (this being indeed the desired goal). Otherwise, trapping

of the charge carriers or electron-hole recombination can occur, resulting in a drop in the efficiency of the process.
The rate of transfer, trapping and recombination of the charge carriers and, nevertheless, the electric conductivity of the semiconductor (the latter mainly addressed in view of photo-electrochemical applications) can be tuned in order to achieve a better performance of a given photocatalyst.
In this work, we explored different pathways to enhance either the conductivity of the semiconductor or the rate of charge carrier transfer. These approaches are namely: *i)* surface (and bulk) fluorination of TiO_2 powders; *ii)* metal and noble metal nanoparticles deposition on TiO_2 powders; *iii)* nanostructuring of TiO_2 (*i.e.*, fabrication of TiO_2 nanotubes).
TiO_2 powders have been studied as photocatalysts for different applications, including both downhill reactions, namely, ammonia and formic acid liquid-phase oxidation, and an uphill reaction, *i.e.*, the photocatalytic reforming of water-methanol vapors.
The nanostructuring of titania certainly represents the core of this work and, precisely, has to deal with the synthesis of titanium dioxide nanotubes by electrochemical anodization of titanium substrates. These nanotubes have been studied for both photocatalytic and photo-electrochemical water splitting.

1.4 References & Notes

[1] A. Fujishima, K. Honda, Nature 238 (1972) 37.
[2] A. Fujishima, T.N. Rao, D.A. Tryk, J. Photochem. Photobiol. C: Photochem. Rev. 1 (2000) 1.
[3] C. Renz, Chim. Acta 4 (1921) 961.
[4] A.E. Jacobsen, Ind. Eng. Chem. 41 (1949) 523.
[5] A. Fujishima, X. Zhang, D.A. Tryk, Surf. Sci. Rep. 63 (2008) 515.
[6] M.A. Fox, M.T. Dulay, Chem. Rev. 93 (1993) 341.
[7] A. Fujishima, J. Ohtsuki, T. Yamashita, S. Hayakawa, Photomed. Photobiol. 8 (1986) 45.
[8] B. Ohtani, J. Photochem. Photobiol. C: Photochem. Rev. 11 (2010) 157.
[9] Slightly more than 24,700 papers, dealing all with photocatalysis, are accessible on http://www.scopus.com (research made in October 2013; keyword “photocatalysis”). Interestingly, around 10,000 of these articles (more than one third of the total) were published in the last three years and around 21,000 (*ca.* 85% of the total) deal with titanium dioxide. This statistics clearly stresses that the interest in

photocatalysis is unfailingly increasing and TiO_2 undoubtedly covers the main role in this scenario. Nevertheless, regardless of the application, more than 40,000 scientific articles on TiO_2 have been published over the last ten years.

[10] U. Diebold, Surf. Sci. Rep. 48 (2003) 53.

2. Theoretical Background

2.1 Properties of Titanium Dioxide

According to U. Diebold, titanium dioxide is the most studied single-crystalline semiconductor in the field of surface science of metal oxides [1]. It is characterized by many favorable hence exploitable properties and, as a consequence, it is widely used as a photocatalyst [2,3], for Dye Sensitized Solar Cells (*DSSC*) [4], as a gas-sensor [5], as a white pigment for paints and cosmetic products [6,7], as a corrosion protective coating [8], for optical coatings [9], in ceramics and in electrochromic devices [10], for bone implants and as a food coloring agent (E171) [11].

Three are the main crystallographic phases of titanium dioxide [12], namely, rutile (*R*), anatase (*A*) and brookite (*B*). The thermodynamic stability of these types of structure depends on the size of titania particles [13,14]. Precisely, it has been shown that *R* is the most stable phase when particles are bigger than *ca.* 35 nm. On the other hand, *A* results stable for crystallites smaller than 11 nm. Finally, *B* has been found to be stable when the particles size ranges from 11 to 35 nm.

Among the three types of titania phases, mainly two, *i.e.*, *R* and *A*, have been studied and discussed herein. For both structures, the basic building block consists of a titanium atom surrounded by six oxygen atoms in a more or less distorted octahedral configuration. The two bonds between the titanium and the oxygen atoms at the apices of the octahedron are slightly longer and sizable deviations from a 90° bond angle are observed for anatase. For the sake of brevity, further details regarding structural features of these crystallographic phases are here omitted (recent reviews exhaustively examined titanium dioxide physico-chemical properties [1,15]).

Overall, the wide use of titanium dioxide, which is an n-type indirect band gap semiconductor, originates from its high chemical and photo(electro)-chemical stability, high photoactivity [16], favorable electron conduction and valence band positions and (relatively) convenient band gap width. A brief description of TiO_2 photocatalysis and photo-electrochemistry, along with the relative properties and theoretical concepts, is given in the following sections.

2.2 TiO_2 Photo-Electrochemistry

As mentioned along the Historical Overview (Section 1.1), the basis for photo-electrochemical (PEC) solar energy conversion were laid in the late 60s, when A. Fujishima, at that time a Japanese Ph.D. student working with Prof. Ken-ichi Honda at the University of Tokyo, started to investigate the photo-electrolysis of water using the energy of light [2]. The idea basically arose by analogy with natural photosynthesis where, in few words, the oxidation of water and the reduction of CO_2 to produce oxygen and carbohydrates, respectively, are carried out by capturing the energy of sunlight.

Generally, if a semiconductor is used as an electrode connected to another one (a platinum counter electrode, for instance) and both of them are immersed in the proper electrolyte, the photo-excitation of the semiconductor can generate electrical work through the external circuit and simultaneously drive chemical (red-ox) reactions at the surface of each electrode. A system built up with such a configuration (as the one sketched in Fig. 1(A)) is conventionally addressed as a PEC solar cell.

Titanium dioxide was the first material the researchers looked at when studying this newly invented approach. It has, in fact, extremely high stability in aqueous electrolytes and a sufficiently positive valence band (*VB*) edge for oxidizing water to oxygen.

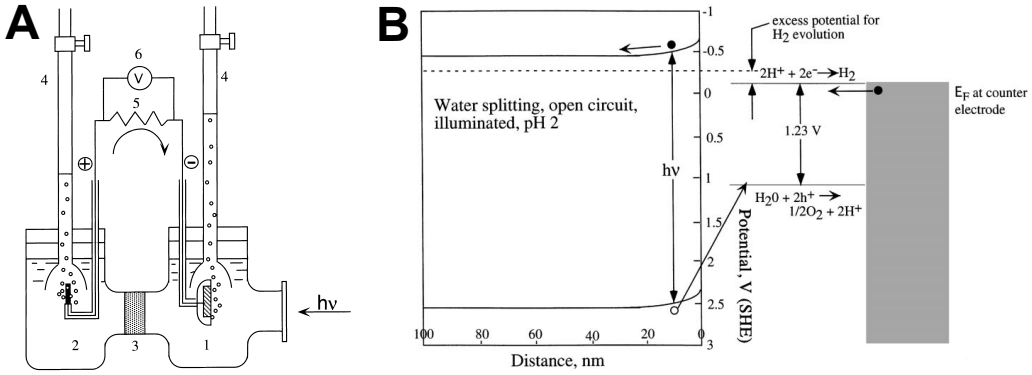

Figure 1 – (A) Schematic diagram of a PEC cell: (1) n-type TiO_2 electrode; (2) platinum counter electrode; (3) separator allowing ionic conductivity between the two-compartments; (4) burettes for collecting the evolved gas; (5) resistance and (6) voltmeter. (B) Schematic representation of PEC water electrolysis using an illuminated oxide semiconductor electrode. Open circuit (or small current), pH 2, illuminated conditions are shown for an oxide with an E_{CB} of − 0.65 V (SHE) and an E_{VB} of 2.35 V (SHE). With an open circuit, a small excess of potential (≈ 0.15 V) is available for H_2 evolution, assuming a reversible counter electrode. Both illustrations are taken from ref. [17].

During those first experiments, when the surface of the TiO_2 electrode was irradiated with light of wavelength shorter than ≈ 415 nm, photopromoted electrons flowed from the TiO_2 electrode to the platinum counter electrode through the external circuit. The direction of the current revealed that the oxidation reaction (oxygen evolution) was occurring at the TiO_2 electrode and the reduction reaction (hydrogen evolution) was at the Pt electrode. This fact demonstrated that water could be decomposed into oxygen and hydrogen, using UV–Vis light and without applying any external voltage, according to the following scheme:

Excitation of TiO_2 by light absorption: $TiO_2 + 2h\upsilon \rightarrow 2e^- + 2h^+$

O_2 evolution at the TiO_2 electrode: $H_2O + 2h^+ \rightarrow \frac{1}{2}O_2 + 2H^+$

H_2 evolution at the Pt electrode: $2H^+ + 2e^- \rightarrow H_2$

Overall reaction: $H_2O + 2h\upsilon \rightarrow \frac{1}{2}O_2 + H_2$

When a semiconductor electrode is in contact with an electrolytic solution, thermodynamic equilibration takes place at the interface. This results in the formation of a space-charge layer within a thin surface region of the semiconductor, in which the electronic energy bands are generally bent upwards in the cases of an n-type semiconductor, as shown in Fig. 1(B). On the contrary, the energy bands undergo downward bending for a p-type semiconductor. The thickness of the space-charge layer is usually of the order of 1–10^3 nm, this depending on the carrier density and dielectric constant of the semiconductor. If this electrode receives photons with energy greater than that of the material's band gap, E_G, e^--h^+ pairs are generated and separated in the space charge layer. In the case of an n-type semiconductor, the electric field existing across the space charge layer drives photogenerated holes toward the interfacial region (*i.e.*, the solid–liquid interface) and electrons toward the interior (*i.e.*, the bulk) of the electrode and, from there, to the electrical connection and external circuit (the reverse process takes place at a p-type semiconductor electrode) [18].
If the energy level of the *CB* is higher (*i.e.*, more negative on the electrochemical scale) than the hydrogen evolution potential, photogenerated electrons can flow to the counter electrode and reduce protons, resulting in hydrogen gas evolution without any applied potential. For this to occur, E_{CB} should be at least as negative as – 0.4 or – 1.2 V (*vs.* SHE) in acidic or in alkaline electrolytes, respectively. TiO_2 and some other metal oxide semiconductors (MOs), such as $SrTiO_3$, $CaTiO_3$, $KTaO_3$, Ta_2O_5 and ZrO_2, satisfy this requirement.

On the other hand, the employment of an external bias or a difference in pH between the anolyte (*i.e.*, the electrolyte in the anodic compartment) and the catholyte (*i.e.*, the electrolyte in the cathodic compartment) is required to achieve hydrogen evolution with materials with a less negative *CB* potential.
Another remarkable aspect is that, in view of an efficient solar light utilization, an ideal semiconductor would have a band gap of *ca.* 1.35 eV [19], thus allowing effective absorption of a wide portion of the solar light spectrum. However, even when photons are completely absorbed, the excess of energy of the photons ($E > E_G$) cannot be utilized in a simple single band-gap device, this because relaxation occurs in the upper excited states before charge transfer takes place. Therefore, a fraction of the photon energy is dissipated as heat.
Generally, when semiconductor electrodes are used for photo-assisted splitting of water, the bandgap should be at least 1.23 eV (*i.e.*, the equilibrium cell potential for water electrolysis at 25 ˚C and 1 atm), particularly considering the existence of polarization losses due to, for instance, oxygen evolution.
Regardless of the width of the band gap, another approach to successfully harvest solar light (*i.e.*, its visible light component) might involve the photosensitization of TiO_2. This approach has been intensively investigated with respect to regenerative PEC cells. In these cells, there is a redox couple in the electrolyte and its reduced form is oxidized at the TiO_2 photoanode, whereas the oxidized form is reduced at the counter electrode. The solar conversion efficiency of such devices has reached values of *ca.* 11 % [20,21]. However, this approach has a practical problem principally concerning the fact that photosensitizer dyes would be unstable under these conditions. In fact, they undergo actual degradation and the bigger the extent of dye decomposition, the larger the drop of efficiency of the PEC cell.
The idea of light-assisted water splitting has also been developed using the photocatalytic approach, *i.e.*, essentially using photo-electrochemistry without an external circuit. Conceptually, one can consider a noble metal nanoparticle on a titanium dioxide crystal as a small PEC cell where the anode and the cathode are short-circuited and spatially separated by a nanometric distance. Photocatalytic water splitting has been intensively studied on systems composed of Pt nanoparticles, as a cathodic co-catalyst, deposited on titania, the latter representing the anode [22]. The close relationship between TiO_2 photo-electrochemistry and photocatalysis is discussed in the following paragraphs section.

2.3 TiO_2 Photocatalysis

As pointed out by A. Heller [23], all of the extensive knowledge that was gained during the development of semiconductor photo-electrochemistry during the 1970s and 1980s has greatly triggered and assisted the development of photocatalysis. It turned out that TiO_2 is excellent, for instance, for the photocatalytic degradation of organic compounds. In other words, if one puts a photo-catalytically active TiO_2 powder into a shallow pool of polluted water and allows it to be illuminated with sunlight, the water will gradually become purified.

Ever since 1977, when S.N. Frank and A.J. Bard first examined the possibilities of using TiO_2 to decompose cyanide in water [24,25], there has been an increasing interest in titania-based environmental applications. These authors quite correctly pointed out the implications of their result in the field of environmental purification. Indeed, their prediction has been borne out, as evidenced by the extensive worldwide efforts given in this area [2,15,22,26].

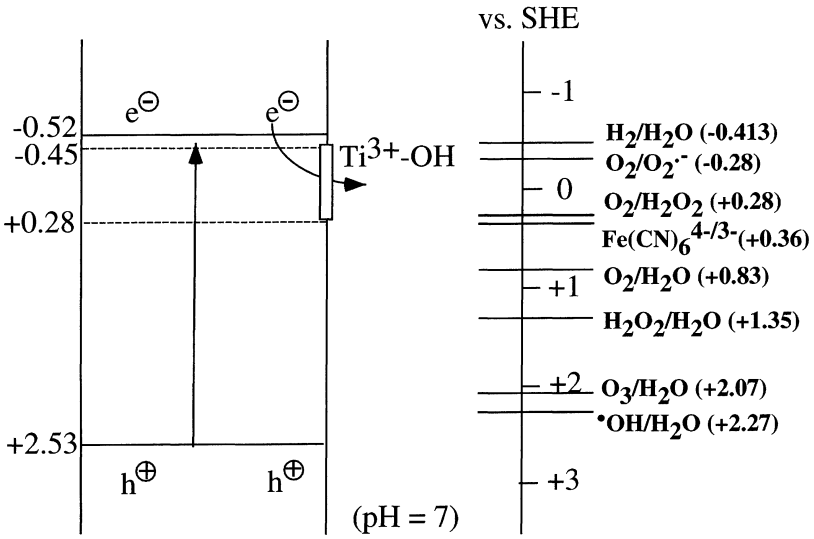

Figure 2 – Schematic diagram showing the potentials for various redox processes occurring at the TiO_2 surface at pH 7. The illustration is taken from ref. [17].

One of the most important aspects of environmental photocatalysis is the availability of a material such as titanium dioxide, which for several aspects is close to be an ideal photocatalyst. As already remarked, it is relatively inexpensive, chemically stable and the photogenerated holes are highly oxidizing. In addition, electrons are photo-promoted to a sufficiently negative potential to produce the superoxide radical anion ($O_2^{\bullet -}$) from O_2.

The energy band diagram of TiO_2 in a solution of pH 7 is shown in Fig. 2. The redox potential of photogenerated holes is + 2.53 V (SHE). Therefore these holes, through reaction with water molecules, can produce hydroxyl radicals ($^{\bullet}OH$), the redox potential of which is only slightly lower.
On the other hand, the redox potential of conduction band electrons is − 0.52 V. Although E_{CB} would in principle be negative enough to evolve hydrogen from water, conduction band electrons can become trapped and lose some of their reducing power. However, even after trapping, a significant number are still able to reduce O_2 to superoxide $O_2^{\bullet-}$ or to hydrogen peroxide H_2O_2.
Depending upon the experimental conditions, conduction band holes, $^{\bullet}OH$ radicals, $O_2^{\bullet-}$ and H_2O_2, all being extremely reactive species, can play an important role in the photocatalytic reaction mechanisms. In fact, most of the organic compounds can be fully oxidized by $OH^{\bullet}$ radicals to CO_2 and H_2O (therefore, such reactions can virtually be exploited for the oxidative destruction of any organic pollutant).
Moving back to the idea of short-circuited photo-electrochemical reactions, we can conceptually imagine O_2 as being reduced to either $O_2^{\bullet-}$ or H_2O_2 at a catalytic surface site. Here, a Pt microcrystallite deposited on the TiO_2 surface would represent an example of catalytic site for O_2 reduction. However, as titania is an n-type material, oxygen reduction can be supported even in the dark and by titania alone (*i.e.*, without noble metal deposits).
Since the anodic and cathodic currents must balance each other precisely on an electrically isolated TiO_2 particle, an oxidation reaction, carried out by valence band holes, is expected to occur in addition to oxygen reduction. This anodic reaction can be envisaged as the (direct) oxidation of an organic compound via holes. Since these are minority carriers, they would be in very low concentration in the dark but, on the contrary, would be in higher concentration under illumination.
In order to avoid the use of TiO_2 powder, which implies later separation from the liquid phase, various researchers began to work with TiO_2 particles immobilized in different ways, such as, for example, in form of thin films (one of the first reports on such approach is that of R.W. Matthews [27]).
Along the way, electrochemical anodization of titanium substrates was shown to be a straightforward approach for synthesizing nanostructured TiO_2 layers. Self-assembled TiO_2 architectures (such as nanopores, nanochannels, nanotubes and others [28,29]) could be fabricated by tuning the anodization conditions, as explained in detail in the following paragraphs (Section 2.4).

2.4 Electrochemical Anodization & TiO_2 Nanotubes

Some of the most important features of TiO_2 nanotubes have been briefly discussed, along with a short historical sequence of the groundbreaking achievements attained in the field. For the sake of conciseness and brevity, many other interesting and important aspects have been omitted. However, a thorough overview on the properties and applications of TiO_2 nanotubes can be found in several recent review papers [28,33].

The wide attention that titanium dioxide has received over the last forty years surely originated from its outstanding electronic properties that, as described in the previous sections, allow for a wide range of applications. However, not only the material as such, but also its structure and morphology were proved to have a considerable influence on its photocatalytic and photo-electrochemical performance.

In order to achieve a maximum turnover rate for the light-assisted reactions, a high surface area is desired, as for any process involving heterogeneous catalysis. This is usually achieved by using nanoparticles that are either suspended in the reaction environment or compacted to form a photo-electrode.

Despite of the broad use of titania nanoparticles, various one-dimensional and highly defined TiO_2 morphologies (such as nanotubes and nanowires) were explored over the past decades for their photocatalytic performance and, most of all, were found superior to nanoparticles in many cases [34]. Here, parameters that played a major impact were not only a high specific surface area but also better charge carrier transport and higher electron conductivity displayed by *1D* TiO_2 nanostructures. In fact, nanotubes and nanowires grant unidirectional percolation paths for photo-excited charge carriers, this being a potential approach to inhibit the electron–hole recombination process [28,30,35-38].

Nevertheless, a main practical drawback of any powder form (nanoparticles or loose assemblies of nanotubes, *etc.*) is that either the process has to be carried out in a suspension (which requires post-reaction separation of the loose material from the liquid medium), or the photocatalyst has to be immobilized on an inert substrate to allow ‘‘flow-through’’ reactions.

Since the late 90s, *1D* nanostructured oxides have been grown either by hydrothermal or by template-assisted methods that lead to nanotubes or nanowires powder [39,40]. Later, several advanced morphologies could be directly grown as aligned arrays, on a conductive substrate, such as wires [41], templated rods [42-46] or self-organized anodic structures that can be obtained as an oxide layer firmly attached to a titanium substrate (*i.e.,* the anodic layers are directly fabricated as back-contacted thin films) [28,30-

32,41-48]. Therefore, the latter structures can be straightforwardly used not only in static reactors but, most importantly, also as photo-anodes for electrochemically assisted photocatalytic processes (or, more generally, for any electrochemical application).

The first evidence of anodic titanium dioxide nanotubes dates back to 1999 when V. Zwilling *et al.* reported that anodization of Ti in a fluoride containing aqueous electrolyte resulted in the formation of self-organized TiO_2 nanotubes on the metal surface [49]

Such a combination of extremely ordered geometry and exciting properties not only has inspired the field of nanotechnology, but also triggered enormous efforts in physics, chemistry and materials science, hence generating an intense research activity that focused on the growth, modification, properties and applications of these *1D* nanostructures [28-32,47,48].

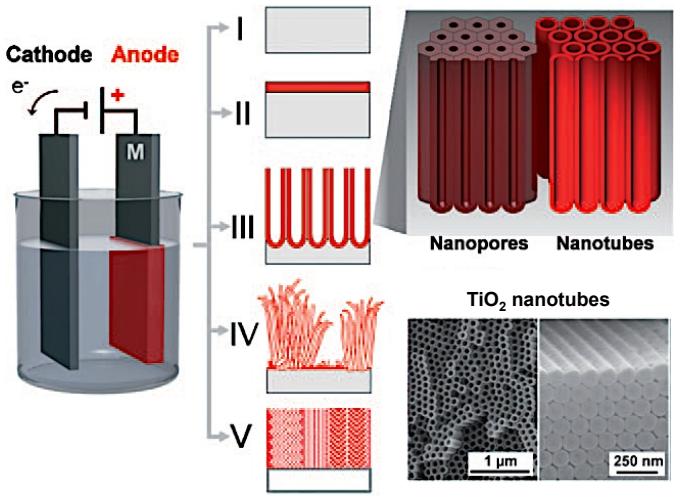

Figure 3 – The electrochemical anodization process and possible morphologies: *I)* electropolishing, II) formation of compact anodic oxides, III) self-ordered oxides (nanotubes or nanopores), IV) rapid (disorganized) nanotube formation, V) ordered nanoporous layers. The illustration is taken and adapted from ref. [28].

Self-organized nanotubes (or channels/pores) arrays can be attained by an optimized anodization process. When a titanium foil (or, more generally, a metal substrate) is positively biased at a sufficiently anodic voltage in an electrochemical configuration comprising the proper electrolytic solution (see Fig. 3), an oxidation reaction $M \rightarrow M^{n+} + ne^-$ will be initiated. Depending mainly on the electrolyte and the anodization parameters, essentially three reaction paths may exist: *I)* the M^{n+} ions are solvatized within the electrolyte, that is, the metal is continuously dissolved and corrosion or electropolishing of the metal substrate is observed; *II)* the M^{n+} ions formed react with O^{2-}

provided by H_2O in the electrolyte and form a compact *MO* layer (if the *MO* is not soluble in the electrolyte); *III)* under some electrochemical conditions, competition between solvatization and oxide formation is established, finally leading to porous *MO*. Under even more specific experimental conditions, a situation is established where self-organization during the growth of porous oxide takes place, allowing, for instance, the formation of highly ordered TiO_2 nanotubes. Furthermore, under some other specific conditions, disorganized but rapid growth of TiO_2 nanotube bundles or formation of thick sponge-like mesoporous layers can be observed (*IV* and *V* in Fig. 3, respectively).

The growth of the oxide can be monitored by recording the current *vs.* time profiles, hence obtaining curves as those reported as example in Fig. 4(A). After initiation, the growth of an anodic oxide layer is determined by the field-aided transport of mobile ions through the oxide. Depending on the migration rate of the involved ionic species (Ti^{4+}, O^{2-}), the growth of new oxide proceeds either at the interface between the metal and the oxide or at the interface between the oxide and the electrolyte. In principle, compact anodic TiO_2 layers may grow at both interfaces but, under most experimental conditions, the oxide actually grows at the metal–oxide interface.

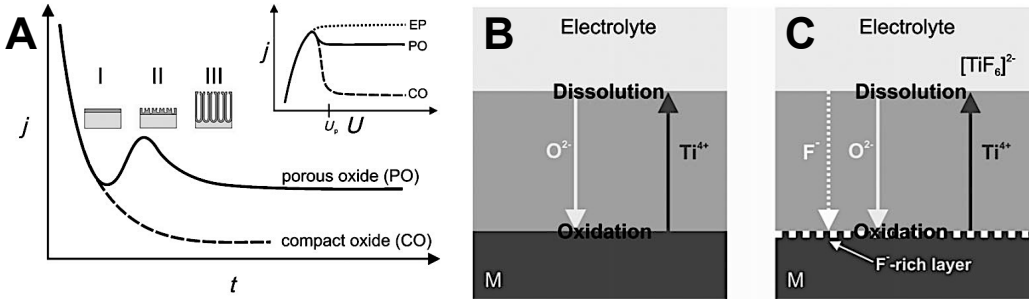

Figure 4 – (A) Typical current density–time (*J*–*t*) characteristics after a voltage step in the absence and presence (dotted and continuous line) of fluoride ions. The inset shows typical linear sweep voltammograms (*J*–*U* curves) for different fluoride concentrations resulting in the electropolishing of the metal (EP), a compact oxide (CO) or a porous nanotubular structure (PO); Schematic drawing showing field-aided transport of mobile ions through the oxide layers (B) in the absence and (C) in the presence of fluoride ions. The illustration is taken and adapted from ref. [28].

Under a constant voltage *U*, the field $F = U/d$ drops constantly since the thickness of the oxide *d* increases in the meanwhile, thus lowering the driving force for solid-state ion migration. The result is an exponential drop of the anodic current with time until the field effect is totally lost. At this point, a practically finite thickness is reached, the value of which mainly depends on the anodization voltage. For many transition metals (valve

metals), this final thickness is given by $d = fU$, where f is the so-called growth factor of the oxide (typically in the range of 2–4 nm V^{-1}).
The layer grown at the oxide-electrolyte interface consists of less-dense oxide containing oxyhydroxides, while the layer at the metal–oxide interface consists of dense and stable TiO_2 [50-53].
Clearly, the presence of fluorides in the electrolyte strongly affects the anodization process as fluorides form water-soluble species ($[TiF_6]^{2-}$). On one side, complexation occurs with Ti^{4+} ions that are ejected at the oxide–electrolyte interface after migration through the oxide film. On the other side, complexation occurs by chemical attack of the formed TiO_2.
Depending on fluoride concentration, three very different electrochemical characteristics can be obtained (as sketched in Fig. 4(A), inset). When the fluoride content is very low (≤ 0.05 wt%) or fluoride ions are completely absent, a stable compact oxide layer is formed even after anodizing the material at a voltage above U_p (*i.e.*, the threshold voltage for anodic oxide formation). If fluoride concentration is high (*ca.* 1 wt%), no oxide formation can be observed, since all formed Ti^{4+} ions immediately react with the abundant fluoride to form soluble $[TiF_6]^{2-}$. Afterwards, the reaction may be controlled by diffusion of $[TiF_6]^{2-}$ from the surface and electro-polishing of the sample occurs.
For intermediate fluoride concentrations, a competition between oxide formation and Ti^{4+} solvatization takes place and porous oxide or nanotube formation can be observed. A typical J–t curve for conditions that lead to nanotube formation is shown in Fig. 4(A). The curve shows three stages: *I)* in the initial stage of anodization the curve essentially follows the fluoride-free case and, if samples are removed from the electrolyte, a compact oxide layer is present. In stage *II)*, a current increase occurs and irregular nanoscale pores are initially formed that penetrate the initial compact oxide. The current increases as a direct consequence of the increase in reactive area. In step *III)*, the current drops again, as a regular nanopore or nanotube layer forms. The penetrated compact oxide (random pore layer or, more specifically, initiation layer) often remains as remnants that are frequently found after anodization at the tube tops [54]. After that the self-organization has occurred, the tube growth continues at steady current densities.
A consistent amount of work has been and is still dedicated to growing thick ordered TiO_2 nanotube layers. Clear evidence arisen during these studies is that the limit in thickness is undoubtedly ascribed to the oxide-growth/chemical-dissolution equilibrium that takes place during the steady-state step of the anodization process. In this view, J.M. Macak *et al.* achieved some crucial improvements to the geometry and thickness of the tubes. First, they demonstrated that the pH of the electrolyte plays a crucial role in

improving the tube layer thickness, that is, at neutral pH values, much longer tubes could be grown. Second, they also showed that in non-aqueous electrolytes, smooth tubes without sidewall inhomogeneity (ripples) could be grown up to a much higher aspect ratios, which exhibit a strongly improved ordering (using organic electrolyte systems, such as ethylene glycol, almost ideal hexagonally arranged tube layers can be grown to a thickness of several hundreds of micrometers) [55-57].

As for many applications crystalline titania is desired, it must be remarked that the anodization process typically yields amorphous oxides and, hence, amorphous TiO_2 nanotubes. However, the conversion of the anodic oxides into crystalline titania can be easily achieved by using an adequate annealing treatment. At temperatures above 280 °C, the onset of anatase formation is usually observed and, at higher temperatures, the anatase formation is accelerated. At temperatures higher than 500 °C, the rutile phase appears and, at even higher temperature, rutile formation is observed at a large extent up to the complete conversion of anatase into rutile. When annealing at temperatures higher than 700–800 °C, the structural integrity of the tubes is lost [33].

2.5 References & Notes

[1] U. Diebold, Surf. Sci. Rep. 48 (2003) 53.

[2] A. Fujishima, T.N. Rao, D.A. Tryk, J. Photochem. Photobiol. C: Photochem. Rev. 1 (2000) 1.

[3] A. Mills, R.H. Davies, D. Worsley, Chem. Soc. Rev. 22 (1993) 417.

[4] B. O'Regan, M. Grätzel, Nature 353 (1991) 737.

[5] U. Kirner, K.D. Schierbaum, W. Göpel, B. Leibold, N. Nicoloso, W. Weppner, D. Fischer, W.F. Chu, Sens. Actuat. B: Chem. 1 (1990) 103.

[6] C. Renz, Chim. Acta 4 (1921) 961.

[7] A.E. Jacobsen, Ind. Eng. Chem. 41 (1949) 523.

[8] E. Szalkowska, J. Gluszek, J. Masalski, W. Tylus, J. Mater. Sci. Lett. 20 (2001) 495.

[9] H. Selhofer, R. Müller, Thin Solid Films 351 (1999) 180.

[10] K. Yoshimura, T. Miki, S. Tanemura, J. Vac. Sci. Technol. A 15 (1997) 2673.

[11] K. Gotfredsen, A. Wennerberg, C. Johansson, L.T. Skovgaard, E. Hjørting-Hansen, J. Biomed. Mater. Res. 29 (1995) 1223.

[12] Other titanium dioxide structures exist as well. Cotunnite TiO_2, for example, has been synthesized at high pressure and is one of the

hardest polycrystalline materials known, as reported by L.S. Dubrovinsky et al., Nature 410 (2001) 653.
[13] H. Zhang, J.F. Banfield, J. Phys. Chem. B 104 (2000) 3481.
[14] M.R. Ranade, A. Navrotsky, H.Z. Zhang, J.F. Banfield, S.H. Elder, A. Zaban, P.H. Borse, S.K. Kulkarni, G.S. Doran, H.J. Whitfield, Proc. Natl. Acad. Sci. U.S.A. 99 (2002) 6476.
[15] A. Fujishima, X. Zhang, D.A. Tryk, Surf. Sci. Rep. 63 (2008) 515.
[16] Many scientific papers in the field of photocatalysis and photo-electrochemistry report on the "photoactivity" of a given material although in almost all cases the meaning is the same of that of absolute or relative reaction rate, as pointed out by B. Ohtani, J. Photochem. Photobiol. C: Photochem. Rev. 11 (2010) 157.
[17] A. Fujishima, D.A. Tryk, Photo-electrochemical Conversion, in: K. Honda (Ed.), Functionality of Molecular Systems, Vol. 2, Springer, Tokyo, 1999, pp. 196.
[18] A.J. Nozik, R. Memming, J. Phys. Chem. 100 (1996) 13061.
[19] S.M. Sze, Physics of Semiconductor Devices, Wiley, New York, 1981.
[20] M.K. Nazeeruddin, A. Kay, I. Rodicio, R. Humphry-Baker, E. Mueller, P. Liska, N. Vlachopoulos, M. Grätzel, J. Am. Chem. Soc. 115 (1993) 6382.
[21] M.K. Nazeeruddin, P. Pechy, M. Grätzel, Chem. Commun. (1997) 1705.
[22] D.A. Tryk, A. Fujishima, K. Honda, Electrochim. Acta 45 (2000) 2363.
[23] A. Heller, Acc. Chem. Res. 14 (1981) 154.
[24] S.N. Frank, A.J. Bard, J. Am. Chem. Soc. 99 (1977) 303.
[25] S.N. Frank, A.J. Bard, J. Phys. Chem. 81 (1977) 1484.
[26] M.R. Hoffmann, S.T. Martin, W. Choi, D.W. Bahnemann, Chem. Rev. 95 (1995) 69.
[27] R.W. Matthews, J. Phys. Chem. 91 (1987) 3328.
[28] P. Roy, S. Berger, P. Schmuki, Angew. Chem. Int. Ed. 50 (2011) 2904.
[29] D. Kowalski, D. Kim, P. Schmuki, Nano Today 8 (2013) 235.
[30] P. Roy, D. Kim, K. Lee, E. Spiecker, P. Schmuki, Nanoscale 2 (2010) 45.
[31] J.M. Macak, H. Tsuchiya, A. Ghicov, K. Yasuda, R. Hahn, S. Bauer, P. Schmuki, Curr. Opin. Solid. Stat. Mat. Sci. 11 (2007) 3.
[32] Y.C. Nah, I. Paramasivam, P. Schmuki, ChemPhysChem 11 (2010) 2698.
[33] I. Paramasivam, H. Jha, N. Liu, P. Schmuki, Small 8 (2012) 3073.
[34] J.M. Macak, M. Zlamal, J. Krysa, P. Schmuki, Small 3 (2007) 300.
[35] M. Law, J. Goldberger, P. Yang, Annu. Rev. Mater. Res. 34 (2004) 83.
[36] R. Jennings, A. Ghicov, L.M. Peter, P. Schmuki, A.B. Walker, J. Am. Chem. Soc. 130 (2008) 13364.
[37] M. Grätzel, Inorg. Chem. 44 (2005) 6841.
[38] K. Zhu, T.B. Vinzant, N.R. Neale, A.J. Frank, Nano Lett. 7 (2007) 3739.

[39] P. Hoyer, Langmuir 12 (1996) 1411.
[40] T. Kasuga, M. Hiramatsu, A. Hoson, T. Sekino, K. Niihara, Langmuir 14 (1998) 3160.
[41] Z.R. Tian, J.A. Voigt, J. Liu, B. Mckenzie, H. Xu, J. Am. Chem. Soc. 125 (2003) 12384.
[42] C.M. Lieber, Solid State Commun. 107 (1998) 607.
[43] C.N.R. Rao, M. Nath, Dalton Trans. (2003) 1.
[44] Y. Feldman, E. Wasserman, D.J. Srolovitz, R. Tenne, Science 267 (1995) 222.
[45] R. Tenne, L. Margulis, M. Genut, G. Hodes, Nature 360 (1992) 444.
[46] Y. Xia, P. Yang, Y. Sun, Y. Wu, B. Mayers, B. Gates, Y. Yin, F. Kim, H. Yan, Adv. Mater. 15 (2003) 353.
[47] A. Ghicov, P. Schmuki, Chem. Commun. (2009) 2791.
[48] S. Berger, R. Hahn, P. Roy, P. Schmuki, Phys. Status. Solidi B 247 (2010) 2424.
[49] V. Zwilling, E. Darque-Ceretti, A. Boutry-Forveille, D. David, M.Y. Perrin, M. Aucouturier, Surf. Interface Anal. 27 (1999) 629.
[50] L.V. Taveira, J.M. Macak, H. Tsuchiya, L.F.P. Dick, P. Schmuki, J. Electrochem. Soc. 152 (2005) B405.
[51] S.P. Albu, A. Ghicov, S. Aldabergenova, P. Drechsel, D. LeClere, G.E. Thompson, J.M. Macak, P. Schmuki, Adv. Mater. 20 (2008) 4135.
[52] H. Mirabolghasemi, N. Liu, K. Lee, P. Schmuki, Chem. Commun. 49 (2013) 2067.
[53] N. Liu, H. Mirabolghasemi, K. Lee, S.P. Albu, A. Tighineanu, M. Altomare, P. Schmuki, Faraday Discuss. (2013) DOI: 10.1039/C3FD00020F.
[54] R. Beranek, H. Hildebrand, P. Schmuki, Electrochem. Solid State Lett. 6 (2003) B12.
[55] J.M. Macak, K. Sirotna, P. Schmuki, Electrochim. Acta 50 (2005) 3679.
[56] J.M. Macak, H. Tsuchiya, P. Schmuki, Angew. Chem. Int. Ed. 44 (2005) 2010.
[57] J.M. Macak, H. Tsuchiya, L. Taveira, S. Aldabergerova, P. Schmuki, Angew. Chem. Int. Ed. 44 (2005) 7463.

3. Experimental Part & Analytical Instruments

3.1 Titanium Dioxide Powders

3.1.1 Sol-Gel Synthesis of NH_4F-Modified TiO_2 Powders

This section fully describes the synthesis of a series of NH_4F-modified TiO_2 powders that have been employed in the study discussed in Chapter 4. The powders were prepared by a sol-gel method [1,2], both in the absence and in the presence of NH_4F. Therefore, a reference material, labeled as S0, was prepared without any addition of NH_4F. On the other hand, modified photocatalysts were prepared by adding different amounts of NH_4F during the hydrolysis of the Ti precursor, *i.e.*, Ti(IV) tetraisopropoxide ($Ti\{OCH(CH_3)_2\}_4$). NH_4-modified samples are labeled herein as SX (*e.g.*, S5), with X indicating the specific NH_4F/Ti percent molar ratio used in the preparation. Three NH_4F amounts were used, namely, 5, 7 and 12 %.
As prepared samples were amorphous, so that annealing was performed to achieve full crystallization. The thermal treatment was carried out in a tubular furnace, at 700 ˚C, for 4 h under a controlled flow of synthetic air (20 vol% O_2 – 80 vol% N_2).
The so obtained powders underwent noble metal nanoparticles (NM NPs) photodeposition starting from 6 vol% methanol aqueous solutions, containing 3 g L^{-1} of the desired sample and the proper amount of NM precursor. $HAuCl_4$ and H_2PtCl_6 were used for gold and platinum nanoparticle deposition, respectively. The amount of NM precursor was calculated in order to obtain a nominal metal loading of 0.5 wt%. Such a loading was previously found to be optimal for improving the rate of formic acid (FA) photocatalytic mineralization, representing the best balance between the shielding effects induced by the presence of NM NPs on the surface of the powder, thus decreasing the fraction of light effectively absorbed by TiO_2, and their beneficial role in collecting conduction band electrons, hence reducing electron-hole recombination [3,4].
Au(III) and Pt(IV) photoreduction to Au^0 and Pt^0 NPs [5] was achieved by irradiating the suspensions with an immersion fluorescent, low pressure mercury arc lamp (Jelosil), emitting in the 300–400 nm range, with a peak of maximum emission at *ca.* 360 nm. Photodeposition lasted 2 h and was performed under nitrogen atmosphere.

NM-modified powders were recovered from the reaction suspension by using a rotavapor. The powders were afterwards washed, through washing-centrifugation cycles in water, until the complete removal of residual ions and organics was attained (precisely, the concentration of chloride anions was monitored by ionic chromatography after every cycle; the washing procedure was stopped when a [Cl^-] < 1 ppm was detected). The samples were dried overnight at 70 °C and stored in the dark, in a moisture-free container. These samples were labeled as NM/SX (*e.g.*, Pt/S5), where NM refers to either Au or Pt. Reference samples were also prepared, by using the same procedure aside from the addition of the NM precursor. These powders are labeled as R/SX (*e.g.*, R/S5), with R standing for "reference". The same method for NM NPs deposition was also employed to modify commercial TiO_2 P25 (Degussa-Evonik).
Inductively coupled plasma (ICP) analysis performed using a Thermo Electron ICAP 6300 instrument after microwave digestion of the photocatalysts in a 3:1 HCl/HNO_3 aqueous mixture, confirmed the effective and quantitative deposition of the noble metals.
All reagents were purchased from Aldrich and employed as received. Water purified by a Milli-Q water system (Millipore) was used throughout.

3.1.2 Preparation of Au & Pt/TiO_2 Anatase Powders

This section describes the preparation of Au and Pt/anatase powders that have been employed in the study discussed in Chapter 5.
Several different methods to load metal NPs onto TiO_2 powders, such as precipitation, impregnation, photoreduction (described in Section 3.1.1) and chemical reduction (with H_2 gas or $NaBH_4$) are reported in the literature. Among all these methods, the adsorption of NM ions onto the titania surface followed by reduction with $NaBH_4$ produces highly dispersed metal NPs in intimate contact with TiO_2 [3]. A commercial amorphous TiO_2 powder (NanoActive®, NanoScale Co., USA) was used as starting material. It was first kept at 200 ˚C under O_2 flow for 1 h. After cooling to room temperature, it underwent further oxidation in O_2 flow at 500 ˚C for 1 h. The sample obtained by this way is labeled herein as TiO_2-A.
Au- and Pt-modified TiO_2 photocatalysts were prepared as follows: 500 mg of TiO_2-A were suspended in 40 mL of H_2O and sonicated for 20 min. Then, a $HAuCl_4$ or H_2PtCl_6 water solution was added and the so obtained suspension was stirred for 30 min. Finally, a $NaBH_4$ solution (10 mg in 10 mL of H_2O) was added drop-wise under stirring and was allowed to react for 10 min. The product was then centrifuged, washed three times with H_2O and dried in *vacuum* (10^{-5} mbar). The so obtained samples are labeled herein as

Au/TiO_2-A or Pt/TiO_2-A, respectively. The nominal amount of metal loaded on TiO_2 was 1 wt% in both cases. An aqueous (40 mL) suspension of TiO_2-A (500 mg) was also treated with the $NaBH_4$ solution under conditions identical to those adopted for noble metal deposition, apart from the addition of the metal precursor, to produce a reference sample, labeled herein as TiO_2-Rf.
The actual Pt and Au loadings were determined by inductively coupled plasma – optical emission spectrometry (ICP-OES; ICAP 6300, Thermo Electron) after microwave digestion of the samples in a 3:1 HCl/HNO_3 solution. The measured Au and Pt loadings were 0.70 ± 0.02 and 0.64 ± 0.02 wt%, respectively.

3.1.3 Preparation of Metal-Loaded TiO_2 P25 Powders

This section describes the preparation of metal-loaded TiO_2 P25 powders that have been employed for the study discussed in Chapter 6. Preformed metal (Pt, Pd, Au and Ag) nanoparticles, stabilized by n-dodecyl trimethylammonium chloride, were deposited on TiO_2 P25 powders by means of a procedure already described in refs. [6-8]. The proper amount of metal precursor was dissolved in an aqueous solution containing the surfactant, with a surfactant-metal molar ratio of 40:1. Metal colloidal suspensions were obtained by adding an aqueous solution containing a large excess of $NaBH_4$. Then, an aliquot of the colloidal suspension was added under vigorous stirring to the required amount of P25 powders that was previously dispersed in water and sonicated. The powder was repeatedly washed with ultra-pure water (until the concentration of ionic species was lower than 1 ppm) and dried overnight in oven at 70 ˚C. This method for metal nanoparticles deposition avoids any structural modification of TiO_2 (*i.e.*, no change in SSA and phase composition [6,7]), because it is carried out in water at room temperature.
Nominal Pt and Pd NPs loadings ranged from 0.05 to 2.0 wt%, whereas Au and Ag loadings were fixed at 1.0 wt%. The samples are labeled herein as xM (*e.g.*, 0.05Pt), with M and x indicating the metal (Pt, Pd, Au or Ag) and the nominal weight percent loading (with respect to the weight of TiO_2), respectively. A reference sample, labeled herein as Blank, was prepared from TiO_2 P25 powders by following the same procedure except for the addition of the metal precursor.
$AgNO_3$ (Janssen Chimica), gold(III) chloride hydrate (≥ 99.8 %), palladium(II) sulphate (98 %) and chloroplatinic acid hydrate (~ 38 % Pt basis), all purchased from Sigma–Aldrich, were employed as metal precursors.

3.2 Titanium Dioxide Anodic Films

3.2.1 Fabrication of TiO_2 Nanotubes/Ti/Pt Photo-Electrodes

This section fully describes the fabrication of a series of TiO_2 nanotubes (NT) arrays that have been employed in the study discussed in Chapter 7. Self-assembled TiO_2 NT arrays were synthesized by following a procedure reported in ref. [9]. After a thorough washing and degreasing by sonication in acetone, methanol and water (10 min each), the titanium disks (0.5 mm thick, 40 mm in diameter) underwent anodization in a conventional two-electrodes electrochemical cell connected to a DC power supply (Long Wei, PS-305D) under a 30 V applied potential. The cell allowed the anodization, and hence the growth of NT, to occur only at one side of the Ti disk. Therefore, the side of the titanium disk in contact with the electrolytic solution and a platinum foil were used as the working and the counter electrode, respectively.

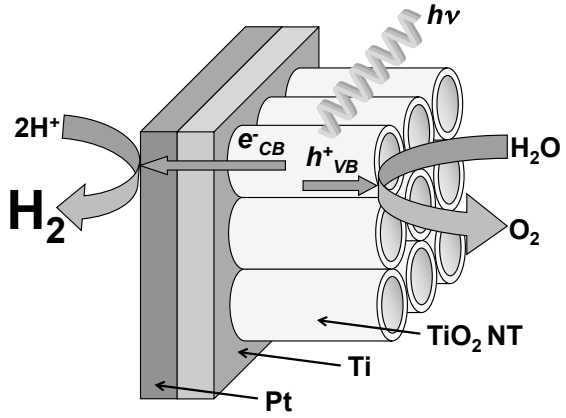

Figure 1 – Sketch of the TiO_2 NT/Ti/Pt photo-electrode showing the mechanism of separate H_2 and O_2 production through photocatalytic water splitting.

All experiments were carried out using a formamide-based electrolyte composed of 0.6 wt% NH_4F and 5 wt% H_2O. The anodization time was varied from 20 min up to 7 h, to attain NT layers characterized by different thickness. Then, the as-anodized oxides were soaked in ultrapure water, dried overnight in air at 70 °C and subsequently annealed in air at 450 °C for 3 h, with a heating ramp of 5 °C min^{-1}.

The fabrication of photo-electrodes to be employed in the photocatalytic cell for separate H_2 and O_2 production (fully described in Section 3.4.4) was completed by Pt deposition onto the non-anodized side of the titanium disks (see Fig. 1), after having ground the surface with sandpaper (grit 1500, *ca.*

12.6 μm) to remove any surface oxide layer and establish a better electric contact between the Pt layer and the Ti disks. Thin and homogeneous Pt layers were deposited by room temperature DC sputtering [10], performed at 12 V and 20 mA for 14 min.
Titanium disks (TI000420/15, ≥ 99.6 %) were purchased from Goodfellow. Formamide (≥ 99.5 %), NH_4F (≥ 98 %), acetone (≥ 99%) and methanol (≥ 99.9 %) were all Sigma–Aldrich chemicals.

3.2.2 Fabrication of Ta-Doped TiO_2 Nanotubes

This section describes the fabrication of pure and Ta-doped TiO_2 nanotubes arrays that have been employed in the study discussed in Chapter 8. The nanotube arrays were grown by a conventional electrochemical anodization treatment. All experiments were carried out in two-electrodes O-ring cell, with a platinum foil and a Ti (or Ti–Ta) substrate as counter and working electrode, respectively.
Prior to anodization, Ti foils (0.1 mm thick, 99.6+ % purity, Advent Research Materials, UK) were cut into samples (1.5 cm × 1.5 cm) and Ti–Ta alloys (Hauner Metallische Werkstoffe, Germany) were mechanically ground and polished (New Lam System). Afterwards, all substrates were cleaned by ultrasound treatment in acetone and ethanol (5 min each treatment), followed by rinsing with deionized water and drying in a stream of nitrogen. Electrolytes were prepared from ethylene glycol (Sigma–Aldrich, > 99.5 % purity) with NH_4F (0.5 wt%) and H_2O (3 vol%). All chemicals were reagent grade (Sigma–Aldrich). During the anodization, the DC voltage (provided by a Voltcraft VLP 2403 pro potentiostat) was raised from the open-circuit potential to the final potential (60 V). Anodic layers of different thickness were grown by varying the anodization time. Thicknesses of around 3, 7 and 12 μm were obtained after 6, 15 and 22 min, respectively, for pure TiO_2 nanotubes. The anodization time was then adjusted to yield Ta-doped TiO_2 NT with approximately the same tube length. To achieve this, longer anodization experiments were required and comparable thicknesses of the films were obtained on Ti–Ta alloys after 7, 16 and 60 min-long experiments. After anodization, the samples were soaked in ethanol overnight and subsequently dried in a stream of nitrogen.
Crystalline oxides were attained after annealing the anodic films in air at different temperatures (450, 550, 650 and 750 ˚C) for 1 h. The thermal treatment was performed with a rapid thermal annealer (Jipelec JetFirst100) with heating and cooling ramps of 30 ˚C min^{-1}.

3.2.3 Fabrication of Au-Decorated TiO_2 Nanotubes

This section describes the fabrication of Au nanoclusters-decorated TiO_2 nanotubes arrays that have been employed in the study discussed in Chapter 9. The nanotube arrays were grown by a conventional electrochemical anodization treatment. All experiments were carried out in a two-electrode O-ring cell, with a platinum foil and a Ti or Ti–Au substrate as counter and working electrode, respectively. The DC potential was provided by a LAB/SM1300 power supply.

For the fabrication of unmodified nanotubes layers, 0.125 mm thick Ti sheets (99.6 % purity, Advent Materials, UK) were used. Au-containing tubes, decorated with different loadings of Au, were grown by anodization of 0.02, 0.2 and 1 at% Au-Ti alloys (Hauner Metallische Werkstoffe, Germany). Prior to anodization, the samples were mechanically ground by using 4000 grit-sized SiC paper. Afterwards, the samples underwent polishing with a 9 μm polycrystalline diamond suspension and a mixture composed of non-crystallizing colloidal silica suspension and H_2O_2 (90:10 vol%). Then, the samples were degreased by sonication in acetone, ethanol and isopropanol, followed by rinsing with deionized water. Finally, the samples were dried with nitrogen gas.

Anodization experiments were performed in an ethylene glycol-based electrolyte, containing 0.2 M of HF and 1 M of H_2O, by applying 120 V for different times, in order to grow tubes of different lengths. After the anodization process, the samples were washed in ethanol and then dried in a nitrogen stream. To fully crystallize the materials, the samples were annealed at 450 and 650 °C, for 1 h in static air, using a rapid thermal annealer (Jipelec JetFirst100) with heating and cooling ramps of 30 ˚C min^{-1}.

3.2.4 Fabrication of Au Nanoparticles-Filled TiO_2 Nanocavities

This section describes the fabrication of Au nanoparticles (NPs)-filled TiO_2 nanocavities arrays that have been employed in the study discussed in Chapter 10. Ti foils (0.125 mm thick, 99.7 % purity, Goodfellow, England) were degreased by sonication in acetone, ethanol and deionized water and then were dried with nitrogen stream. Mixtures of hydrofluoric acid and phosphoric acid (Sigma-Aldrich) were used as electrolyte. Precisely, for the TiO_2 nanocavities arrays described in Chapter 10, H_3PO_4-based electrolytes containing 3 M of HF were used for all experiments.

A two-electrodes system composed of a platinum plate and a Ti foil as the counter and working electrode, respectively, was used for all anodization experiments. The potential was provided by a DC power supply Voltcraft

VLP 2403 pro potentiostat. A potential of 15 V was applied for 2 h, while keeping the electrolytic solution, *i.e.*, the H_3PO_4-HF mixture, at 80 ˚C. After anodization, the samples were rinsed with ethanol and then dried in nitrogen stream.
For Au films deposition on anodic TiO_2 substrates, a plasma sputter equipment (EM SCD500, Leica) was employed by operating at 15 mA and under *vacuum* condition (*ca.* 10^{-3} mbar of Ar). The dewetting step was performed by heat treatment carried out with a rapid thermal annealer (Jipelec JetFirst100) at 450 ˚C in air, with heating and cooling ramps of 30 ˚C min^{-1}.

3.3 Physico-Chemical Characterization

3.3.1 BET Analysis

The BET specific surface area (BET SSA) of the TiO_2 powders described in Section 3.1.1 and Chapter 4 (NH_4F-modified TiO_2 powders prepared by sol-gel method) and Section 3.1.3 and Chapter 6 (metal-loaded P25 powders prepared by surfactant-assisted method) was measured by N_2 adsorption–desorption at liquid nitrogen temperature in a Micromeritics ASAP 2010 apparatus, after out-gassing the samples in *vacuum* at 300 °C for at least 6 h.
Nitrogen physisorption measurements at 77 K for TiO_2 powders discussed in Section 3.1.2 and Chapter 5 (prepared by thermal oxidation of commercial amorphous titania powders) were carried out with a Quantachrome Autosorb-1 apparatus. Specific surface area, pore volume (desorption cumulative pore volume, DCPV) and pore size distribution (BJH method) were measured after evacuation at 200 ˚C for 16 h.

3.3.2 X-Ray Diffraction

X-ray diffraction (XRD) analysis was performed on both TiO_2 powders and anodic oxide thin films to assess the composition of the metal oxides in terms of crystallographic phase.
The X-ray diffraction patterns for TiO_2–based materials discussed in Section 3.1.1 and Chapter 4 (NH_4F-modified TiO_2 powders prepared by sol-gel method), Section 3.1.3 and Chapter 6 (metal-loaded P25 powders prepared by surfactant-assisted method) and Section 3.2.1 and Chapter 7 (TiO_2 NT/Ti/Pt photo-electrodes) were recorded with a Philips PW3020 diffractometer, by using the Cu Kα radiation (λ = 1.54056 Å). Quantitative

analysis to determine the crystallographic phase composition of the TiO_2 powders was made by the Rietveld refinement method, using the software "Quanto". Differently, concerning anodic TiO_2 films, diffraction patterns were recorder in the 20 ° < 2θ < 65 ° range with a total counting time of *ca.* 14 h. The diffraction data were collected by directly placing the samples, *i.e.*, the TiO_2 NT/Ti/Pt photo-electrodes, within the specimen compartment of the diffractometer. The crystallographic phase composition of the anodized films was determined by Rietveld refinement performed using the GSAS software [11]. Structural models for anatase TiO_2, rutile TiO_2 and metallic Ti phases were taken from refs. [13,14]. The background was subtracted using the shifted Chebyshev polynomials and the diffraction peak profiles were fitted with a modified pseudo-Voigt function. The generalized spherical harmonic (GSH) model implemented in GSAS was used to account for the contribution to the diffracted intensities given by preferential orientations.
The X-ray powder diffraction measurements of TiO_2 powders discussed in Section 3.1.2 and Chapter 5 (prepared by thermal oxidation of commercial amorphous titania powders) were performed using a Siemens D500 diffractometer operating at 40 kV and 30 mA, with a Cu Kα radiation source. Data were collected using a scan rate of 1.25° min^{-1} and a step size of 0.02 °.
X-ray diffraction analysis to determine the crystal structure of anodic oxides discussed in Section 3.2.2 and Chapter 8 (Ta-doped TiO_2 nanotubes), Section 3.2.3 and Chapter 9 (Au-decorated TiO_2 nanotubes) and Section 3.2.4 and Chapter 10 (Au NPs-filled TiO_2 nanocavities) were performed on an X'pert Philips PMD diffractometer, with a Panalytical X'celerator detector, using graphite-monochromated CuKα radiation (λ = 1.54056 Å).

3.3.3 UV-Vis Diffuse Reflectance Spectra

UV-Vis diffuse reflectance (DR) spectra were recorder to gain information about the optical properties of the TiO_2 powders, *i.e.*, light absorption threshold and possible visible light absorption features.
The spectra of TiO_2 powders discussed in Section 3.1.1 and Chapter 4 (NH_4F-modified TiO_2 powders prepared by sol-gel method) and Section 3.1.3 and Chapter 6 (metal-loaded P25 powders prepared by surfactant-assisted method) were collected with a Lambda 19 Perkin Elmer spectrophotometer, equipped with an integrating sphere. After acquisition, the reflectance data were converted into absorption (A) spectra (where A = 1 − R).
The UV–Vis DR spectra for TiO_2 powders discussed in Section 3.1.2 and Chapter 5 (prepared by thermal oxidation of commercial amorphous titania powders) were recorded with a Thermo Scientific Evolution 600 spectrophotometer, equipped with a diffuse reflectance accessory Praying–

Mantis sampling kit (Harrick Scientific Products, USA). A Spectralon® disk was used as reference material. All the powders were analyzed after careful grinding.

3.3.4 Scanning Electron Microscopy

Scanning electron microscopy (SEM) was performed on anodic TiO_2 thin films to evaluate the morphological and structural features of the nanosized materials studied herein.
A scanning electron microscope LEO 1430 (Zeiss) was employed to evaluate the effects induced by different anodization times on the morphology of TiO_2 NT arrays described in Section 3.2.1 and Chapter 7.
A field-emission scanning electron microscope (Hitachi FE-SEM S4800) was employed for the morphological characterization of all anodic oxides described in Sections 3.2.2, 3.2.3, 3.2.4 and Chapters 8, 9 and 10. The composition and chemical state of the anodic films described in Section 3.2.3 and Chapters 9 (Au-decorated TiO_2 nanotubes) were characterized by energy dispersive X-ray (EDX) analysis (EDAX Genesis) fitted to the Hitachi FE-SEM S4800.

3.3.5 Transmission Electron Microscopy

Transmission electron microscopy (TEM) was performed both on TiO_2 powders and anodic thin films to evaluate morphological and structural features of the nanosized materials studied herein.
High-resolution transmission electron microscopy (HRTEM) investigation of TiO_2 powders discussed in Section 3.1.1 and Chapter 4 (NH_4F-modified TiO_2 powders prepared by sol-gel method) and Section 3.1.3 and Chapter 6 (metal-loaded P25 powders prepared by surfactant-assisted method) was carried out with a JEM 3010 (JEOL) electron microscope operating at 300 kV, with a point-to-point Scherzer defocus resolution of 0.17 nm. Specimens for HRTEM analysis were sonicated in 2-propanol and then transferred as a suspension to a copper grid covered with a holey carbon film.
HRTEM and high-angle annular dark-field scanning transmission electron microscopy (HAADF-STEM) were employed to study the structural and morphological features of TiO_2 powders discussed in Section 3.1.2 and Chapter 5 (prepared by thermal oxidation of commercial amorphous titania powders) and Section 3.1.3 and Chapter 6 (metal-loaded P25 powders prepared by surfactant-assisted method). Morphology and size distribution of the metallic NPs supported on TiO_2 were investigated by using a Zeiss Libra 200FE instrument. The samples were finely ground using an agate

mortar and then dispersed in isopropanol by sonication. A drop of the suspension was deposited on a holey-carbon film supported on a copper 300 mesh grid. After solvent evaporation, TEM micrographs were taken spanning wide regions of all examined samples in order to provide a representative statistical map of the powders. The size distribution of Au and Pt NPs deposited on TiO_2 powders was determined by sampling 200 metallic NPs.
For morphological characterization of anodic films described in Section 3.2.3 and Chapter 9 (Au-decorated TiO_2 nanotubes), a transmission electron microscopy (Philips CM 30 T/STEM microscope) was used. Selected area diffraction (SAD) analysis was used for determining the crystalline structure of the layers.

3.3.6 X-ray Photoelectron Spectroscopy

X-ray photoelectron spectroscopy (XPS) analysis was performed both on TiO_2 powders and anodic thin films to assess the composition and chemical state of the samples.
The XPS analysis for TiO_2 powders discussed in Section 3.1.2 and Chapter 5 (prepared by thermal oxidation of commercial amorphous titania powders) were performed with a Omicron ESCA + spectrometer equipped with a spherical capacitor analyzer, 128 channel detector (channel-trons), monochromator, ion gun and an electron flood gun for charge neutralization. The monochromator had an illuminated area of about 1 mm in diameter. All measurements were done with monochromatic Al Kα radiation at 300 W. The accuracy of the reported binding energy (BE) was ± 0.1 eV. The sample analysis area was about 1 mm in diameter and the working pressure below 1×10^{-9} mbar. Detailed scans were recorded for the C 1s, O 1s, Ti 2p, Au 4f and Pt 4f BE regions. No further elements were detected. BE values were corrected by assigning the value of 284.6 eV to the C 1s peak of adventitious hydrocarbons. The analysis involved Shirley-type background subtraction and nonlinear least squares curve fitting, adopting Gaussian–Lorentzian peak shapes and peak area determination by integration. The atomic composition was evaluated from peak areas using Scofield sensitivity factors, based on the geometric configuration of the apparatus. The experimental uncertainty on the reported atomic composition values was below ± 5 %. Depth profiles were obtained by Ar^+ sputtering at 2.5 kV under an argon partial pressure of ~ 1×10^{-8} mbar over a 2 mm × 2 mm area. Under these conditions, the sputtering rate was 20 Å min^{-1}. For each sample, the chemical composition was checked at least over three different areas.

The composition and chemical state of the anodic films described in Section 3.2.3 and Chapters 9 (Au-decorated TiO_2 nanotubes) and Section 3.2.4 and Chapters 10 (Au NPs-filled TiO_2 nanocavities) were characterized by X-ray photoelectron spectroscopy (XPS) with an XPS instrument PHI 5600, US.

3.3.7 Electron Spin Resonance Spectroscopy

Electron spin resonance (ESR) spectroscopy was performed with the TiO_2 powders discussed in Section 3.1.2 and Chapter 5 (prepared by thermal oxidation of commercial amorphous titania powders) with a Bruker EMX spectrometer operating at the X-band frequency and equipped with an Oxford cryostat. The nanocrystals were charged into quartz glass tubes connected to both a high *vacuum* system and a controlled gas feed (O_2 or N_2 saturated with CH_3OH-H_2O vapors obtained by continuously bubbling the gas into a 20 vol% CH_3OH aqueous solution). Irradiation was performed by a UV–Vis 150 W Xe lamp (Oriel) on samples in the ESR cavity, through an optical fiber (50 cm length, 0.3 cm diameter). Additional experiments were carried out under the same conditions by filtering the UV portion of the lamp emission spectrum by a 420 nm cut-off filter. Samples were irradiated at 130 K either in *vacuum* or in the presence of 10 mbar of O_2 or N_2 saturated with CH_3OH-H_2O. The spectra were recorded at the same temperature in *vacuum* (10^{-5} mbar), before, during and after 30 min irradiation, using a modulation frequency of 100 kHz, modulation amplitudes of 2–5 G and a microwave power of 10 mW.
The g values were calculated by standardization with α,α'-diphenyl-β-picryl hydrazyl (DPPH). The spin concentration was obtained by double integration of the resonance lines, referring to the area of the standard Bruker weak pitch (9.7×10^{12} ± 5 % spins cm^{-1}). Accuracy on double integration was ± 15 %. The most sensitive part of the ESR cavity (1 cm length) was always kept filled. Spectra simulations and fitting were performed using the SIM 32 program [14]. For each sample, the absence of any signal before irradiation was checked.

3.3.8 Time of Flight – Secondary Ion Mass Spectrometry

The presence of Ta and its depth distribution in Ta-doped TiO_2 nanotubes (the fabrication, characterization and other related contents of which are reported in Section 3.2.2 and Chapter 8) were investigated by time of flight secondary -ion mass spectrometry (TOF-SIMS). The negative-depth profiles were recorded on an Ion-TOF TOF-SIMS V instrument operating in dual

beam mode. A pulsed 25 keV Bi^+ liquid-metal ion beam bunched down to < 0.1 ns and a 2 keV Cs^+ ion beam were used for spectrum generation and sputter removal of the samples, respectively. Poisson correction was employed and signals were identified according to their isotopic pattern and exact mass. The sputter rate, estimated by profilometry, was around 1 mm in 1600 s sputter time.

3.4 Photocatalytic Tests

3.4.1 Photocatalytic Degradation of Formic Acid

Formic acid (FA) photocatalytic degradation tests were carried out to assess the photocatalytic activity of NH_4F-modified TiO_2 powders, the synthesis and physico-chemical properties of which, along with their photocatalytic performance, are described and discussed in Section 3.1.1 and Chapter 4, respectively. FA photo-oxidation runs were performed under atmospheric conditions in a magnetically stirred, 60 mL cylindrical quartz reactor, placed within a homemade housing consisting of a black box mounted on an optical bench [3].

All the irradiated aqueous suspensions contained 0.1 g L^{-1} of photocatalyst and an initial FA concentration of *ca.* 1.0 x 10^{-3} mol L^{-1}. After a preliminary ultrasound treatment for 30 min, the suspensions were magnetically stirred in the dark for 15 min, to reach the adsorption-desorption equilibrium of the substrate on the photocatalyst surface before starting irradiation. 2 mL samples were withdrawn from the irradiated suspension after different time intervals during the runs and centrifuged. The liquid phase was analyzed by ion chromatography to determine the residual FA content. Ion chromatography was performed with a Metrohm 761 Compact IC instrument, equipped with a conductivity detector, after calibration for formate ions in the 0–50 ppm concentration range.

All kinetic runs were performed at natural pH, until *ca.* 70 % of the substrate was decomposed. Experiments were repeated at least twice, to check their reproducibility. During FA degradation, the pH of the suspensions increased from initial values around 3.7 to *ca.* 4.8 as a consequence of FA mineralization to CO_2 and H_2O (*i.e.*, the concentration of the acid, and thus also that of H^+ ions, decreases during irradiation).

3.4.2 H_2 Production by Methanol Photo-Steam Reforming

Methanol photo-steam reforming experiments were carried out to assess the photocatalytic activity of NH_4F-modified TiO_2 powders and Au and Pt/TiO_2 anatase powders. The synthesis and physico-chemical properties of the former series of samples, along with their photocatalytic performance, are discussed in Section 3.1.1 and Chapter 4, respectively, whereas, details and results concerning the latter are reported in Section 3.1.2 and Chapter 5.

Photoreactor set-up and experimental details adopted in these studies are described in detail in refs. [6,7,15,16]. Briefly, the photocatalyst bed was prepared by mixing 14 mg of photocatalyst powder with 3 g of 20–40 mesh (0.42–0.85 mm) quartz beads and 1.2 mL of ultra-pure water. The solid mixture was then dried in oven at 70 ˚C for 2 h. The so obtained photocatalyst bed was inserted in the photo-reactor, which consisted of a flat cylindrical Plexiglas cell frontally closed by a Pyrex glass optical window (nominal irradiation surface *ca.* 20 cm^2).

The photoreactor was connected to a recirculation, stainless steel apparatus, containing a N_2 gas bubbling system filled with a 20 vol% CH_3OH aqueous solution and kept at 30 ˚C (precisely, the methanol molar fraction in the liquid phase, *x*, was 0.10). The gas stream from the bubbling system was therefore a N_2 stream saturated with CH_3OH and H_2O vapors. This gas stream was conveyed to the photocatalyst bed within the reactor. Upon light activation of the photocatalyst, methanol and water were overall converted into CO_2 and H_2, according to a simplified reaction as follows: $CH_3OH + H_2O \rightarrow CO_2 + 3\ H_2$.

Prior to any run, the whole setup was thoroughly flushed with an inert gas, *i.e.*, N_2, in the dark for 30 min, in order to remove any trace of oxygen. The photocatalyst bed was irradiated for either 6 (when testing bare TiO_2 powders) or 2 h (for noble metal-modified samples). In the latter case, three consecutive irradiation cycles were performed with each photocatalyst bed, with 30 min of N_2 purging (in the dark) between each irradiation cycle. All kinetic tests were repeated three times.

The amount of hydrogen produced under irradiation and accumulated in the inert gas (along with the other photoproduced gas-phase species, *e.g.*, CO and CO_2) was determined by an on-line Agilent 6890 N gas-chromatograph, employing N_2 as carrier gas, equipped with two columns (HP-PlotU and Molesieve 5A), two detectors (thermo-conductivity and flame ionization) and a Ni-catalyst kit for CO and CO_2 methanation.

The irradiation source, always switched on 30 min prior to the beginning of the run, was a Xenon arc lamp (LSH302 LOT Oriel, 300 W), placed at 13 cm from the reactor, emitting in the UV–Vis range (solar simulator) with a full

irradiation intensity of 6.0×10^{-8} Einstein s^{-1} cm^{-2} on the reactor, as determined by ferrioxalate actinometry at 35 ˚C. Its constancy was checked by means of a UVA lux-meter.

During the runs, H_2, CO_2, and CO were produced and accumulated at constant rate in the recirculating gas phase [6,7,15,16]. Therefore, their production rate can be expressed in terms of zero-order rate constant. The gas-phase concentration of formaldehyde and other minor by-products remained almost constant at the exit of the photoreactor, this because they accumulated in the liquid solution (as they are water-soluble). Their average production rate could thus be evaluated from their amount in the aqueous solution at the end of the runs, divided by the overall irradiation time.

The reactor temperature during irradiation was 30 ± 2 °C. The absolute pressure was 1.2 bar at the beginning of the runs and slightly increased during irradiation, due to the accumulation of gas phase products.

A recent systematic investigation on the photo-steam reforming reaction [3] evidenced that methanol undergoes full oxidation to CO_2 through the formation of formaldehyde and formic acid as intermediate species. Also CO, CH_4, methyl formate, dimethyl ether and acetaldehyde were identified as minor products. The distribution of the products (*i.e.*, the selectivity) could be tuned by changing the methanol molar fraction *x* in the liquid solution, thus by changing the partial pressure of methanol and water in the vapor phase that fed the photoreactor. For all experiments, *x* was fixed at 0.1 as standard condition, this value representing a good compromise between a high rate of H_2 production and high selectivity to CO_2, as observed by G.L. Chiarello *et al*. [3].

3.4.3 Photocatalytic Degradation of Ammonia

Ammonia photo-oxidation experiments were carried out to assess the photocatalytic activity of different commercial TiO_2 photocatalysts (used as received) and metal-loaded TiO_2 P25 powders. For the latter series of materials, *i.e.*, metal-loaded P25 powders, synthesis and physico-chemical properties, along with their photocatalytic performance, are discussed in Section 3.1.3 and Chapter 6, respectively.

The photocatalytic reactor and analytical methods are described in detail in refs. [17,18]. The experimental apparatus consisted of a cylindrical Pyrex batch vessel (1100 mL) containing an immersion 25 W UVA mercury arc lamp (HG100, Jelosil), emitting in the 310-400 nm range ($\lambda_{max} \sim 365$ nm). The irradiation intensity within the photoreactor was 1.69×10^{-6} Einstein s^{-1}, according to ferrioxalate actinometry. The temperature of the suspensions within the photoreactor was kept constant at 30 ˚C by means of

an external cooling-water jacket. During the runs, artificial air (20 % O_2 and 80 % N_2), pure O_2 (99.9995 %), pure N_2 (99.9999 %) or a 10 % N_2O-He gas mixture were continuously bubbled from the bottom of the photoreactor. The flow rate of the gas stream was controlled by means of mass flow meters (5810 N, Brooks Instruments).

Once prepared, the TiO_2 aqueous suspensions were kept for 15 min in an ultrasonic bath. After ammonia addition and pH adjustment (if necessary, by addition of small volumes of concentrated KOH or $HClO_4$ solutions), the suspensions were stirred in the dark until a stable pH was reached (5 min were needed for pH around 10.5). The lamp was always switched on 15 min before starting the runs, in order to attain a constant intensity of light emission. All photocatalytic runs lasted 6 h and most of the photocatalysts were tested at least two times under identical conditions, giving reproducible results (uncertainties below 5 % in terms of concentration values). The pH of the suspension was measured at the beginning and at the end of each run. The suspensions, containing amounts of semiconductor powder ranging from 0.05 to 0.6 g L^{-1}, were constantly stirred during irradiation and 10 mL samples were withdrawn from the reactor, through a rubber septum, at regular time intervals, by using a syringe. The samples were immediately centrifuged at 3000 rpm for 30 min (EBA 20, Hettich Zentrifugen).

The concentration of NH_3, NO_2^- and NO_3^- in the aqueous phase was determined by ion chromatography. For ammonia determination, 5 mL of the withdrawn and centrifuged sample were diluted 1:10 with a 5 mM H_3PO_4 aqueous solution, this to ensure the full conversion of NH_3 into non-volatile NH_4^+. Ion chromatography analyses were performed with a Metrohm 761 Compact ion chromatograph, with conductivity detector, equipped with a 20 µL loop. A Metrosep C2 150 4 mm × 150 mm cation analytical column (eluent: 5 mmol L^{-1} H_3PO_4 aqueous solution, flow rate 1 mL min^{-1}) was employed for NH_4^+ determination. A Metrosep A Supp 4 4 mm × 250 mm anion analytical column was used for measuring the concentration of NO_2^- and NO_3^- (eluent: 1.8 mmol L^{-1} Na_2CO_3 and 1.7 mmol L^{-1} $NaHCO_3$ aqueous solution; flow rate 1 mL min^{-1}; electrochemical suppressor: 50 mmol L^{-1} H_2SO_4 aqueous solution). The amount of NO_2^- and NO_3^- could not be evaluated when performing the photocatalytic runs in the presence of ClO_4^- anions (originated from dissociation of $HClO_4$, added to adjust the pH), because of peak overlapping issues.

The calibration of the ion chromatograph was regularly checked using a Primus Fluka certified Multianion Standard Solution. Four-points calibration curves in the 0.1-10 ppm concentration range were obtained using aqueous

NH_4Cl, $NaNO_2$ and $NaNO_3$ standard solutions. The Metrohm IC Net 2.3 software was used for calibration and peaks integration.

$[N]_i$ (ppm)	pH	Air flow rate (mL min^{-1})	Stripped NH_3 (%)
100	10.5	50	0.6
100	10.5	100	1.8
100	10.5	150	2.8
100	3.5	150	-
100	6.5	150	-
100	7.5	150	-
100	11.5	150	2.9
100	12.5	150	3.3
1000	10.5	150	4.0

Table 1 – Amount of ammonia (%) stripped after 6 h from irradiated aqueous suspensions containing 0.1 g L^{-1} of TiO_2 P25 and different initial concentration of nitrogen $[N]_i$, at different initial pH and under different air flow rate.

Ammonia solutions containing 100 and 1000 ppm of nitrogen (*ca.* 130 and 1300 ppm of NH_4^+, respectively) were prepared from a 28-30 wt% NH_3 stock solution (Sigma–Aldrich). All other chemicals were also purchased from Sigma–Aldrich. All solutions were prepared using ultra-pure water (18.2 MΩ cm), supplied by a Millipore Direct-Q 3 water purification system. The amount of ammonia stripped by gas bubbling through the suspensions during the photocatalytic runs was evaluated by conveying the gas stream from the photoreactor into a 5 mM H_3PO_4 aqueous solution (*i.e.*, an acidic trap to collect ammonia within the gas stream). The ammonium content of the trap was analyzed by ion chromatography at the end of the runs. As shown in Table 1, the amount of stripped ammonia varied with its initial concentration within the suspension, with the pH and with the flow rate of the bubbling gas. The ammonium content of the trap was accounted for when evaluating the photocatalytic activity, as shown in Eq. 1-3. The outlet gas stream from the trap was analyzed in *continuum* by a photo-acoustic spectroscopy detector (Multi-Gas Monitor Type 1302 Innova, Bruel & Kjaer) to check the effective total removal of ammonia by the H_3PO_4 trap and to exclude that nitrogen-containing gaseous species other than N_2, such as NO, NO_2 and N_2O, were produced during the runs.

The percent conversion of ammonia, X_{NH3}, and the selectivity S_Y toward the nitrogen-containing photo-oxidation products (Y = NO_2^-, NO_3^- and N_2) were calculated from the moles of NH_3 initially present in the suspension, $n_{NH3,i}$, the moles of NH_3, NO_2^- and NO_3^- at the end of the run, $n_{NH3,f}$, $n_{NO2\text{-}f}$ and $n_{NO3\text{-}f}$, respectively, also taking into account the amount of stripped ammonia $n_{NH3,str}$, as follows:

$$X_{NH_3} = \frac{n_{NH_3,i} - n_{NH_3,f} - n_{NH_3,str}}{n_{NH_3,i}} \times 100 \qquad (1)$$

$$S_{NO_2^-} = \frac{n_{NO_2^-\,f}}{n_{NH_3,i} - n_{NH_3,f} - n_{NH_3,str}} \times 100 \qquad (2)$$

$$S_{NO_3^-} = \frac{n_{NO_3^-\,f}}{n_{NH_3,i} - n_{NH_3,f} - n_{NH_3,str}} \times 100 \qquad (3)$$

$$S_{N_2} = 100 - S_{NO_2^-} - S_{NO_3^-} \qquad (4)$$

The selectivity to molecular nitrogen S_{N2} was calculated form the total nitrogen mass balance (Eq. 4), after having verified (by photo-acoustic spectroscopy) that no gaseous NO_x species were produced during the runs.

3.4.4 Separate H_2 & O_2 Photocatalytic Production

Experiments of separate H_2 and O_2 photocatalytic production were carried out to assess the photocatalytic activity of TiO_2 NT arrays, the synthesis and physico-chemical properties of which, along with their photocatalytic performance, are described and discussed in Section 3.2.1 and Chapter 7, respectively.

The TiO_2 NT/Ti/Pt photo-electrodes were tested in a two-compartment photocatalytic Plexiglas cell, fully described in ref. [10], allowing the separate evolution of pure hydrogen and oxygen from aqueous solutions. The two-compartments of the cell were separated by the photo-electrode and filled with 1.0 M NaOH and 0.5 M H_2SO4 aqueous solutions, so that the anodic oxide was in contact with the alkaline solution, whereas the Pt-coated side faced the acidic electrolyte. A chemical bias (*i.e.*, ΔpH) was therefore generated across the two compartments to assist electron transfer from the TiO_2 NT arrays toward the Pt-coated side of the photo-electrode. Moreover, a cation exchange membrane (Nafion 117) was placed below the photo-electrode, in the frame separating the two compartments of the cell.

During irradiation, the evolved gases were collected within two upside-down graduated burettes surmounting each cell compartment. The amounts of H_2 and O_2 were determined from the displacement of the solutions within

each burette. The composition of the evolved gases was determined by gas chromatographic analysis, after withdrawal of gas samples at constant time interval with a gas-tight syringe. The irradiation source, always switched on 15 min prior to the beginning of the runs, was a UV–Vis iron halogenide mercury arc lamp (Jelosil HG200, 250 W) with a full irradiation intensity of 3.12×10^{-8} Einstein s^{-1} cm^{-2} on the photocatalytic cell, as determined by ferrioxalate actinometry.
H_2SO_4 (95–97 %) and NaOH (≥ 98.0 %) were purchased from Fluka. Ultra-pure water (18.2 MΩ cm at 25 ˚C), supplied by a Millipore Direct-Q 3 water purification system, was used to prepare all solutions.

3.4.5 Photocatalytic H_2 Production from Water-Ethanol Solutions

Experiments of photocatalytic H_2 production from water-ethanol solutions were carried out to assess the photocatalytic activity of Au-decorated TiO_2 NT arrays (synthesis, physico-chemical properties and photocatalytic performance are described in Section 3.2.3 and Chapter 9) and Au NPs-filled TiO_2 nanocavities (synthesis, physico-chemical properties and photocatalytic performance are described in Section 3.2.4 and Chapter 10).
For the photocatalytic H_2 production, the anodic layers were placed in a quartz tube containing water-ethanol solutions that were purged with N_2 for 30 min in order to remove O_2. Immediately after purging, the quartz tube was sealed with a rubber cap. The anodic films were irradiated with UV light provided by 200 mW HeCd laser (irradiation intensity 60 mW cm^{-2}, λ = 325 nm, Kimmon, Japan) while he ethanol-water solutions were constantly stirred. The laser beam was expanded to attain a spot of light of 1 cm^2. In order to measure the production of H_2, gas samples (typically of 200 μL) were withdrawn from the headspace within the quartz tube and analyzed by gas chromatography (GCMS – QP 2010 SE, Shimadzu).

3.5 Photo-Electrochemical Tests

3.5.1 IPCE & Photocurrent Transients

Incident photon to current conversion efficiency (IPCE) spectra and photocurrent transients were recorded to assess the photo-electrochemical properties of TiO_2 NT arrays, the synthesis and physico-chemical properties of which, along with their photocatalytic performance, are described and discussed in Section 3.2.1 and Chapter 7, respectively.

Photocurrent measurements were performed in a two-electrodes photo-electrochemical cell equipped with a Pyrex glass window, through which the TiO_2 NT arrays were illuminated. The cell was filled with 1.0 M NaOH aqueous solution. The anodic oxides and a platinum foil were used as working and counter electrodes, respectively. The illumination was provided by a 150 W Xe lamp (Lot-Oriel Arc Lamp) coupled to a monochromator (Lot-Oriel Omni-λ 300). The lamp irradiance was measured with a Newport calibrated photodetector (818-UV).
Incident photon to current conversion efficiency (IPCE) spectra were collected under monochromatic irradiation in the absence of any applied electric bias, by measuring the photocurrent density with a digital multimeter (Agilent 34410A) in the 340–460 nm range. The multimeter and the monochromator were simultaneously operated by custom-built LabView software, in order to acquire the steady short circuit photocurrent at each wavelength before moving to the next one.
Photocurrent transients were acquired by chrono-amperometric measurements (current density *vs.* time) under chopped irradiation (60 s light – 60 s dark cycles) using a Gamry Ref600 potentiostat. All NT arrays were monochromatically irradiated at the wavelength for which their maximum IPCE was measured. The irradiation power was always *ca.* 32 μW cm^{-2}.

3.5.2 Photo-Electrochemical Water Splitting

Photo-electrochemical water splitting experiments were carried out to assess the photo-electrochemical properties of pure and Ta-doped TiO_2 NT arrays, the synthesis and physico-chemical properties of which, along with their water splitting ability, are described and discussed in Section 3.2.2 and Chapter 8, respectively.
The photoelectrochemical water-splitting behavior of the anodic oxides was investigated in aqueous KOH solution (1 M) with a three-electrodes configuration, comprising a TiO_2 (or Ta-doped TiO_2) nanotubes layer photo-anode used as the working electrode, a saturated Ag/AgCl electrode as the reference and a platinum foil as the counter electrode. An external bias, provided by a scanning potentiostat (Jaissle IMP 88 PC) with a scan rate of 1 mV s^{-1}, was applied to the photo-electrochemical cell to record the photocurrent response. The photocurrent density was calculated by dividing the photocurrent response (in mA) by the anodic oxide area irradiated by the light source (0.196 cm^2). All experiments were carried out under simulated AM 1.5 illumination provided by a solar simulator (300 W Xe lamp with a Solarlight optical filter) with an irradiation power of 100 mW cm^{-2}. The light intensity was measured prior to all experiments using a calibrated

Si photodiode. H_2 and O_2 production runs were carried out in the three-compartment cell described in ref. [19]. The amount of H_2 and O_2 produced during the experiments were determined with a Shimadzu GCMS-QP 2010 SE, equipped with a TCD, Restek micropacked Shin Carbon ST columns (2 m × 0.53 mm) and a Zebron capillary column ZB-5 MS (30 m × 0.25 mm). Typical sample volumes of 200 µL were withdrawn from the glass tube (through a rubber septum) with a gas-tight SGE syringe. GC conditions: isothermal column temperature 45 ˚C; injector temperature 280 ˚C; TCD temperature 260 ˚C; flow rate of 14.3 mL min^{-1} with He as carrier gas.

3.6 References & Notes

[1] M.V. Dozzi, S. Livraghi, E. Giamello, E. Selli, Photochem. Photobiol. Sci. 10 (2011) 343.

[2] M.V. Dozzi, B. Ohtani, E. Selli, Phys. Chem. Chem. Phys. 13 (2011) 18217.

[3] M.V. Dozzi, L. Prati, P. Canton, E. Selli, Phys. Chem. Chem. Phys. 11 (2009) 7171.

[4] M.V. Dozzi, A. Saccomanni, E. Selli, J. Hazard. Mater. 211-212 (2012) 188.

[5] Although we speculatively state that those particles are Au^0 and Pt^0 nanocrystals, their chemical state has been investigated and verified only recently. G.L. Chiarello *et al*. (paper in preparation) performed an X-ray absorption spectroscopy study on a series of Pt/TiO_2 powders synthesized by flame-spray pyrolysis. As a main finding, it was observed for the as-formed samples that Pt is present as a mixture of and Pt^0 and Pt(II) states. Nevertheless, it was also demonstrated that Pt(II) oxide undergoes reduction to Pt^0 under UV-Vis light irradiation, in a flow of N_2 saturated with CH_3OH-H_2O vapors.

[6] G.L. Chiarello, M.H. Aguirre, E. Selli, J. Catal. 273 (2010) 182.

[7] G.L. Chiarello, A. Di Paola, L. Palmisano, E. Selli, Photochem. Photobiol. Sci. 10 (2011) 355.

[8] A.Q. Wang, C.M. Chang, C.Y. Mou, J. Phys. Chem. B 109 (2005) 18860.

[9] S. Rani, S.C. Roy, M. Paulose, O.K. Varghese, G.K. Mor, S. Kim, S. Yoriya, T.J. La Tempa, C.A. Grimes, Phys. Chem. Chem. Phys. 12 (2010) 2780.

[10] E. Selli, G.L. Chiarello, E. Quartarone, P. Mustarelli, I. Rossetti, L. Forni, Chem. Commun. (2007) 5022.

[11] R.B. Larson, ACVD, General Structural Analysis System, Los Alamos National Laboratory, 2004, 86.

[12] J.K. Burdett, T. Hughbanks, G.J. Miller, J.W. Richardson Jr., J.V. Smith, J. Am. Chem. Soc. 109 (1987) 3639.
[13] R.R. Pawar, V.T. Deshpande, Acta Crystallogr. A24 (1968) 316.
[14] A. Adamski, T. Spalek, Z. Sojka, Res. Chem. Intermediat. 29 (2003) 793.
[15] G.L. Chiarello, L. Forni, E. Selli, Catal. Today 144 (2009) 69.
[16] G.L. Chiarello, D. Ferri, E. Selli, J. Catal. 280 (2011) 168.
[17] M. Altomare, G.L. Chiarello, A. Costa, M. Guarino, E. Selli, Chem. Eng. J. 191 (2012) 394.
[18] M. Altomare, E. Selli, Catal. Today 209 (2013) 127.
[19] P. Roy, C. Das, K. Lee, R. Hahn, T. Ruff, M. Moll, P. Schmuki, J. Am. Chem. Soc. 133 (2011) 5629.

4. NH_4F-Modified TiO_2 Powders

4.1 Overview

A series of titania powders were synthesized by the sol-gel method. For some samples, specific amounts of NH_4F were added *in situ*, *i.e.*, during the hydrolysis of the Ti precursor. Hence, effects induced by NH_4F on the physico-chemical properties of the photocatalysts and on their photocatalytic activity were studied. The noble metal nanoparticles deposition on TiO_2 powders was also investigated, although this will be better discussed in Chapter 5. After the conversion into crystalline materials by thermal treatment and after the photodeposition of noble metal nanoparticles, these powders were tested for both a thermodynamically down-hill reaction, *i.e.*, the degradation of formic acid in aqueous suspension, and an up-hill reaction, *i.e.*, H_2 production from methanol–water vapors. The results presented in this chapter have been published in ref. [1].

4.2 Aim

The undesired recombination of charge carriers, *i.e.*, e^-–h^+ recombination, which is in competition with charge transfer toward the oxide surface, represents one of the main issues to solve in order to achieve a better performance of titanium dioxide-based photocatalysts.
In this context, heterojunctions formation, *e.g.*, by coupling different metal oxides (MOs) in intimate contact, and surface modification, *e.g.*, by depositing noble metal (NM) nanoparticles (NPs) on TiO_2 [2,3] have been quite often investigated to solve this problem.
Here, the effect of NM (*i.e.*, Pt and Au) NPs photodeposition on a series of NH_4F-modified TiO_2 photocatalysts is discussed in terms of their photocatalytic activity in the oxidative degradation of formic acid (FA) in aqueous suspension and in hydrogen production from methanol–water vapors. The main aim of the work was getting a better insight into *i)* the role played by NM NPs on both photocatalytic reduction and oxidation processes and *ii)* the effects of NH_4F on the physico-chemical properties of titania powders. In principle, the addition of NH_4F was supposed to induce N- and/or F-doping within the TiO_2 lattice. However, a previous work of our lab

[4], showed that no fluoride could be detected in the bulk of the materials and only surface fluorination of titania was attained, whereas N was found to occupy substitutional and interstitial positions within the TiO_2 lattice, although measurements of the optical band gap did not show any effect on the light absorption threshold for samples annealed at 700 ˚C. In other words, by adopting this method, photocatalysts active under Vis light were not obtained, although intriguing positive effects related to the addition of NH_4F were observed, as thoroughly discussed along this Chapter.
Formic acid has been investigated as a model substrate for photocatalytic oxidation reaction because *i)* it undergoes conversion into CO_2 and H_2O, without forming any stable intermediate which could possibly adsorb at the photocatalyst surface (interpretation of kinetic results is therefore simplified) and because *ii)* it does not absorb Vis light (studies of activity under visible light may be easily interpreted). Furthermore, the (room temperature and atmospheric pressure) production of H_2 through photocatalytic steam reforming of organics has recently gained huge attention [5-8]. In fact, it provides a way to convert solar into chemical energy under relatively mild conditions and with a reduced CO_2 impact if compared to the use of fossil fuels. In such a process, organic compounds improve the rate of H_2 evolution, with respect to pure water photosplitting, by acting as hole-scavengers, *i.e.*, by being quickly oxidized by *VB* holes and $^{\bullet}OH$ radicals (direct and indirect mechanism, respectively [8]), thus limiting e^--h^+ recombination [9-12].

4.3 Photocatalysts Characterization

All the details concerning the experimental and analytical procedures employed in this work have been fully discussed in Section 3.1.1.
The main structural features of the bare TiO_2 powders, *i.e.*, free of NM NPs, are summarized in Table 1. As-prepared powders were amorphous and crystallization was attained upon thermal treatment. The phase composition data for NH_4F-modified samples (obtained by Rietveld refinement of the XRD patterns shown in Fig. 1) evidence that the addition of NH_4F inhibits the anatase-into-rutile phase transition, which otherwise would occur when annealing unmodified titania at temperature as high as 700 °C. Nevertheless, the specific surface area (SSA) values for NH_4F-modified materials are slightly larger than that of the corresponding unmodified TiO_2 (but lower than that of P25). The XRD patterns obtained for samples modified by NM NPs deposition were practically similar to those recorded for the

corresponding bare samples. Also the SSA values did not vary upon NM NPs photo-deposition, in agreement with previous studies [13].

Sample	NH_4F/Ti molar ratio (%)	Anatase (wt%)	Rutile (wt%)	d_A (nm)	SSA ($m^2\ g^{-1}$)
P25	–	80	20	25	48
S0	–	38	62	65	7
S5	5	99	1	49	16
S7	7	100	–	44	14
S12	12	100	–	48	12

Table 1 – Phase composition and anatase crystallite dimensions d_A obtained from XRD analysis. Specific surface area (SSA) obtained from BET analysis.

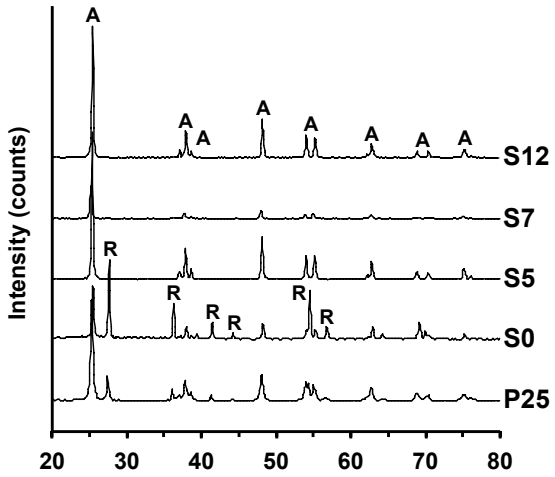

Figure 1 – XRD patterns for TiO_2 P25 and homemade TiO_2 powders prepared with different amounts of NH_4F. Homemade samples underwent thermal treatment at 700 °C, in air for 4 h.

The deposition of Au NPs on TiO_2 was confirmed by the change in color of the powders, turning from white into purple (purple color is due to the surface plasmon resonance of nanocrystalline Au^0 particles). As shown in Fig. 2(A), all Au-modified samples show an absorption band typical of the plasmonic resonance, with a maximum around 550 nm, *i.e.*, red shifted compared to the pure gold plasmon peak (520 nm [14]). This shift indicates an interaction between gold and titanium dioxide. Sample Au/S0 exhibits a red-shifted absorption edge because of its relatively high rutile content (see also Table 1).

Au-containing samples prepared with an intermediate NH_4F amount (S5 and S7) exhibit plasmon resonance bands that *i)* are slightly shifted toward

shorter wavelengths with respect to the other samples, indicating smaller sizes for the Au NPs [15] and *ii)* show relatively high maximum absorption intensities.

All Pt/TiO_2 samples, appearing as grey powders, show broad and featureless absorption spectra over the visible region (see Fig. 1(B)).

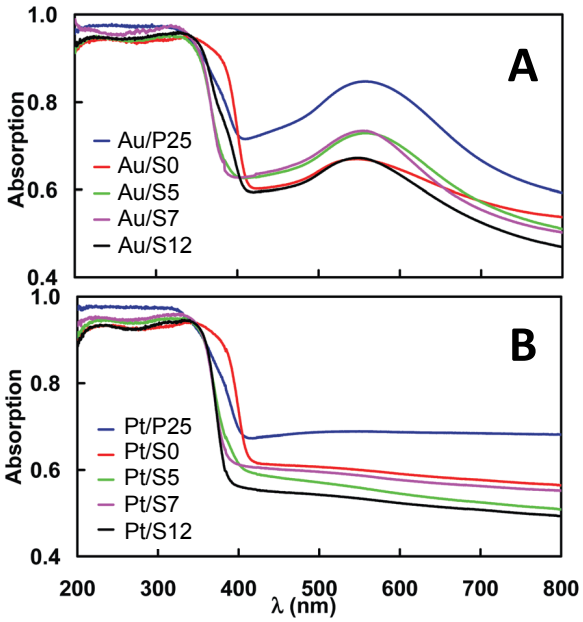

Figure 2 – UV-Vis absorption spectra for P25 and for homemade TiO_2 powders, all modified by (A) Au and (B) Pt NPs deposition (0.5 wt%).

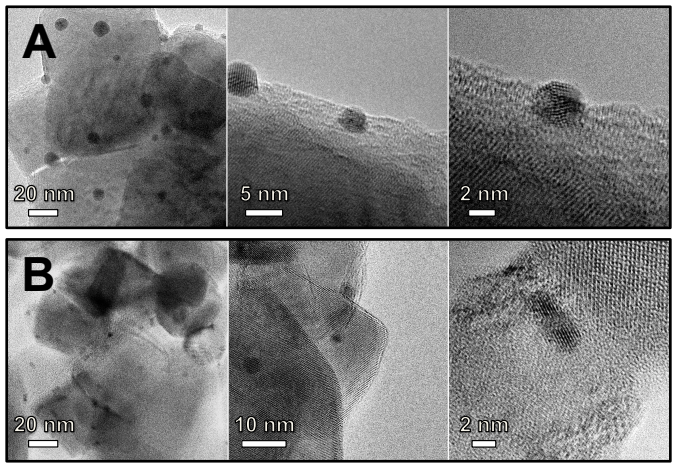

Figure 3 – HRTEM images (different magnifications) of TiO_2 powders prepared with addition of NH_4F and modified by Au (A) or Pt (B) NPs photo-deposition (NH_4F/Ti % molar ratio = 7; the powders underwent annealing at 700 °C before NM NPs deposition).

Au and Pt deposition was corroborated by HRTEM, yielding direct information on the size and distribution of the NM NPs at the TiO_2 surface (see Fig. 3). Homemade samples appear as micro aggregates of single crystal nanospheres (however, the existence of a single and coherent crystallographic domain has not been effectively verified). The average diameter of the crystallites ranged from 40 to 50 nm, which is consistent with the values calculated from XRD data (Table 1). Overall, the adopted photodeposition technique seems to ensure a good dispersion of the NM NPs at the TiO_2 surface (see Fig. 3(A) and (B)). On the other hand, Pt NPs resulted slightly smaller than Au ones.
XPS analysis, performed in a previous work of our research group on samples prepared under the same experimental conditions, revealed the actual presence of both N and F, mainly in the substitutional and surface forms, respectively. The concentration of N and F was also shown to increase with increasing the nominal amount of NH_4F used during the synthesis [4].

4.4 Formic Acid Photocatalytic Oxidation

Since this reaction, *i.e.*, FA oxidation, always occurred at constant rate, the photocatalytic activity of the samples discussed herein is evaluated in terms of the zero-order rate constants, k^0, as reported in Fig. 4. TiO_2 powders prepared with moderate amounts of NH_4F (*i.e.*, samples S5 and S7) were more active than pure TiO_2 powders (S0).
As expected, the presence of Au and Pt NPs deposited on the powders led to a beneficial increase of FA degradation rate. The effects induced by the photodeposition procedure itself can be distinguished from that induced by the presence of NM NPs by taking into account the photocatalytic performance of the reference samples (R/TiO_2, Fig. 3). As described in Section 3.1.1, reference samples (R/TiO_2) were obtained by irradiating the bare materials under nitrogen atmosphere in the presence of methanol and in the absence of NM precursors.
The lower photoactivity of R/TiO_2 samples (compared to that of the corresponding unmodified powders) demonstrates that the photodeposition procedure as such negatively affects the surface properties of titania, thus slowing down FA photo-oxidation. This might be ascribed to the presence of residual methanol molecules on the photocatalyst surface, which possibly compete with FA for reaction with *VB* holes. Consistently, previous works reported that any modification of P25 TiO_2 induced by treatments for NM NPs deposition implies a decrease of photocatalytic activity, particularly in

the case of deposition–precipitation methods which require a thermal treatment for metal reduction [16].

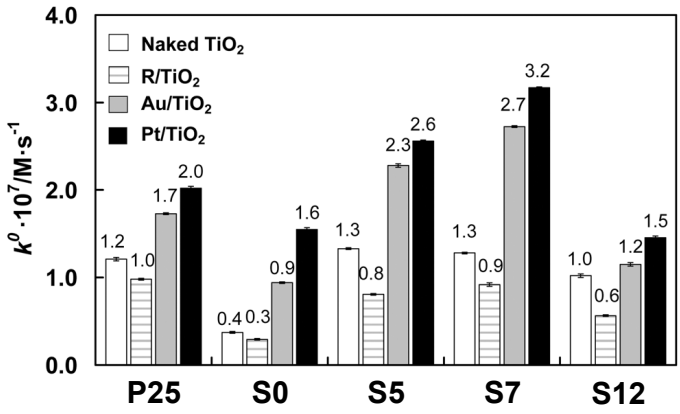

Figure 4 – Zero-order rate constants of formic acid photo-mineralization for photocatalysts prepared with different amounts of NH_4F. The samples were also modified by Au or Pt NPs deposition. R/TiO_2 refers to samples that underwent the same photodeposition procedure but in the absence of any noble metal precursor.

The rate constant values reported in Fig. 4 clearly confirm that Pt is a better co-catalyst than Au. The difference in the photocatalytic performance can be related to their work function values (φ), *i.e.*, the energy required to promote an electron from the Fermi energy level into *vacuum* (the higher φ, the lower the energy of the Fermi level). In fact, the greater the difference between the metal work function and that of TiO_2, the higher the Schottky barrier generated by the band alignment at the metal–semiconductor interface [2]. As a direct consequence, the efficiency of the electron trapping by the NM and the subsequent transfer to O_2 molecules adsorbed on the photocatalyst is increased. For the 111 crystal plane, φ = 5.31 and 5.93 eV are reported for Au and Pt, respectively [17], whereas, values in the 4.6–4.7 eV range are reported for TiO_2 [18]. Consequently, Pt is more efficient than Au in trapping the *CB* electrons, thus ensuring a more effective charge separation, in line with the higher photoactivity of Pt-modified TiO_2. Nevertheless, the higher photoactivity of Pt-loaded powders possibly owes to smaller dimensions of the Pt NPs (as observed by HRTEM analysis), that is, smaller Pt crystals may allow a better contact with the semiconductor surface, thus enhancing the electron trapping and reducing the charge recombination process.

Most importantly, it was also observed that the best performing homemade materials (Au and Pt/S7) were even more active than P25 TiO_2, modified according to the same procedure of NM NPs deposition (see Fig. 4).

On the other hand, when large amounts of NH_4F were added during the synthesis (as in the case of sample S12), a decrease of the photocatalytic activity was observed. This is possibly due to an excess of structural defects in the TiO_2 lattice that could act as recombination centers of the charge carriers.

4.5 H_2 Production by Methanol Photo-Steam Reforming

For all photocatalytic tests, production of H_2, CO_2 and CO occurred at constant rate during irradiation. The zero-order rate constants of H_2 production measured for the investigated photocatalysts are reported in Fig. 5 (for the sake of brevity, selectivity to CO and CO_2 will not be discussed herein). Among the naked samples (inset in Fig. 5), full-anatase S5 was the most active photocatalyst. Here, in contrast with the results obtained for FA photo-oxidation, sample S0 (composed of A/R mixed phase) showed photoactivity quite similar to those of S7 and S12 (full anatase powders), although the two NH_4F-TiO_2 samples showed larger SSA values (Table 1).

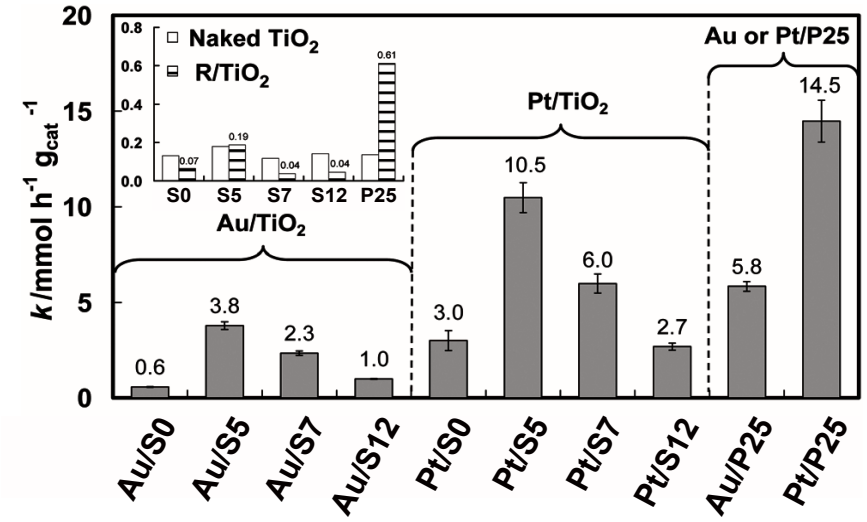

Figure 5 – Zero-order rate constants of H_2 production on naked NH_4F-TiO_2 and reference R/TiO_2 powders (both in the inset), and on 0.5 wt% Au- and Pt-modified TiO_2. Results for commercial P25 are also reported for comparison.

Considering that the anatase (A) phase is characterized by a more negative E_{CB} than the rutile phase (R) (*i.e.*, – 0.45 and – 0.37 V *vs.* SHE at pH 7 [19]), conduction band electrons in the anatase phase are expected to be more effective in reducing protons, yielding H_2. On the other hand, the absorption threshold for A is at shorter wavelengths compared to that of R. Therefore, A

most likely absorbs a slightly smaller fraction of the spectrum. As a result of these two counterbalancing effects, mixed phase S0 and P25 exhibit a photocatalytic activity similar to those measured for full anatase S7 and S12.
As mentioned when discussing the results of FA photo-oxidation, the effect of the photodeposition procedure on photoactivity can be assessed by comparing the rate constants measured for reference R/TiO_2 samples with those for unmodified naked samples (inset of Fig. 5). As already observed in FA photo-oxidation, the photodeposition procedure itself negatively affected the surface properties of homemade titania. However, this did not occur for sample S5, its photoactivity remaining almost unchanged after the treatment.
On the contrary, the activity of P25 was strongly enhanced by the photodeposition procedure. In fact, the rate constant measured for R/P25 was about four times greater than for as-received (untreated) powders. These results are in agreement with recent reports on R/P25 used for photocatalytic reduction of Cr(VI) ions [20]. Such an effect could be related to a partial surface reduction of TiO_2 P25 when UV-light irradiated, under anaerobic conditions and in the absence of the NM NPs precursor.
As expected, Au and Pt deposition on titania induced a more than ten-fold increase of the H_2 production rate compared to the reference bare oxides (see Fig. 5). Here, the increase of photoactivity observed after NM NPs deposition was more marked than that measured for FA degradation (Fig. 4). However, for both photocatalytic reactions, Pt/TiO_2 powders resulted more active than Au/TiO_2 ones, as a consequence of the higher work function value of Pt, as discussed in Section 4.4.
Au and Pt NPs at the semiconductor surface are able to collect conduction band electrons, thus increasing the efficiency of charge separation and, consequently, favoring electron transfer to the protons. For this reaction, CH_3OH photo-oxidation occurs at the semiconductor surface, the latter acting as a photo-anode, whereas H_2 evolution takes place at noble metal sites, acting as photo-cathode.
Yet, bell-shaped trends were obtained for the naked, Au and Pt/titania series when plotting the measured photoactivity *vs.* the amount of NH_4F used during the synthesis. By observing such trends, one can notice that sample S5 is always the best photocatalyst within each series. These results can be explained by supposing that moderate amounts of NH_4F added during the synthesis (*i.e.*, NH_4F/Ti molar ratio of *ca.* 5 %) lead to the formation of nanosized powders with relatively high SSA, composed of almost full-anatase phase exhibiting high crystallinity. These features most likely guarantee an effective charge-carrier separation and also adsorption of reactive species at a large extent.

Furthermore, the data shown in the inset of Fig. 5 prove that the only addition of NH_4F, regardless of the amount, produces negligible effects on the rate of H_2 evolution. On the other hand, the use of NH_4F appears to be essential in order to ensure a relevant H_2 evolution rate with the corresponding Au and Pt-modified materials, especially when prepared with moderate amounts of NH_4F (NH_4F/Ti molar ratio of 5 and 7 %). This effect can be addressed as a synergistic phenomenon occurring when homemade oxides are both modified by the addition of NH_4F and photodeposition of NM NPs. In particular, the extent of surface fluorination can largely affect the result of the photodeposition procedure in terms of size and distribution of the noble metal nanoparticles.

4.6 Conclusion & Further Work

The addition of suitable amounts of NH_4F resulted beneficial in view of enhancing the photocatalytic activity of homemade TiO_2 powders. The oxides prepared with NH_4F consisted of pure anatase, although thermal annealing was performed at 700 °C. Moreover, for moderate amounts of NH_4F, the average dimension of the crystallites and the SSA values resulted lower and higher, respectively, than those observed when NH_4F was either avoided or over-added. In other words, a controlled addition of NH_4F can lead to nanosized titanium dioxide particles, composed of full-anatase phase, even if annealed at 700 °C, and exhibiting relatively high SSA, all these features being necessary in view of fabricating materials with high performance for heterogeneous photocatalysis.

Further studies are necessary to clarify the role of both N and F in stabilizing the anatase phase at high temperature. Moreover, hydrophilicity measurements would better clarify the role and the extent of surface fluorination. Nevertheless, the possible presence of N or F within the TiO_2 lattice, *i.e.*, doping, must be investigated more in depth.

Last but not least, yet concerning TiO_2 surface fluorination, NM NPs photodeposition as such is intrinsically affected by the physico-chemical properties of the photocatalyst, *i.e.*, the result of the photodeposition (in terms of size-distribution of metal nanoparticles and their distribution at the semiconductor surface) would never be the same for every oxide, but it rather depends on the features of the material itself (which are related to surface properties and photocatalytic activity). In fact, photodeposition actually consists of a reduction of a metal cation operated by conduction band electrons. Therefore, it is reasonable to suppose that, for instance,

photodeposition is faster when carried out on a powder exhibiting high photocatalytic activity. Hence, many parameters must be taken into account in order to properly compare different materials that have undergone NM nanoparticles photodeposition.

4.7 References & Notes

[1] M.V. Dozzi, A. Saccomanni, M. Altomare, E. Selli, Photochem. Photobiol. Sci. 12 (2013) 595.
[2] P. Kamat, J. Phys. Chem. B 106 (2002) 7729.
[3] A.L. Linsebigler, G. Lu, J.T. Yates, Chem. Rev. 95 (1995) 735.
[4] M.V. Dozzi, B. Ohtani, E. Selli, Phys. Chem. Chem. Phys. 13 (2011) 18217.
[5] G.L. Chiarello, L. Forni, E. Selli, Catal. Today 144 (2009) 69.
[6] G.L. Chiarello, M.H. Aguirre, E. Selli, J. Catal. 273 (2010) 182.
[7] G.L. Chiarello, A. Di Paola, L. Palmisano, E. Selli, Photochem. Photobiol. Sci. 10 (2011) 355.
[8] G.L. Chiarello, D. Ferri, E. Selli, J. Catal. 280 (2011) 168.
[9] G. Wu, T. Chen, W. Su, G. Zhou, X. Zong, Z. Lei, C. Li, Int. J. Hydrogen Energy 33 (2008) 1243.
[10] O. Rosseler, M.V. Shankar, M. Karkmaz-Le Du, L. Schmidlin, N. Keller, V. Keller, J. Catal. 269 (2010) 179.
[11] N. Strataki, V. Bekiari, D.I. Kondarides, P. Lianos, Appl. Catal. B Environ. 77 (2007) 184.
[12] J. Greaves, L. Al-Mazroai, A. Nuhu, P. Davies, M. Bowker, Gold Bull. 39 (2006) 216.
[13] M. Mrowetz, A. Villa, L. Prati, E. Selli, Gold Bull. 40 (2007) 154.
[14] M.C. Daniel, D. Astruc, Chem. Rev. 104 (2004) 293.
[15] S. Link, M. El-Sayed, J. Phys. Chem. B 103 (1999) 8410.
[16] M.V. Dozzi, L. Prati, P. Canton, E. Selli, Phys. Chem. Chem. Phys. 11 (2009) 7171.
[17] CRC Handbook of Chemistry and Physics, Taylor & Francis, 87th edn., 2006, pp. 12–114.
[18] C. Young, T. M. Lim, K. Chiang, J. Scott, R. Amal, Appl. Catal. B Environ. 78 (2008) 1.
[19] A. Di Paola, M. Bellardita, R. Ceccato, L. Palmisano, F. Parrino, J. Phys. Chem. C 113 (2009) 15166.
[20] M.V. Dozzi, A. Saccomanni, E. Selli, J. Hazard. Mater. 211–212 (2012) 188.

5. Au & Pt/TiO_2 Anatase Powders

5.1 Overview

Metal-loaded TiO_2 is, by far, one of the most important photocatalyst for H_2 production. Anatase powders loaded with Au or Pt nanoparticles were prepared by an impregnation-reduction method and studied for H_2 production through photo-steam reforming of methanol-water vapors. The electron and hole trapping centers, Ti^{3+} and O^-, respectively, formed upon UV–Vis activation of the semiconductor, were studied by *in situ* electron spin resonance spectroscopy. It was observed that the nature of the loaded metal affected both the H_2 evolution rate and the distribution of the methanol oxidation products. Data and results presented in this chapter have been published in ref. [1].

5.2 Aim

Although a large number of materials potentially suitable for photo-assisted H_2 production have been explored [2-7], titanium dioxide still represents the benchmark photocatalyst owing to its large availability, cheapness, stability, and non-toxicity. In spite of this, the electron-hole recombination process, common to all semiconductors, lowers its photocatalytic efficiency. Indeed, the charge-carriers separation and transfer are key issues, which can be improved by *i)* co-catalyst loading (*e.g.*, noble metal, transition-metal oxide, non-metal oxide), *ii)* by coupling of different semiconductors, or *iii)* by modifying the crystal structure and morphology of the material [8].
Furthermore, the rate of H_2 production can be boosted in the presence of sacrificial organics (*e.g.*, methanol [9-13], ethanol and glycerol [14]), these organics being able to combine with holes more rapidly than water itself.
Concerning metal loaded oxides, when the metal nanoparticles (NPs) are deposited onto the surface of TiO_2, conduction band electrons preferentially migrate toward the metal co-catalyst [15,16], as also discussed in the previous chapter. As overall result, the collection of electrons by the metal NPs decreases electron-hole recombination.
Up to now, several metals have been used as titania co-catalyst [17-20] though the best performance for the photocatalytic production of H_2 have

been obtained with Pt or Au/TiO_2. The main reason for this behavior relies on the separation of charge carriers generally attributed to the formation of a Schottky barrier at the metal/TiO_2 interface. The higher is the Schottky barrier, the lower is the recombination rate for electron-hole pairs and the greater is H_2 production [9,11-13,21].
In early work, Bamwenda *et al.* [22] reported that the H_2 yield from water-ethanol solution was greatly improved by Pt deposition on titania, rather than by Au deposition. The higher activity was ascribed to a more effective trapping and pooling of *CB* electrons by Pt deposits and/or to the higher intrinsic Pt activity in reduction processes.
Although the beneficial effect of noble metal loading on the photocatalytic properties of TiO_2 in reduction processes is well established, their role in the parallel oxidation reactions is still under debate. Furthermore, there hardly is any investigation that directly relates morphological and electronic properties of metal co-catalysts to the type, amount and location of the electronic defects and charge carriers active in the photocatalytic process.
Aiming at covering such a piece of knowledge, an *in situ* electron spin resonance (ESR) spectroscopy study on Au and Pt/TiO_2 photocatalysts tested for H_2 production through methanol photoreforming is reported in this chapter. The direct investigation, performed by ESR analysis, of the paramagnetic species formed upon TiO_2 irradiation has recently provided relevant insight into the mechanism of specific photocatalytic processes and also suggested ways for improving the photo-efficiency through the manipulation of defect states [23-25].

5.3 Photocatalysts Characterization

As described in Section 3.1.2, TiO_2 anatase powders (TiO_2-A) were prepared by annealing commercial amorphous titania at 500 ˚C in air. Then, Au- and Pt-loaded powders were obtained by an adsorption-reduction method. The XRD pattern of TiO_2-A, reported in Fig. 1, shows that the sample was crystalline and composed of 100 % anatase phase, with an average crystallites size of 15 nm, evaluated using the Scherrer equation based on the [101] anatase reflection. Almost identical XRD patterns were recorded for TiO_2-Rf and for the two metal-loaded samples (not shown here), indicating that metal deposition followed by reduction with $NaBH_4$ did not affect the phase and the crystallite size of the materials, as expected from previous reports [26].

Nitrogen physisorption experiments were performed on metal-loaded catalysts and on TiO_2-Rf. All samples resulted mesoporous, showing a type IV Brunauer isotherm. As an example, the adsorption–desorption isotherms and the corresponding monomodal pore-size distribution of Pt/TiO_2 NPs are shown in Fig. 2(A).

The specific surface areas (SSA) and Barrett-Joyner-Halenda (BJH) pore volumes (desorption cumulative pore volume - DCPV) of the different samples are reported in Table 1. It is worth noting that the SSA for TiO_2-Rf is significantly higher than those for metal-loaded TiO_2. A similar trend is also observed for DCPV values, with Au and Pt/TiO_2 respectively showing a 40 and 35 % reduction of pore volume in comparison to TiO_2-Rf. The reduction of both surface area and pore volume after metal loading might be a consequence of the Au and Pt deposits, plugging the pores of the catalyst.

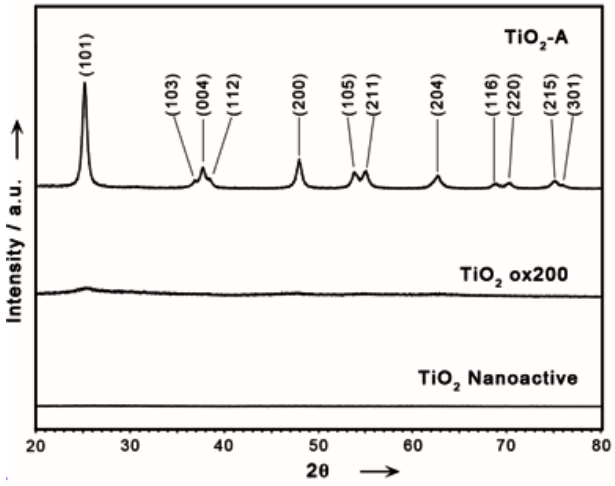

Figure 1 – XRD patterns of as-received TiO_2 powder (NanoActive®) and materials annealed under different conditions (TiO_2 ox200 and TiO_2-A). TiO_2-A resulted composed of 100 % anatase.

Sample	SSA_{BET} ($m^2\ g^{-1}$)	BJH pore volume ($cm^3\ g^{-1}$)
TiO_2-Rf	147.9 ± 0.05	0.224
Au/TiO_2-A	94.32 ± 0.05	0.135
Pt/TiO_2-A	98.11 ± 0.05	0.145

Table 1 – Specific surface area SSA_{BET} and total pore volume (DCPV) of bare and metal-loaded titania powders.

The UV–Vis absorption spectra of bare and metal-loaded TiO_2 samples are shown in Fig. 2(B). Diffuse reflectance data were converted into *F(R)* values according to the Kubelka–Munk equation. TiO_2-Rf showed an optical bandgap value of *ca.* 3.1 eV, comparable with those of TiO_2-A, Au/TiO_2-A and Pt/TiO_2-A. This indicates that neither the $NaBH_4$ treatment nor the metal deposition procedure induced substantial variation of the energy needed for band–band transition.

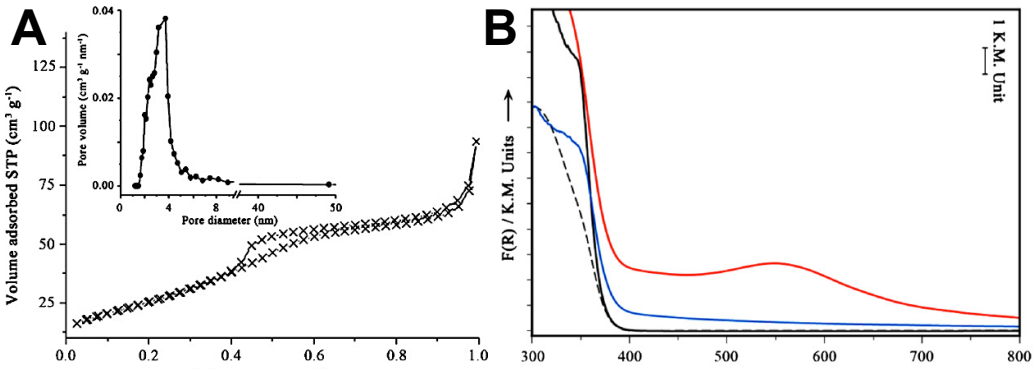

Figure 2 – (A) Adsorption–desorption isotherm at liquid nitrogen temperature of Pt/TiO_2. The curve corresponds to a type IV isotherm with capillary condensation in the mesopores. Inset: pore-size distribution. (B) DR UV–Vis spectra of TiO_2-A (black dashed line), TiO_2-Rf (black continuous line), Au/TiO_2-A (red line) and Pt/TiO_2-A (blue line).

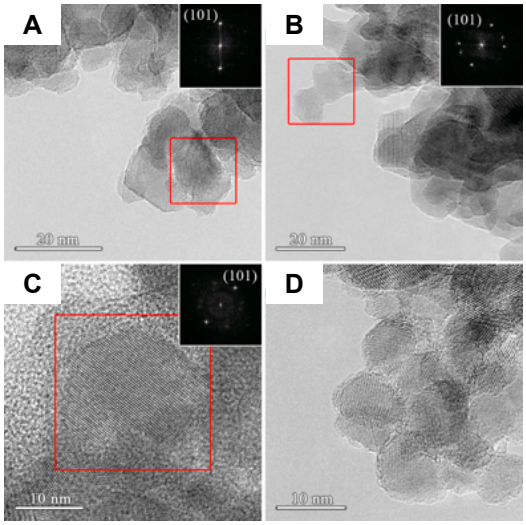

Figure 3 – HRTEM micrographs along with their selected area (red squares) electron diffraction (SAD) patterns (see insets) for (A and C) TiO_2-A and (B and D) TiO_2-Rf.

Au/TiO_2-A also shows the typical absorption band (λ_{max} = 549 nm) in the visible region attributable to the surface plasmon resonance (SPR) of gold NPs (as already discussed in Chapter 4). Differently, plasmon absorption of Pt NPs of Pt/TiO_2-A is not visible, being covered by the TiO_2 bandgap

absorption in the UV spectral region (the weak absorption of Pt/TiO_2-A in the visible region has been predicted by theoretical calculations [27]).
The HRTEM micrographs for TiO_2-A and TiO_2-Rf are shown in Fig. 3. Both samples consisted of aggregates of irregular-in-shape TiO_2 particles, about 10–25 nm in size (in agreement with the calculations based on XRD analysis), and were composed of well-formed TiO_2 single crystals preferentially exposing the [101] facets (see fast Fourier transform in the insets of Fig. 3). These results corroborate that the reduction treatment apparently did not induce any significant modification of the nanomaterial morphology.

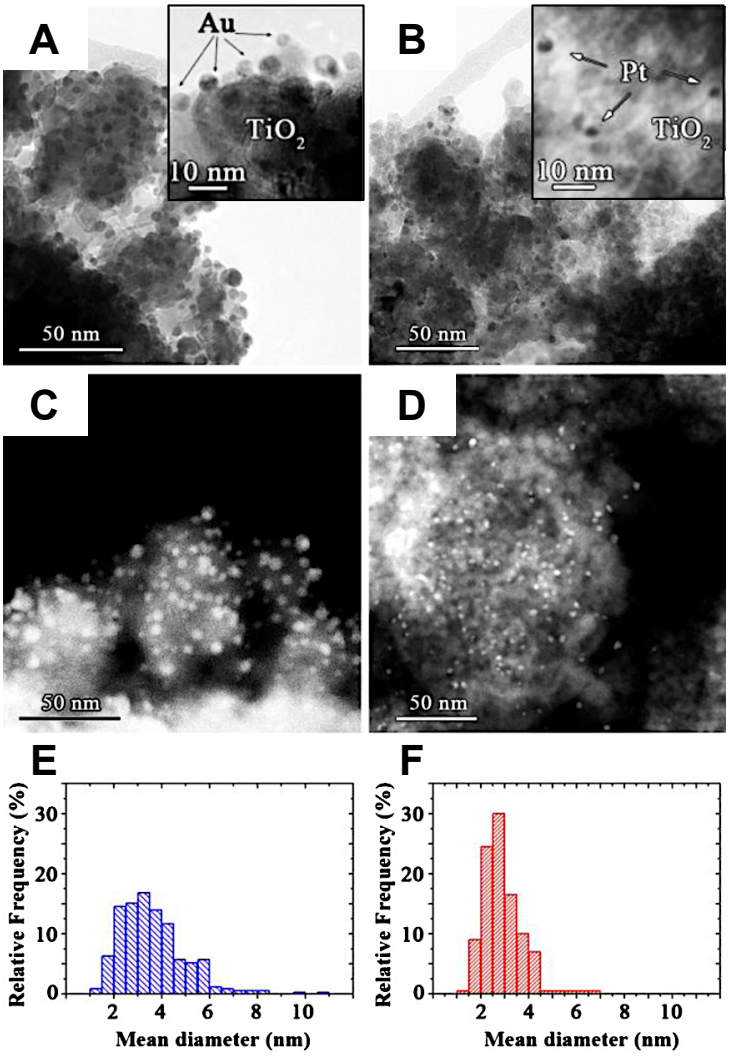

Figure 4 – HRTEM micrographs of (A) Au/TiO_2-A and (B) Pt/TiO_2-A (the insets are high magnification views of Au and Pt NPs deposited on TiO_2-A crystallites). HAADF-STEM images and metal NPs size distribution of (C and E) Au/TiO_2-A and (D and F) Pt/TiO_2-A.

The HRTEM and HAADF-STEM images for Au and Pt/TiO_2-A reported in Fig. 4 demonstrate that the metal NPs deposited on TiO_2-A *via* the impregnation/$NaBH_4$ reduction method (described in Section 3.1.2) were highly dispersed over the whole oxide surface. Both Au (Fig. 4(A) and (C)) and Pt (Fig. 4(B) and (D)) NPs were grown homogeneously and have nearly spherical shape. The insets in Fig. 4(A) and (B) show high magnification pictures of typical zones with several Au and Pt NPs on the TiO_2 surface. Based on the HAADF-STEM analysis, the size distribution of Au NPs resulted centered around 3.6 nm (Fig. 4(E)), whereas that of Pt NPs was picking at around 2.9 nm (Fig. 3(F)). The Pt NPs not only had a lower average diameter compared to Au ones, but also a narrower size distribution. This peculiarity was proved to be fundamental in influencing the activity of noble metal-loaded photocatalysts (see Section 5.4).

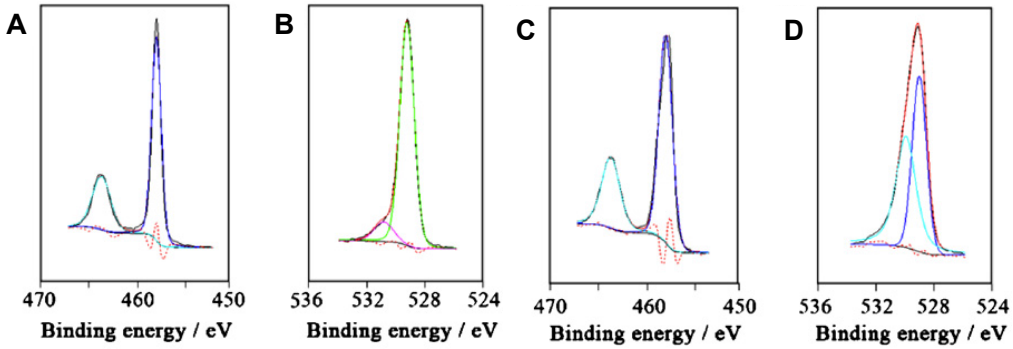

Figure 5 – XPS (A and C) Ti 2p and (B and D) O 1s regions of (A and B) Au/TiO_2-A and (C and D) Pt/TiO_2-A, respectively.

XPS analysis was performed on M/TiO_2-A samples in order to investigate their electronic properties. In particular, binding energy regions typical of Ti 2p, O 1s, Pt 4f and Au 4f were analyzed.

A common feature observed for both Au and Pt/TiO_2-A samples was the position of the main (j = 3/2) spin–orbit split component of the Ti 2p peak at 458.01 eV, which is typical of Ti(IV) sites coordinated to oxygen atoms (Fig. 5(A) and (C)) [28]. Regarding the O 1s peak, a significant broadening and the presence of a shoulder at the high BE side were observed for both samples, suggesting the coexistence of different chemical environments. After peak deconvolution (Fig. 5(B) and (D)), the XPS signal for O 1s appears as composed of a major component picking at 529.24 eV, typical of oxygen atoms in the anatase lattice, and a minor band at higher BE (*ca.* 530.85 eV) mainly related to the presence of ≡Ti-OH species and/or to some surface hydration [29]. In line with this attribution, the O/Ti atomic ratio, obtained from the XPS survey analysis, was *ca.* 2.9 for both samples, which is higher than the stoichiometric value (*i.e.*, 2) expected for the oxide.

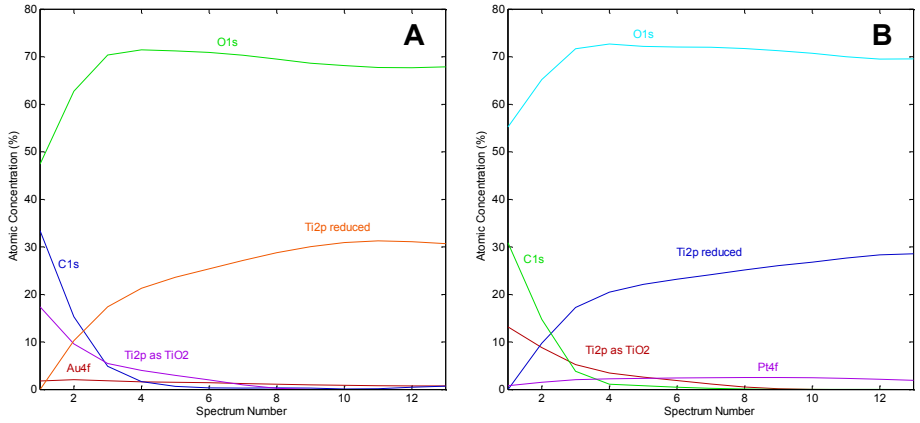

Figure 6 – Profiles of atomic concentration (XPS analysis) of (A) Au/TiO_2-A and (B) Pt/TiO_2-A as a function of the sputtering time.

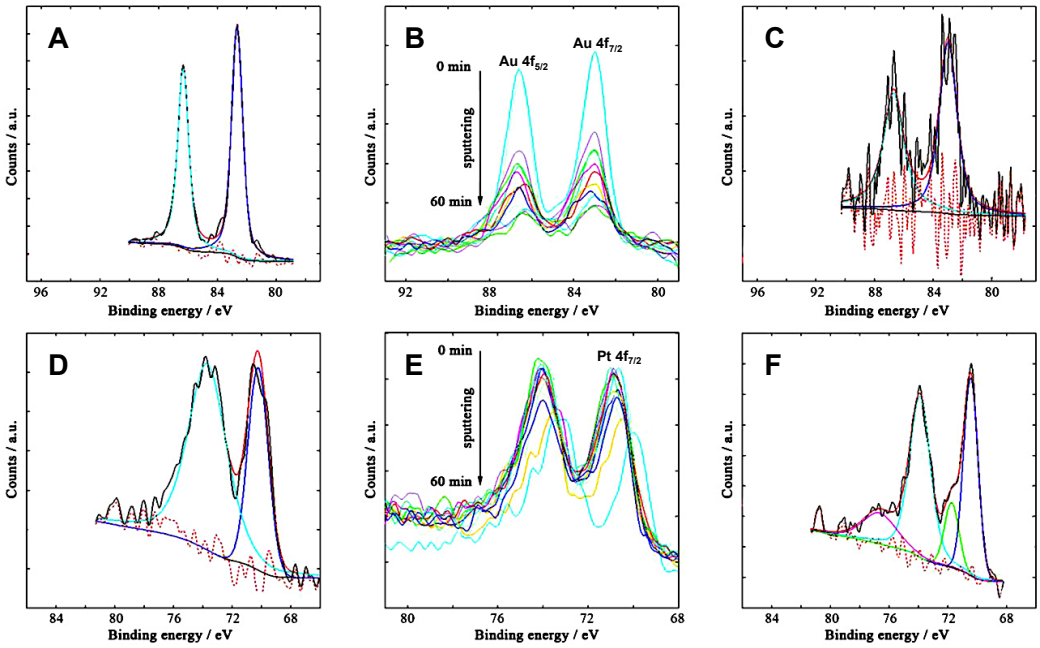

Figure 7 – XPS spectra of the Au 4f region of Au/TiO_2-A (A) before and (C) after 60 min-long Ar^+ sputtering; Pt 4f region of Pt/TiO_2-A (D) before and (F) after 60 min-long Ar^+ sputtering; time evolution of the XPS signal in the Au 4f region (B) and the Pt 4f region (E), recorded after successive steps of Ar^+ sputtering.

The depth-profile XPS analysis revealed a decrease in intensity of the O 1s signals, without any shift of the XPS band maximum during sputtering. In contrast, the Ti 2p signals decrease in intensity and shift to lower BE values, indicating the reduction of Ti(IV) to Ti(III) due to Ar^+ ion sputtering, as already reported in literature (Ti atomic concentration depth profiles are reported in Fig. 6) [30].

Fig. 7 shows the Au 4f and Pt 4f lines for Au and Pt/TiO_2-A, before and after 60 min-long Ar^+ sputtering. The variations in line shape during sputtering

are reported in Fig. 7(B) and (E). The shape and peak position of the Au 4f signal (BE Au $4f_{7/2}$ ≈ 82.72 eV, j–j doublet separation ≈ 3.6 eV; Fig. 7(A)) indicate that the metal was dispersed on the titanium oxide surface in metallic form (Au^0) only. No changes in the gold electronic state were observed after Ar^+ sputtering (Fig. 7(B) and (C)). The surface Au/Ti atomic ratio was *ca.* 0.014, in agreement with the nominal noble metal amount.
On the other hand, variations of the Pt 4f peak position were observed, depending on the duration of Ar^+ sputtering. Before sputtering, only Pt^0 species (BE Pt $4f_{7/2}$ ≈ 70.25 eV, j–j doublet separation of *ca.* 3.5 eV) was detected by XPS analysis (Fig. 7(D)). After Ar^+ sputtering, besides Pt^0, a different platinum species appeared (BE Pt $4f_{7/2}$ ≈ 71.72 eV, j–j doublet separation *ca.* 4.9 eV; Fig. 7(E) and (F)), attributable to the presence of Pt(II) (*i.e.*, oxidized platinum) located in the sub-surface region of the Pt NPs [31], with a relative Pt(II)/Pt(0) atomic ratio of *ca.* 0.2. The surface Pt/Ti atomic ratio was *ca.* 0.009 for the Pt/TiO_2-A sample.

5.4 H_2 Production by Methanol Photo-Steam Reforming

The rates of hydrogen production r_{H2} measured for the photocatalytic steam reforming of methanol are reported in Fig. 8(A), together with the rates of formation of the main methanol oxidation products, *i.e.*, carbon dioxide (CO_2), carbon monoxide (CO) and formaldehyde (H_2CO). Photoactivity greatly increased in the presence of noble metal NPs at the TiO_2 surface, with an increase of r_{H2} by more than one order of magnitude (see Table 2). However, the comparison between the activity obtained with sample TiO_2-Rf and those obtained with TiO_2-A evidences that also the reducing and cleaning treatment with the $NaBH_4$ solution contributed in increasing the performance of the bare TiO_2 surface (a similar phenomenon was observed when depositing Au or Pt NPs on P25 TiO_2 by photodeposition, as described in the previous chapter in Section 4.5). Thus, in order to discriminate the effect induced by noble metal NPs from that consequent to the deposition treatment, TiO_2-Rf should be considered as the reference when discussing the effects of noble metal NPs on the photocatalysts performance. Moreover, platinum was confirmed to be a better co-catalyst than gold, as already found in previous studies on the same photocatalytic reaction performed with a series of noble metal-modified TiO_2 photocatalysts, regardless of the preparation method (deposition of surfactant-stabilized noble metal NPs, single-step flame spray pyrolysis and photodeposition were all studied and demonstrated Pt to be a better co-catalyst than Au) [9,32,33].

The apparent quantum efficiency of H_2 production, Φ_{H2}, in the photocatalytic steam reforming of CH_3OH was calculated from the rate of hydrogen production and the measured irradiance on the reactor. Values of Φ_{H2} for Au and Pt/TiO_2-A measured under simulated sunlight were 10 and 14 %, respectively (see Table 2). Remarkably, Au/TiO_2-A showed a H_2 production rate of 15.8 mmol h^{-1} g^{-1}, that is *ca.* 20 % higher than that measured for 1 wt% Au/TiO_2 (Degussa-Evonik P25) with the same photocatalytic set-up [9]. By the same way, Pt/TiO_2-A powders prepared in this study present a 50 and 15 % increase of H_2 production rate compared to 0.5 wt% Pt/TiO_2 (prepared in a single-step by flame spray pyrolysis) and to 1 wt% Pt/TiO_2 (synthesized by the deposition of surfactant-stabilized preformed NM nanoparticles on commercial TiO_2 Degussa-Evonik P25), respectively. Nevertheless, Pt/TiO_2-A powders prepared in this study showed higher r_{H2} than that for 0.5 wt% Pt/TiO_2 P25 prepared by photodeposition (preparation and physico-chemical properties for the latter are discussed in Section 3.1.1 and Chapter 4).

Sample	r_{H2}	r_{H2CO}	r_{CO}	r_{CO2}	Φ_{H2}
TiO_2-A	0.65±0.09	0.10±0.06	0.06±0.01	0.03±0.04	0.4
TiO_2-Rf	1.0±0.3	0.3±0.2	0.08±0.01	0.05±0.03	0.4
Au/TiO_2-A	15.8±0.7	5.9±0.5	0.24±0.01	2.02±0.07	10
Pt/TiO_2-A	21.4±0.2	5.4±0.7	0.14±0.01	3.29±0.07	14

Table 2 – Photocatalytic performance in CH_3OH photo-steam reforming, expressed as rates of products formation, r_X (in mmol h^{-1} g^{-1}) with X = H_2, CO, CO_2 and H_2CO, and percent quantum efficiency of hydrogen production, Φ_{H2}.

The presence of oxidation products other than CO_2 in the reaction system confirms that methanol photoreforming proceeds through a rather complex mechanism which involves a series of consecutive intermediate oxidation steps, occurring on the photocatalyst surface, each of them yielding a H_2 molecule and differently oxidized carbon-containing molecules. Concerning these latter, part of them desorb from the photocatalyst surface, without undergoing further oxidation [9,34,35]. The effect induced by the presence of noble metal NPs on the distribution of methanol oxidation products can provide valuable information on the role of the co-catalyst in increasing the photocatalyst performance, particularly in the oxidation paths.

In fact, as shown in Fig. 8(B), the r_{H2}/r_{CO2} ratio was always much higher than the ideal (stoichiometric) value, *i.e.*, 3, expected on the basis of complete methanol oxidation, indicating that this reaction was always far from being

complete. However, the r_{H2}/r_{CO2} ratio dropped from *ca.* 20 to values *ca.* 6 (still higher than 3) in the presence of noble metal NPs on TiO_2. This effect, slightly more remarkable for Pt/TiO_2-A, indicates that the presence of noble metal NPs not only improved the overall photocatalytic performance (possibly due to better charge separation), but also provided surface sites ensuring a more efficient adsorption and/or a complete oxidation of the carbon-containing species involved in the reaction sequence. It is worth underlining that these positive effects of noble metal NPs on the TiO_2 surface prevail on the photoactivity decrease expected as a consequence of the decreased surface area of the materials upon noble metal NPs deposition (see Table 1).

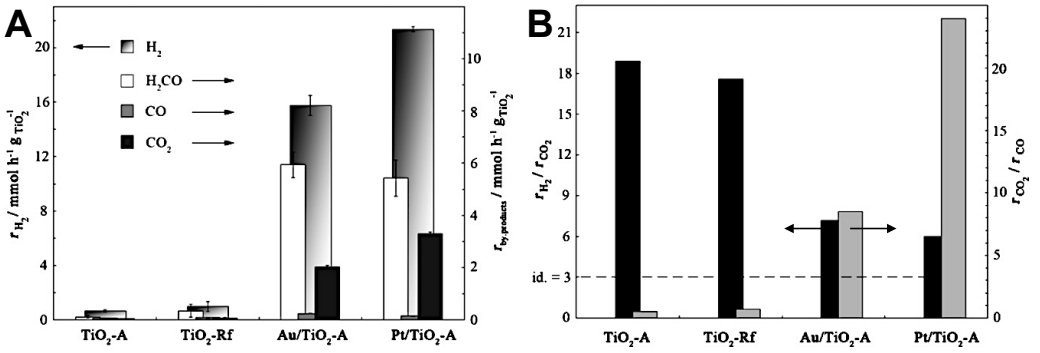

Figure 8 – (A) Hydrogen, formaldehyde, carbon monoxide and carbon dioxide production rates measured with the investigated photocatalysts in the photocatalytic steam reforming of methanol; (B) Ratios between the production rate of H_2 and CO_2 (black) and between the production rate of CO_2 and CO (gray) measured in methanol steam reforming with the investigated photocatalysts.

Fig. 8(B) reports also the r_{CO2}/r_{CO} ratio. This ratio is very important from a practical point of view, *i.e.*, when H_2 is used as a feed for fuel cells. In fact, CO, which most probably forms mainly through formic acid photocatalytic dehydration [9,35], would certainly be the most undesired by-product, being a well-known poison for Pt-based catalysts used in fuel cells. The r_{CO2}/r_{CO} ratio was lower than 1 for naked TiO_2 (Fig. 8(B)), indicating a very poor performance of these photocatalysts. However, the ratio largely increased in presence of noble metal NPs and reached higher value for Pt/TiO_2-A, thus proving an increased oxidation ability of Pt-modified titania. This can be easily evidenced also by a simple comparison between the effects of the presence of Au or Pt NPs on the rates of H_2 and CO_2 production (taking TiO_2-Rf as reference; see Table 2). In fact, although r_{H2} increased by 16 and 22 times upon TiO_2 modification with Au or Pt NPs, respectively, the corresponding r_{CO2} values were 40 and 66 times greater. Yet, superior performances of Pt/TiO_2-A powders possibly depend also on the small

diameter and narrow size distribution of Pt nanoparticles, which guarantee a better intimate metal/TiO_2 contact [36,37].

5.5 ESR Investigation

In order to study how Au and Pt affect the amount and transfer of charge carriers (e^- and h^+) and drive the photoactivity of Au and Pt/TiO_2-A, ESR spectra were acquired after UV–Vis irradiation at 130 K, either in *vacuum* ($p < 10^{-5}$ mbar) or in the presence of O_2 (p_{O2} = 10 mbar). For each sample, the absence of signals before irradiation was proved and no significant difference resulted in the ESR spectra recorded just before and 20 min after switching the light off, apart from a small decrease of the signal intensity.
After irradiation under *vacuum* all samples showed two well-separated sets of resonances (Fig. 9(A)). The signals observed at higher field were attributed to electrons trapped at different Ti^{3+} centers (Ti^{3+}[I] and Ti^{3+}[II]; see Table 3) [24,25,28,29,34-42].
In detail, the narrow signal at g = 1.988, mainly evident in TiO_2-Rf and Au/TiO_2-A, is attributable to the perpendicular g-tensor component of anatase Ti^{3+} bulk centers Ti^{3+}[I]; the corresponding $g_{||}$ resonance was not detectable due to the overlap with other resonance lines. The about symmetrical broad resonances of Ti^{3+}[II] were assigned to Ti^{3+} sites located in a disordered environment, probably nearby the surface [42].
The lower field features can be attributed to superimposed oxygen species, O^- and O^{2-} [26,43,44], the g values of which and relative amounts were calculated by signal simulation (Fig. 9(A) and Table 3). In particular, the lower field resonances observed for Pt/TiO_2-A were reproduced by five different components (Fig. 9(B) and Table 3): two overlapping axial species due to h^+ trapped at two distinct O^- sites (O^-[I] and O^-[II]) and three orthorhombic species assigned to superoxide anions with different g_{zz} values (O_2^-[I], O_2^-[II] and O_2^-[III]).
The differences in the g_{zz} component indicate that several cationic surface sites are available for the stabilization of the superoxide radical. According to the ionic model originally proposed by Kanzig and Cohen for bulk halides [45], the g_{zz} component is largely sensitive to the electric field generated by the metal cation of the adsorption site. In the case of TiO_2 the value is indicative of slight changes in Ti^{n+} charge, generated by different surrounding groups (*e.g.*, metal loaded on the surface).
The presence of O_2^- species, mainly occurring for TiO_2-Rf and Au/TiO_2-A powders, even when UV irradiation was performed in *vacuum*, may be

ascribed to the evolution of residuals OH^- groups according to the following mechanism [46]:

$h^+ + OH^- \rightarrow {}^\bullet OH$ (1)

$2\,{}^\bullet OH \rightarrow H_2O_2$ (2)

$H_2O_2 + h^+ \rightarrow O_2^- + 2H^+$ (3)

$O_2^- + h^+ \rightarrow O_2$ (4)

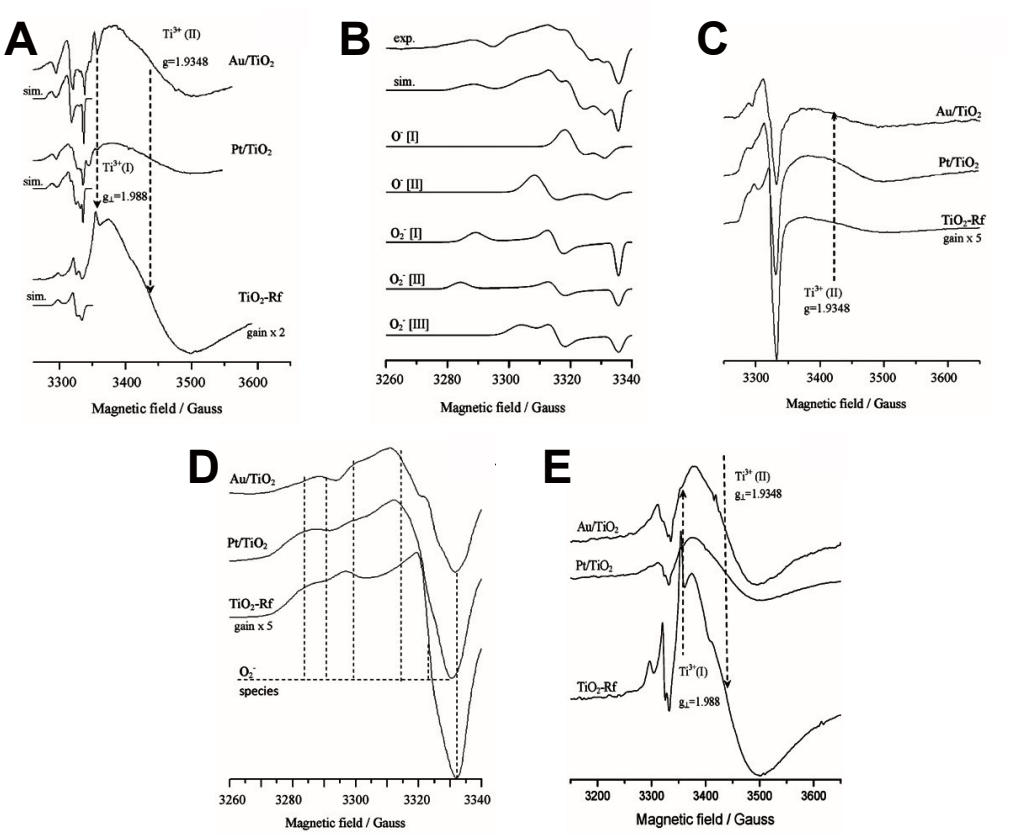

Figure 9 – (A) ESR spectra of bare and metal-loaded anatase at 130 K after UV–Vis irradiation in *vacuum* at $p < 10^{-5}$ mbar. (B) Deconvolution (simulation) of ESR signals for Pt/TiO_2-A (experimental) into O^- and O_2^- species. (C) ESR spectra after UV–Vis irradiation in presence of 10 mbar of O_2 and then under *vacuum* at $p < 10^{-5}$ mbar. (D) Magnification of the O_2^- spectral region. (E) ESR spectra after UV irradiation in the presence of 10 mbar of N_2 (saturated with vapors from a 20 vol% MeOH-H_2O solution) and subsequent evacuation at $p < 10^{-5}$ mbar.

Due to their significance in evidencing the e^-–h^+ charge separation, the amounts of the O^- species (calculated as percent of the total intensity of the $O^- + O_2^-$ signals by simulation of the normalized spectra) were determined for the different samples and reported in Table 3.

Sample	O^-(%)	O^- species	Ti^{3+} species	O^{2-} species
TiO_2-Rf	4.5	O^-: $g_\perp$ = 2.0080 $g_{\|\|}$ = 2.0016	Ti^{3+} [I]: $g_\perp$ = 1.9880 $g_{\|\|}$ = n.d. Ti^{3+} [II]: $g_\perp$ = 1.9348 $g_{\|\|}$ = 1.9045	O_2^-: g_{zz} = 2.0233 g_{yy} = 2.0094 g_{xx} = 2.0003
Au/TiO_2	5.7	O^- [I]: absent O^- [II]: $g_\perp$ = 2.0153 $g_{\|\|}$ = 2.0023	Ti^{3+} [I]: $g_\perp$ = 1.9880 $g_{\|\|}$ = n.d. Ti^{3+} [II]: $g_\perp$ = 1.9348 $g_{\|\|}$ = 1.9045	O_2^- [I]: g_{zz} = 2.0282 g_{yy} = 2.0121 g_{xx} = 2.0000 O_2^- [II]: g_{zz} = 2.0312 g_{yy} = 2.0121 g_{xx} = 2.0000 O_2^- [III]: g_{zz} = 2.0194 g_{yy} = 2.0121 g_{xx} = 2.0000
Pt/TiO_2	16.8	O^- [I]: $g_\perp$ = 2.0095 $g_{\|\|}$ = 2.0023 O^- [II]: $g_\perp$ = 2.0153 $g_{\|\|}$ = 2.0023	Ti^{3+} [I]: $g_\perp$ = 1.9880 $g_{\|\|}$ = n.d. Ti^{3+} [II]: $g_\perp$ = 1.9348 $g_{\|\|}$ = 1.9045	O_2^- [I]: g_{zz} = 2.0282 g_{yy} = 2.0121 g_{xx} = 2.0000 O_2^- [II]: g_{zz} = 2.0312 g_{yy} = 2.0121 g_{xx} = 2.0000 O_2^- [III]: g_{zz} = 2.0194 g_{yy} = 2.0121 g_{xx} = 2.0000

Table 3 – g tensor values for paramagnetic defects detected after photo-excitation in *vacuum* ($p < 10^{-5}$ mbar) on bare and metal-loaded TiO_2 powders determined by simulation of the ESR features, along with the relative contribution of O^- species (calculated as percent of the total intensity of the $O^- + O_2^-$ signals after spectra normalization).

The abundance and stability of the paramagnetic centers detected by ESR after UV–Vis irradiation are possibly related to charge separation, to their inhibited recombination and to the presence of metal or other impurities on the oxide surface [24,25,38–44].
Fig. 9(A) clearly shows that, after irradiation in *vacuum*, the concentration of e^- trapped on Ti^{3+} sites (in the range of 8.4×10^{15} – 1.2×10^{17} spin g^{-1}) always exceeded that of h^+ trapped on O^- (1×10^{13} – 7.1×10^{13} spin g^{-1}).
In detail, the highest amount of Ti^{3+} centers was detected for TiO_2-Rf powders, while it decreased for Au/TiO_2-A, becoming the lowest for Pt/TiO_2-A (Table 4). In the first case, photogenerated electrons remained at the TiO_2 surface promoting the reaction but also undergoing recombination with h^+. Otherwise, when Au or Pt was added, photogenerated electrons were readily transferred to the noble metal NPs and this occurred particularly for Pt [15].

Sample	Ti^{3+} species (spin g^{-1})		
	UV–Vis irradiation in *vacuum* ($p < 10^{-5}$ mbar)	UV–Vis irradiation $p(O_2)$ = 10 mbar	UV–Vis irradiation $p(N_2$ saturated with MeOH) = 10 mbar
TiO_2-Rf	1.6×10^{18}	4.5×10^{17}	4.9×10^{18}
Au/TiO_2-A	2.4×10^{17}	4.8×10^{16}	4.6×10^{17}
Pt/TiO_2-A	1.6×10^{17}	1.6×10^{17}	3.3×10^{17}

Table 4 – Amount of paramagnetic Ti^{3+} traps (spin g^{-1}) detected at 130 K with M/TiO_2 samples and for bare titania after UV–Vis irradiation in different conditions.

Thus, the electrons became less available to both charge trapping with Ti^{3+} centers and recombination with h^+. Indeed, electron trapping by Pt decreases the charge recombination rate and therefore favors hole trapping by O_2^-, as assessed by the higher amount of O^- species detected in Pt/TiO_2-A samples compared to Au/TiO_2-A and TiO_2-Rf (see Table 3). Therefore, loaded metals act as an electron sink, with Pt being much more efficient than Au, probably due to the larger difference between its work function φ and that of TiO_2 ($\Delta\varphi(Pt–TiO_2)$= 1.5 *vs.* $\Delta\varphi(Au–TiO_2)$ = 0.7 eV [47,48]) as already pointed out in Chapter 4. As a consequence, the probability of e^-–h^+ recombination for Pt/TiO_2-A remarkably decreases in comparison with bare TiO_2 and the quantum efficiency for H_2 production (Φ_{H2}; see Table 2) increased by more than one order of magnitude, the electrons on the metal being more readily available for H^+ reduction. The positive oxidation state of some Pt centers, as evidenced by XPS data (Fig. 7(F)), may also help to drain

electrons toward the noble metal, thus supporting the intrinsic electron scavenging action of Pt and improving charge separation.

The presence of metal NPs not only affects H_2 production, but also the product distribution of the photocatalytic oxidation of methanol (see Fig. 8(B)). In fact, methanol photoreforming on the Au/TiO_2-A catalyst gave rise to high amounts of H_2CO and CO, with low CO_2 production. Conversely, Pt/TiO_2-A induced the formation of lower amounts of H_2CO and CO and a higher CO_2 production (Fig. 8(B)). Looking at the reaction steps involved in the photocatalytic anaerobic oxidation of methanol in presence of noble metal-loaded TiO_2 [29], such performances can be associated to the amount of trapped hole centers (O^- centers), *i.e.*, the higher the amount of h^+ trapping centers detected by ESR spectroscopy, the higher the amount of fully mineralized carbonaceous products.

The ESR investigation on metal-loaded TiO_2 was performed after UV–Vis irradiation at 130 K also in presence of $p(O_2)$ = 10 mbar and subsequent removal of the residual oxygen by evacuation at $p < 10^{-5}$ mbar (Fig. 9(C) and (D)). The resonances of Ti^{3+} and O_2^- centers can be easily detected (Fig. 9(A)). The formation of superoxide species (evidenced in Fig. 9(D)) formally involved the transfer of electrons to molecular O_2, from both Ti^{3+} sites and the conduction band (e^-_{CB}), as follows [43]:

$$Ti^{3+} + O_2 \rightarrow Ti^{4+}\text{---}O_2^- \qquad (5)$$

$$Ti^{4+} + O_2 + e^-_{CB} \rightarrow Ti^{4+}\text{---}O_2^- \qquad (6)$$

According to reaction (5), the intensity of Ti^{3+} resonances for TiO_2-Rf and Au/TiO_2-A after O_2 flowing becomes much lower than in *vacuum* (see Table 4). By contrast, for Pt/TiO_2-A, the amount of Ti^{3+} centers remains more or less constant. This suggests that superoxide formation in Pt/TiO_2-A does not significantly involve Ti^{3+} centers, probably because they lie at a subsurface region.

Recently, the injection of electrons from Au NPs to TiO_2 has been suggested to be active in various photocatalytic processes such as water splitting and aerobic oxidation of alcohols [49,50]. The collective oscillation of electrons of Au particles induced by the incident light (excitation wavelengths must be close to Au surface plasmon resonance SPR band) can possibly transfer electrons from Au NPs to the TiO_2 conduction band.

Taking into account that the photoreactivity of Au/TiO_2-A could in principle be influenced by this effect, the ESR spectra of Au/TiO_2-A at 130 K were recorded under visible light irradiation (cut-off filter at 420 nm), either in *vacuum* ($p < 10^{-5}$ mbar) or in presence of $p(O_2)$ = 10 mbar. However, in all experiments no paramagnetic ESR-active species were detected. Thus,

although electron transfer cannot in principle be excluded, no electrons were trapped in TiO_2 as paramagnetic Ti^{3+} species under such conditions. Since also the contact with O_2 after visible light irradiation did not induce any electron transfer from the TiO_2 *CB* to O_2, a phenomenon usually detectable as O_2^-, it's reasonable to conclude that visible light irradiation does not induce any e^- transfer toward the *CB* and that SPR absorption in our Au/TiO_2-A sample does not contribute to its activation.
Finally, to simulate the condition experienced by TiO_2 samples during photocatalytic tests (see Section 3.6.2), TiO_2-Rf, Au/TiO_2-A and Pt/TiO_2-A underwent UV–Vis irradiation at 130 K in the presence of 10 mbar of N_2 saturated with vapors from a 20 vol% MeOH-H_2O solution. After this treatment, the excess of gas/vapors was removed by evacuation down to 10^{-5} mbar and ESR spectra were recorded afterwards (Fig. 9(E)). The very complex signal at low magnetic field is due to the superimposition of different species, mainly O^- and O_2^- centers. Regarding the possible presence of hydroxylmethyl radicals ($^{\bullet}CH_2OH$) generated by methanol photo-oxidation at the TiO_2 surface, they cannot be detected at T > 77 K [51,52]. At higher magnetic field, the intensity of Ti^{3+} active sites follows the same trend observed after irradiation in *vacuum*, that is TiO_2 > Au/TiO_2-A $\gg$ Pt/TiO_2-A, even if a considerable increase in the whole amount of Ti^{3+} traps becomes evident in all samples (Table 4). These results confirm that methanol, reacting irreversibly with the photogenerated holes, acts as an efficient h^+ scavenger, suppressing the recombination of electrons and holes at the semiconductor surface.

5.6 Conclusion & Further Work

The photocatalytic efficiency of Au and Pt/TiO_2-A for H_2 production (through photoreforming of methanol) is strongly related to their morphological and electronic properties, as well as to charge trapping phenomena and reactivity of the charge carriers. Pt/TiO_2-A displays higher activity than both Au/TiO_2-A and bare TiO_2, for both H_2 production and full CH_3OH oxidation.
The ESR study evidenced that after photo-excitation in *vacuum*, the amount of electron-traps, *i.e.*, Ti^{3+} centers, follows the order TiO_2-Rf $\gg$ Au/TiO_2-A > Pt/TiO_2-A. On the other hand, the amount of hole-traps, *i.e.*, O^- centers, shows an opposite trend, being the highest in Pt/TiO_2-A.
H_2 production is indeed associated to electron transfer phenomena, that is, photogenerated electrons in Pt/TiO_2-A are more readily transferred toward

Pt NPs, where they can reduce protons to form H_2. This indicates an overall greater ability of Pt (with respect to Au) to act as electron sink.
Yet, a smaller size of the noble metal NPs could favor the electron transfer between oxide and metal, hence improving the charge separation and the catalytic activity.
Moreover, considering the semiconductor/metal junction, an optimum NM particle decoration density would be reached when the width of the space charge layers induced by neighboring noble-metal particles overlap with each other. Hence, in view of further optimization, the photocatalytic performance of Pt/TiO_2 systems might be investigated in relation to the structural-geometrical features of the photocatalyst. A precise tuning of the dimensions and the dispersion of noble metal nanoparticles at the TiO_2 surface and, nevertheless, also a refined control of the spacing between the particles, may provide useful information on how to to enhance the photocatalytic activity of TiO_2-based materials.

5.7 References & Notes

[1] A. Naldoni, M. D'Arienzo, M. Altomare, M. Marelli, R. Scotti, F. Morazzoni, E. Selli, V. Dal Santo, Appl. Catal. B Environ. 130–131 (2013) 239.
[2] F. Zuo, L. Wang, T. Wu, Z. Zhang, D. Borchardt, P. Feng, J. Am. Chem. Soc. 132 (2010) 11856.
[3] M. Cargnello, A. Gasparotto, V. Gombac, T. Montini, D. Barreca, P. Fornasiero, Eur. J. Inorg. Chem. (2011) 4309.
[4] J. Zhang, J. Yu, Y. Zhang, Q. Li, J.R. Gong, Nano Lett. 11 (2011) 3026.
[5] D. Wang, A. Pierre, G. Kibria, K. Cui, X. Han, K.H. Bevan, H. Guo, S. Paradis, A. Hakima, Z. Mi, Nano Lett. 11 (2011) 2353.
[6] A. Ishikawa, T. Takata, J.N. Kondo, M. Hara, H. Kobayashi, K. Domen, J. Am. Chem. Soc. 124 (2002) 13547.
[7] M. Higashi, K. Domen, R. Abe, J. Am. Chem. Soc. 134 (2012) 6968.
[8] X. Chen, S. Shen, L. Guo, S.S. Mao, Chem. Rev. 110 (2010) 6503.
[9] G.L. Chiarello, M.H. Aguirre, E. Selli, J. Catal. 273 (2010) 182.
[10] N. Strataki, V. Bekiari, D.I. Kondarides, P. Lianos, Appl. Catal. B Environ. 77 (2007) 184.
[11] P. Pichat, New J. Chem. 11 (1987) 135.
[12] C.M. Wang, A. Heller, H. Gerischer, J. Am. Chem. Soc. 114 (1992) 5230.
[13] O. Rosseler, M.V. Shankar, M. Karkmaz-Le Du, L. Schmidlin, N. Keller, V. Keller, J. Catal. 269 (2010) 179.

[14] A. Gallo, T. Montini, M. Marelli, A. Minguzzi, V. Gombac, R. Psaro, P. Fornasiero, V. Dal Santo, ChemSusChem 5 (2012) 1800.
[15] J.G. Highfield, P. Pichat, New J. Chem. 13 (1989) 61.
[16] T. Hirakawa, P.R. Kamat, J. Am. Chem. Soc. 127 (2005) 3928
[17] Z. Zheng, B. Huang, X. Qin, X. Zhang, Y. Daib, M.H. Whangbo, J. Mater. Chem. 21 (2011) 9079.
[18] A. Tanaka, S. Sakaguchi, K. Hashimoto, H. Kominami, Catal. Sci. Technol. 2 (2012) 907.
[19] M. Ni, M.K.H. Leung, D.Y.C. Leung, K. Sumathy, Renew. Sustain. Ener. Rev. 11 (2007) 401.
[20] N. Zhang, S. Liu, X. Fu, Y.J. Xu, J. Phys. Chem. C 115 (2011) 9136.
[21] A.V. Korzhak, N.I. Ermokhina, A.L. Stroyuk, V.K. Bukhtiyarov, A.E. Raevskaya, V.I. Litvin, S.Y. Kuchmiy, V.G. Ilyin, P.A. Manorik, J. Photochem. Photobiol. A Chem. 198 (2008) 126.
[22] G.R. Bamwenda, S.T Subota, T. Nakamura, M. Haruta, J. Photochem. Photobiol. A Chem. 89 (1995) 177.
[23] M. D'Arienzo, J. Carbajo, A. Bahamonde, M. Crippa, S. Polizzi, R. Scotti, L. Wahba, F. Morazzoni, J. Am. Chem. Soc. 133 (2011) 17652.
[24] R. Scotti, M. D'Arienzo, A. Testino, F. Morazzoni, Appl. Catal. B Environ. 88 (2009) 497.
[25] R. Scotti, I.R. Bellobono, C. Canevali, C. Cannas, M. Catti, M. D'Arienzo, A. Musinu, S. Polizzi, M. Sommariva, A. Testino, F. Morazzoni, Chem. Mater. 20 (2008) 4051.
[26] M.V. Dozzi, L. Prati, P. Canton, E. Selli, Phys. Chem. Chem. Phys. 11 (2009) 7171.
[27] C.L. Muhich, Y. Zhou, A.M. Holder, A.W. Weimer, C.B. Musgrave, J. Phys. Chem. C 116 (2012) 10138.
[28] G. Cappelletti, S. Ardizzone, C.L. Bianchi, S. Gialanella, A. Naldoni, C. Pirola, V. Ragaini, Nanoscale Res. Lett. 4 (2009) 97.
[29] G. Wang, H. Wang, Y. Ling, Y. Tang, X. Yang, R.C. Fitzmorris, C. Wang, J.Z. Zhang, Y. Li, Nano Lett. 11 (2011) 3026.
[30] A.L. Linsebigler, G. Lu, J.T. Yates, Chem. Rev. 95 (1995) 735.
[31] G. Wang, H. Wang, Y. Ling, Y. Tang, X. Yang, R.C. Fitzmorris, C. Wang, J.Z. Zhang, Y. Li, Nano Lett. 11 (2011) 3026.
[32] G.L. Chiarello, A. Di Paola, L. Palmisano, E. Selli, Photochem. Photobiol. Sci. 10 (2011) 355.
[33] M.V. Dozzi, A. Saccomanni, M. Altomare, E. Selli, Photochem. Photobiol. Sci. 12 (2013) 595.
[34] Z. Liu, B. Guo, L. Hong, H. Jiang, J. Photochem. Photobiol. A Chem. 172 (2005) 81.
[35] G.L. Chiarello, D. Ferri, E. Selli, J. Catal. 280 (2011) 168.

[36] N. Strataki, N. Boukos, F. Paloukis, S.G. Neophytides, P. Lianos, Photochem. Photobiol. Sci. 8 (2009) 639.
[37] Y. Mizukoshi, Y. Makise, T. Shuto, J. Hu, A. Tominaga, S. Shironita, S. Tanabe, Ultrason. Sonochem. 14 (2007) 387.
[38] D.C. Hurum, K.A. Gray, T. Rajh, M.C. Thurnauer, J. Phys. Chem. B 109 (2005) 977.
[39] D.C. Hurum, A.G. Agrios, S.E. Crist, K.A. Gray, T. Rajh, M.C. Thurnauer, J. Electron. Spectrosc. Relat. Phenom. 150 (2006) 155.
[40] D.C. Hurum, A.G. Agrios, K.A. Gray, T. Rajh, M.C. Thurnauer, J. Phys. Chem. B 107 (2003) 4545.
[41] T. Berger, M. Sterrer, O. Diwald, E. Knozinger, D. Panayotov, T.L. Thompson, J.T. Yates, J. Phys. Chem. B 109 (2005) 6061.
[42] J.E. Elser, T. Berger, M. Sterrer, D. Brandhuber, J. Bernardi, O. Diwald, E. Knozinger, J. Phys. Chem. B 110 (2006) 7605.
[43] T. Berger, O. Diwald, E. Knozinger, M. Sterrer, J.T. Yates, Phys. Chem. Chem. Phys. 8 (2006) 1822.
[44] E. Carter, A.F. Carley, D.M. Murphy, J. Phys. Chem. C 111 (2007) 10630.
[45] W. Kanzig, M.H. Cohen, Phys. Rev. Lett. 3 (1959) 509.
[46] R.F. Howe, M. Grätzel, J. Phys. Chem. 91 (1987) 3906.
[47] P.C. Rusu, G. Brocks, Phys. Rev. B 74 (2006) 073414.
[48] K. Tvrdy, P.A. Frantsuzov, P.V. Kamat, Proceedings of the National Academy of Sciences of the United States of America (PNAS) 108 (2011) 29.
[49] C.G. Silva, R. Juarez, T. Marino, R. Molinari, H. Garcia, J. Am. Chem. Soc. 133 (2011) 595.
[50] D. Tsukamoto, Y. Shiraishi, Y. Sugano, S. Ichikawa, S. Tanaka, T. Hirai, J. Am. Chem. Soc. 134 (2012) 6309.
[51] O.I. Micic, Y. Zhang, K.R. Cromack, A.D. Trifunac, M.C. Thurnauer, J. Phys. Chem. 97 (1993) 13284.
[52] I.A. Shkrob, T.W. Marin, H. He, P. Zapol, J. Phys. Chem. C 116 (2012) 9450.

6. Photocatalytic Oxidation of Ammonia

6.1 Overview

Ammonia represents the major nitrogen-containing compound in livestock manure. Its photocatalytic abatement (in aqueous media) has been explored herein employing a lab-scale batch photo-reactor fed with aqueous suspensions containing NH_3 and different commercial TiO_2 powders. In a preliminary study, a systematic investigation was performed on the effects that dissolved O_2, pH, photocatalyst amount and its physico-chemical properties have on both ammonia conversion and selectivity toward the main oxidation products (N_2, NO_2^- and NO_3^-). In a following step, the study focused on the use of TiO_2 P25 powders modified by deposition of metal nanoparticles and the relative effects on the reaction mechanism were assessed. The data and results presented in this chapter have been published (and patented) in ref. [1-3].

6.2 Aim

Although livestock manure can improve the quality of soil and is widely used, together with chemical fertilizers, to boost agricultural productivity, their overuse generates a dangerous accumulation of nitrogen-containing species in soil and groundwater [4]. Such an accumulation accelerates eutrophication phenomena in groundwater, leads to depletion of dissolved oxygen and increases biological oxygen demand, besides presenting acute toxicity to human health.

Therefore, the European Economic Community (EEC) issued the 1991/676/EEC Act, imposing specific management procedures to regulate the spreadable amount of manure and to specify the correct period of the year for field fertilization. In this view, the amount of nitrogen that can be spread as fertilizer was reduced from 340 to 170 kg per hectare (*i.e.*, 10,000 m^2) per year.

In such a situation, especially for areas characterized by a high density of animal farms (*e.g.*, Northern Italy [5]), mandatory was and still is the identification of solutions ensuring suitable disposal of nitrogen.

Several methods have been explored, including biological processes with nitrification-denitrification cycles, breakpoint chlorination, ion exchange, air stripping and chemical oxidation [6,7]. The efficiency of biological treatments mainly depends on the operating temperature, bacterial type, dissolved oxygen, carbon source, pH and concentration of toxic substances, and can therefore hardly cope with the intrinsic changes in physico-chemical properties of wastewaters [8]. Moreover, by employing these processes, ammonia is often not completely removed and nitrogen-containing compounds persist within the waste stream after the treatment. Furthermore, some of the mentioned processes, though able to remove pollutants from manure, finally just concentrate them within a new waste stream, for which a subsequent treatment is still necessary to ensure the complete elimination of toxic species.

Hence, the photocatalytic oxidation of nitrogen-containing effluents has been recently investigated as an unconventional way to detoxify water from ammonia in a single-step process. A great variety of hazardous substances can be efficiently removed via photocatalytic mineralization on TiO_2 [9]. The decomposition of gaseous ammonia was already studied by Mozzanega *et al.* at the end of the '70s on UV-irradiated anatase TiO_2 [10] and is still object of investigation [11,12]. The photocatalytic oxidation of ammonia in the aqueous phase was also explored as an advanced oxidation process (AOP) involving photoproduced hydroxyl radicals as primary oxidants able to transform NH_3 mainly into nitrite and nitrate anions [13–16]. However, since such species are not less noxious than ammonia itself, a selective photocatalytic oxidation into N_2 would be much more desirable [17,18]. Thus, many efforts were devoted to highlight the mechanism of ammonia photo-oxidation in relation to products distribution [11,13,19-23], by coupling NH_3 abatement with H_2 production [24-27] or NO reduction [21,28-30] and by tailoring the process toward a selective conversion into innocuous N_2 [1,14,15,31-33].

In a first study we systematically investigated the influence of some experimental conditions (NH_3 and O_2 concentration, pH, photocatalyst amount and its physico-chemical features) on NH_3 conversion and selectivity toward its main oxidation products [1,2]. Afterwards, the effects of metal nanoparticles (NPs) deposition on TiO_2 P25 were investigated, focusing in particular on how type and amount of metal NPs affect the reaction pathways.

6.3 Photocatalysts Characterization

All photocatalysts tested for this study were commercially available TiO_2 powders. P25 TiO_2 (Degussa-Evonik), a nanocrystalline powder composed of 80 % anatase and 20 % rutile, was used as reference photocatalyst. The other materials comprised samples A1 (Alpha Aesar) and A2 (Aldrich), mainly composed of anatase, A3 (Mirkat), a pure anatase sample, and finally R1 (Aldrich) and R2 (Millenium) consisting of pure rutile. Aside from A3, that was characterized through this work, specific surface area (SSA) and phase composition of all the others were determined by BET and XRD analyses performed in previous studies [18–20] and are herein summarized in Table 1.

Sample	Origin	Ref.	SSA ($m^2\ g^{-1}$)	Crystal phase (wt%)	
				Anatase	Rutile
P25	Degussa	[19]	48	80	20
A1	Alpha Aesar	[19]	235	90	10
A2	Aldrich	[20]	152	98	2
A3	Mirkat	-	178	100	-
R1	Aldrich	[20]	140	-	100
R2	Millenium	[18]	12	-	100

Table 1 – Specific surface area (SSA) and phase composition of the investigated TiO_2 photocatalysts.

Concerning metal-loaded powders, the preparation of which is described in Section 3.1.2, XRD and BET analyses confirmed that the metal NPs deposition did not affect the phase composition and surface area of TiO_2 P25. In fact, a mixed phase composition of 80:20 anatase-rutile and a SSA of 48 $m^2\ g^{-1}$ were measured for metal-loaded powders, in agreement with the results obtained for untreated P25 (see Table 1 in Chapter 4). HAADF-STEM micrographs for 0.05Pt and 0.5Pt showed that 4–5 nm spherical Pt NPs were homogeneously deposited on the photocatalyst surface, with a higher tendency for NPs aggregation for 0.5Pt powders, having a ten-fold higher Pt loading, as evidenced in Fig. 1. On the other hand, no metal NPs aggregation was observed for 1Au and 1Ag, as already reported in a previous paper from our research group [34]. The gold-containing sample exhibited bigger NPs

(3–8 nm on average, along with few particles with dimensions up to 20 nm in diameter) than the silver-modified powders (with 1.5–3 nm Ag NPs).
The absorption spectra of the investigated photocatalysts are collected in Fig. 2. All powders exhibit an optical absorption onset at $\lambda \sim 400$ nm, owing to TiO_2 band gap excitation. The feature observed at *ca.* 550 nm for Au-modified samples corresponds to the typical band for gold plasmon resonance (see UV-Vis DR spectra in Fig. 2(A)). This band, already observed for powders discussed in both Chapter 4 and 5, arises from the collective oscillation of free electrons induced by interaction with an incident electromagnetic radiation whose wavelength far exceeds the particles size.
Ag-modified powders (Fig. 2(A)) exhibited an optical absorption similar to that of Au/TiO_2, though having a maximum of absorption at slightly longer wavelength (*i.e.*, 570 nm).
Finally, Pd- and Pt-modified powders showed a broad, almost featureless optical absorption extending over the entire visible region (Fig. 2(B) and (C)). Moreover, the absorption became progressively more intense with increasing the loading of Pt and Pd NPs on TiO_2, confirming the actual deposition of different loading of metal NPs.

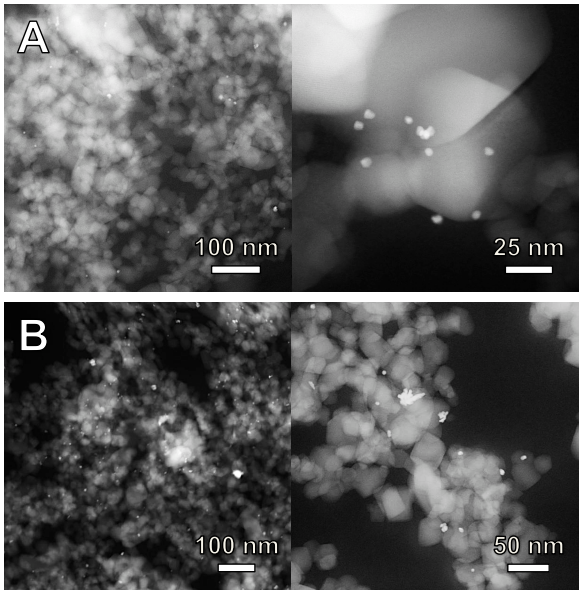

Figure 1 – HAADF-STEM images for (A) 0.05 and (B) 0.5 wt% Pt-modified TiO_2 P25.

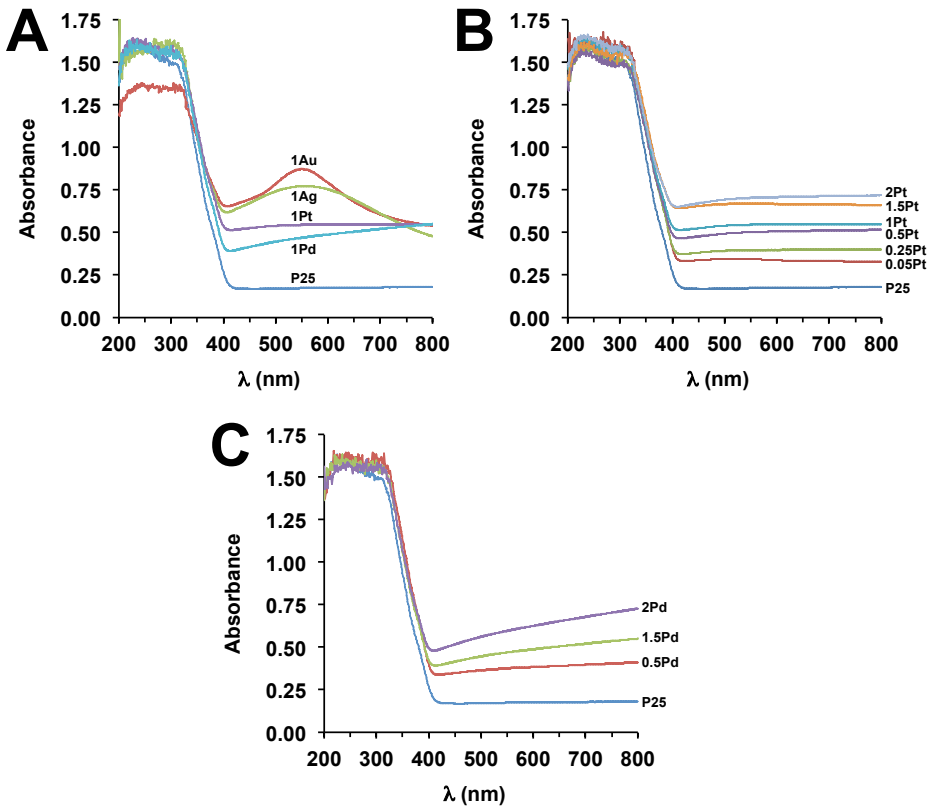

Figure 2 – UV-Vis DR spectra of (A) naked, Au-, Ag-, Pt- and Pd-modified TiO_2 P25 (1 wt% metal loading); (B) Pt-modified and (C) Pd-modified TiO_2 P25 with different loadings.

6.4 Bare TiO_2 Photocatalysts

Details concerning the experimental set-up and analytical methods are reported in Section 3.4.3. Preliminary experiments, carried out by irradiating ammonia solutions with UVA light in the absence of TiO_2 powder, excluded that direct NH_3 photolysis takes place. In fact, the direct photolysis of ammonia is reported to occur under more severe irradiation conditions [15] and therefore it does not take place under the low-intensity UVA irradiation adopted for this study.

Furthermore, negligible ammonia adsorption at the semiconductor surface occurred in the dark for stirred suspensions containing 1.0 g L^{-1} of TiO_2 P25 at pH 10.5. This is not unexpected, because ammonia is prevalently in its

neutral form at this pH, whereas the semiconductor surface is negatively charged, its point of zero charge being around 6.25 [22].
The effect of raising the temperature of the reactor from 30 up to 60 ˚C was also checked. Although temperature is expected to affect both adsorption-desorption equilibrium and intrinsic reaction rates, very little variation in ammonia conversion profiles was observed when studying the reaction at higher temperature. Therefore, the experiments were all carried out at 30 ˚C.

6.4.1 Bubbling Gas & Flow Rate

The rate of ammonia photocatalytic abatement is closely related to the concentration of O_2 within the reaction medium, as shown in Fig. 3(A). Although similar conversions were attained (with TiO_2 P25) when bubbling air or pure O_2, ammonia underwent negligible abatement either when bubbling N_2 or under air atmosphere without any bubbling. Thus, the concentration of O_2 plays a significant role, as already reported [16,18,38].

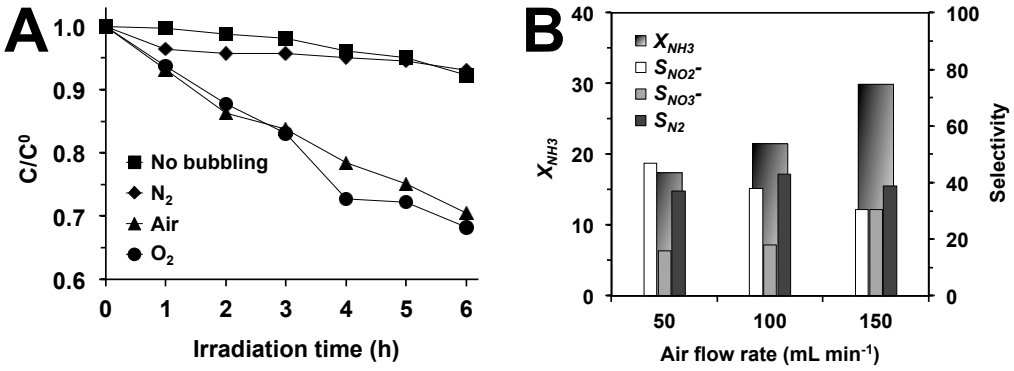

Figure 3 – (A) Ammonia abatement *vs.* irradiation time profiles for photocatalytic runs carried out in the absence of bubbling gas or under N_2, air or O_2 bubbling at 150 mL min^{-1}; 0.1 g L^{-1} P25 TiO_2, $[N]_i$ ~ 100 ppm, pH 10.5. (B) Percent ammonia conversion and selectivity toward ammonia photo-oxidation products after 6 h of irradiation at different flow rates of air, with 0.1 g L^{-1} of P25 TiO_2.

Notoriously, the ability of adsorbed O_2 in capturing *CB* electrons is rate determining in heterogeneous photocatalysis [39] and the separation of charge carriers increases in the presence of O_2 [17]. This occurs because photo-promoted electrons react with O_2 to give $O_2^{\bullet-}$, with the resulting consumption of the former. This reaction partially suppresses the recombination of electron and hole couples, indirectly enhancing the rate of ammonia oxidation by holes or hydroxyl radicals (the latter are generated through electron transfer from water molecules or hydroxyl anions to *VB* holes).

As shown in Table 2, quite similar results were obtained when bubbling air and pure O_2, indicating that bubbling pure O_2 rather than air does not produce any substantial advantage in the photocatalytic abatement of NH_3. Moreover, the effects of saturating the suspension with another oxidizing gas, *i.e.*, N_2O, were also explored, adopting experimental conditions similar to those reported in ref. [14]. However, NH_3 photo-oxidation was completely suppressed when bubbling a 10 vol% N_2O-He gas mixture (with the same flow rate as in previous experiments, *i.e.*, 150 mL min^{-1}).

Fig. 3(B) shows the effect of the flow rate of air on ammonia photo-oxidation. Clearly, the higher the flow rate, the higher the conversion of ammonia and, at the same, an increase of the selectivity toward nitrates was observed. This result might be regarded to a larger amount of dissolved O_2 when flowing air at higher flow rate, so that the availability of *VB* holes for oxidizing ammonia is increased as a consequence of a more efficient consumption of *CB* electrons through reaction with O_2 molecules. Moreover, the selectivity to N_2, S_{N2}, only slightly decreased at the highest flow rate. For this reason, an air flow rate of 150 mL min^{-1} is undoubtedly the best condition, leading to both high conversion of NH_3 and selectivity toward N_2.

$[N]_i$ (ppm)	Gas	pH	X_{NH3}	S_{NO2}-	S_{NO3}-	S_{N2}
100	O_2	10.5	32	31	24	44
100	Air	10.5	35	27	31	42
1000	Air	10.5	11	39	1.0	60
100	Air	3.5*	2.2	-	-	-
100	Air	6.5*	9.4	-	-	-
100	Air	7.5*	9.5	-	-	-
100	Air	11.5#	23	91	7.0	2.0
100	Air	12.5#	26	98	2.0	0

Table 2 – Ammonia conversion (X_{NH3}) and selectivity (S_Y) toward ammonia oxidation products (Y = NO_2^-, NO_3^-, N_2) after 6 h-long irradiation in aqueous suspensions containing 0.1 g L^{-1} of P25 TiO_2 and two different initial concentrations of nitrogen $[N]_i$ at different initial pH (pH was adjusted by adding *$HClO_4$ or #KOH). Gas flow rate 150 mL min^{-1}.

6.4.2 NH_3 Concentration & TiO_2 P25 Amount

Ammonia conversion, X_{NH3}, and the selectivity towards different ammonia oxidation products, S_Y, were found to depend on the initial concentration of nitrogen $[N]_i$ (see Table 2). As frequently found in photocatalysis, the percent conversion of ammonia decreased with increasing $[N]_i$ from 100 to 1000 ppm. Conversely, the selectivity toward N_2 showed an opposite trend, *i.e.*, S_{N2} was much higher for high initial concentration of N, possibly as a consequence of an increased probability of N_2 production resulting from redox reactions involving ammonia and the other intermediates containing nitrogen, in different oxidation states, adsorbed at the photocatalyst surface. In order to attain a reasonable ammonia conversion after 6 h irradiation, the initial concentration of nitrogen was fixed at ≈ 100 ppm.

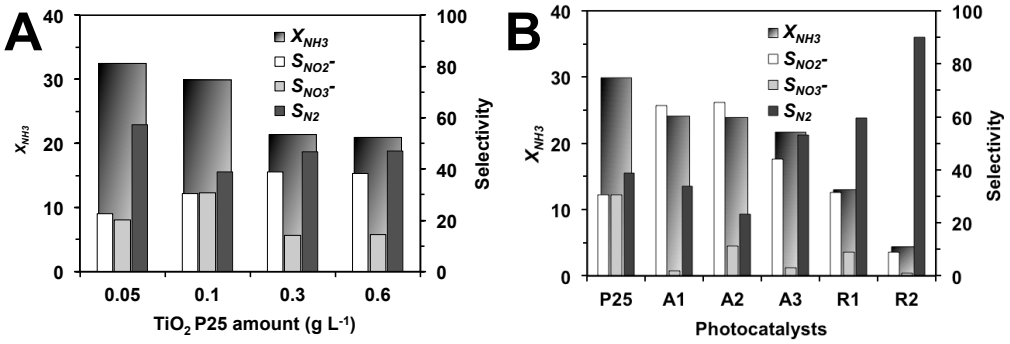

Figure 4 – Ammonia conversion and selectivity toward photo-oxidation products after 6 h irradiation with (A) different TiO_2 P25 amounts in the irradiated suspensions or (B) in the presence of 0.1 g L^{-1} of different TiO_2 photocatalysts. Air bubbling at 150 mL min^{-1}; $[N]_i$ ~ 100 ppm; pH 10.5.

The effect of the photocatalyst amount was also investigated in the range of 0.05–0.6 g L^{-1}. As shown in Fig. 4(A), the highest photocatalytic activity in terms of X_{NH3} was obtained in the presence of around 0.05–0.1 g L^{-1} of TiO_2 P25. For larger TiO_2 amounts, lower X_{NH3} values were observed, probably because of a decrease of irradiation efficiency. In other words, when the content of TiO_2 was increased, also the fraction of incident light absorbed by the semiconductor increased progressively up to a full light absorption. However, at the same time also the fraction of incident light that underwent scattering increased, leading to an overall decrease of the reaction rate. Finally, selectivity toward N_2 reached the maximum for 0.05 g L^{-1} of TiO_2.

6.4.3 Effects of pH

Ammonia photo-oxidation tests on TiO_2 P25 were performed at different pH, in a range from 3.5 to 12.5 (pH was adjusted by adding small amounts of concentrated $HClO_4$ or KOH aqueous solutions). As shown in Table 2, the most suitable pH corresponded to the natural pH of the suspensions (*ca.* 10.5), leading to the highest X_{NH3}. The photocatalytic activity was clearly related to the NH_3/NH_4^+ molar ratio in the aqueous phase and the photocatalyst surface charge, as they both depend on pH. At pH higher than 10.5, a decrease of NH_3 photo-oxidation rate was observed, probably due to competitive adsorption of hydroxide anions at the photocatalyst surface. The hindered photo-oxidation of nitrite to nitrate ions observed under extremely alkaline conditions should be also related to this effect, leading to selectivity to nitrite of *ca.* 90-100 % (*i.e.*, no nitrate ions or N_2 formation). This may suggest that adsorption of nitrite ions at the photocatalyst surface represents an essential step for their conversion into nitrates. Under neutral or acidic conditions, *i.e.*, at pH ≤ 7.5 (adjusted by adding $HClO_4$), the rate of ammonia photo-oxidation dramatically decreased. Here, different ionic species are expected to affect the photocatalytic activity because of their competitive adsorption [40]. Summarizing, the highest rate of ammonia photo-oxidation was obtained at natural pH, which is the condition where no additional species, *i.e.*, $HClO_4$ or KOH, were added for adjusting the pH of the suspension.

6.4.4 Different Commercial TiO_2 Powders

The results discussed so far were all obtained for TiO_2 P25 powders. Therefore, a series of other commercial TiO_2 powders (see Table 2) were also tested for ammonia oxidation, in order to study the dependence of this photocatalytic reaction on phase composition (anatase or rutile) and surface properties of the semiconductor. All experiments were performed at natural pH (around 10.5 for all photocatalysts) and by bubbling air at 150 mL min^{-1}. According to the results shown in Fig. 4(B), TiO_2 P25 possesses the highest photocatalytic activity, though showing a relatively low selectivity to N_2. As speculated by many scientific papers in the field [36,38,41], the high photocatalytic activity of P25 can be ascribed to its mixed anatase-rutile phase, for which a more efficient charge carriers separation would be attained because of a suitable alignment of anatase and rutile *CB*.
With the only exception of P25, the photoactivity generally increased with increasing the photocatalyst surface area (see Fig. 4(B) and Table 2). All anatase samples showed higher photoactivity compared to rutile samples, as

already observed for other photocatalytic reactions [36], along with high selectivity to nitrites (40–60 %). Furthermore, although less active than P25, high surface area anatase A3 ensured a relatively high selectivity to N_2.

6.4.5 NH_3 Photo-Oxidation on Bare TiO_2

Ammonia photocatalytic oxidation to nitrate ions most likely occurs through the formation of nitrite ions. Fig. 5(A) shows an example of ammonia, nitrite and nitrate ions concentration *vs.* time profiles obtained with TiO_2 P25.

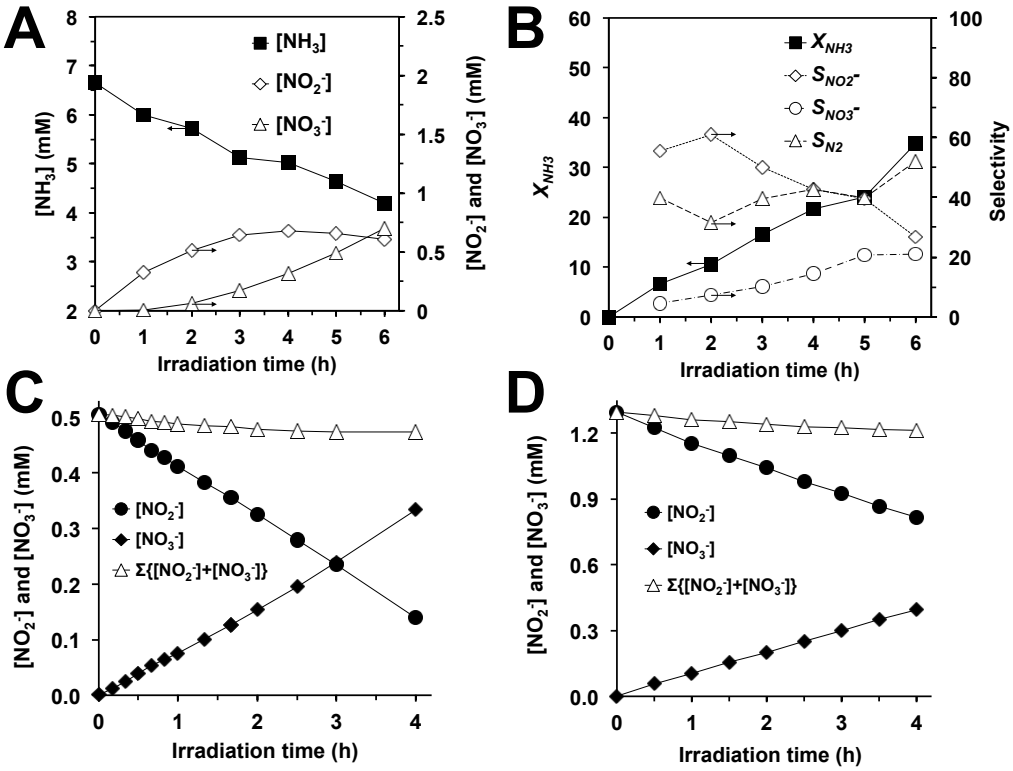

Figure 5 – (A) Ammonia, nitrite and nitrate ion concentrations and (B) ammonia conversion and selectivity *vs.* irradiation time; 0.1 g L^{-1} TiO_2 P25, $[N]_i \sim 100$ ppm, pH 10.5, air bubbling at 150 mL min^{-1}. Nitrite and nitrate ion concentration *vs.* irradiation time profiles in aqueous suspensions initially containing (C) 25 ppm and (D) 60 ppm of NO_2^- ions and 0.1 g L^{-1} of TiO_2 P25; pH 6.0 , air bubbling at 150 mL min^{-1}.

The concentration of the nitrite ions generally increased during irradiation up to a plateau (after *ca.* 3 h), when the rate of photo-production of nitrite ions from ammonia became equal to their oxidation rate into nitrates. Thus, the selectivity values widely vary during the experiments (Fig. 5(B)), with only the selectivity to nitrate ions, S_{NO3}-, constantly increasing during the runs. On the other hand, S_{NO2}– starts to decrease already after 2 h irradiation.

In order to investigate the photocatalytic oxidation of nitrite into nitrate ions, photocatalytic runs were carried out starting from suspensions containing $NaNO_2$, under standard experimental conditions (TiO_2 P25 0.1 g L^{-1}, air bubbling at 150 mL min^{-1}, natural pH *ca.* 6.0). A 70 and 35 % decrease of nitrite concentration was attained after 4 h irradiation, this when the initial concentration was 25 and 60 ppm, respectively. As shown in Fig. 5(C) and (D), the nitrite into nitrate photocatalytic oxidation occurred at constant rate and the total anion concentration, *i.e.*, $\Sigma\{[NO_2^-]+[NO_3^-]\}$, only slightly decreased under irradiation, always remaining below *ca.* 6 % of the initial nitrogen content. A contribution to this phenomenon might be due to nitrate ions adsorption at the TiO_2 surface. Moreover, results shown in Fig. 5(C) and (D) demonstrate that nitrates did not undergo photocatalytic reduction into nitrite [42,43] and exclude that N_2 could be produced, in the absence of ammonia, by photocatalytic reduction of nitrite ions.

6.5 Metal-Loaded TiO_2 P25

Ammonia conversion and selectivity toward the different photo-oxidation products (*i.e.*, NO_2^-, NO_3^- and N_2) measured for metal-loaded TiO_2 powders are collected in Fig. 6-8.

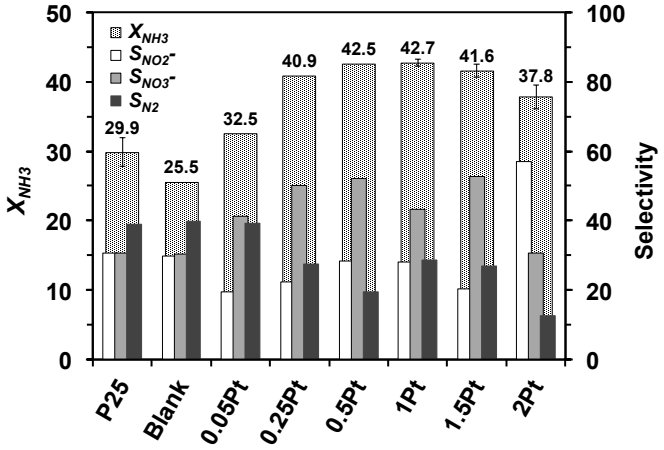

Figure 6 – Ammonia conversion and products selectivity measured after 6 h irradiation for P25, Blank and Pt-modified photocatalysts with different NPs loadings.

Aside from Au-modified TiO_2 (sample 1Au, Fig. 8), all metal-modified photocatalysts clearly exhibited a higher photoactivity in ammonia oxidation compared to that of naked P25 and Blank samples. Concerning bare powders, Blank sample was slightly less photoactive than untreated P25

(Fig. 6), though showing quite similar selectivity values. The increased X_{NH3} observed when employing metal-modified powders can be ascribed to a more effective separation of e^-–h^+ couples induced by the presence of metal NPs, the latters working as electron trap at the photocatalyst surface [44]. In particular, Pt NPs greatly affected both ammonia conversion and product selectivity (Fig. 6). X_{NH3} showed a bell-shaped trend with increasing the loading of Pt, with a maximum measured for the 1Pt sample. However, the presence of Pt NPs led to a significant drop of S_{N2}, even at low Pt loadings (*i.e.*, 0.25Pt), possibly due to the high oxidative power of Pt/TiO_2 powders, all of them producing larger amounts of nitrite and nitrate ions compared to naked TiO_2.

Sample	X_{NH3}	S_{N2}	r_{NO2}- (µmol h^{-1})	Φ_{N2}
P25	29.9	38.9	195	4.0
Blank	25.5	39.7	-	3.5
0.05Pt	32.5	39.2	234	4.4
0.25Pt	40.9	27.6	-	3.9
0.5Pt	42.5	19.5	-	2.9
1Pt	42.7	28.6	269	4.2
1.5Pt	41.6	26.9	-	3.9
2Pt	37.8	12.5	154	1.6
0.5Pd	32.7	44.0	-	5.0
1Pd	40.6	41.2	6	5.8
2Pd	33.1	26.8	-	3.1
1Au	27.0	0	9	0
1Ag	45.5	11.9	358	1.9

Table 3 – Ammonia conversion, selectivity to N_2, rate of photocatalytic oxidation of nitrite ions and apparent photon efficiency of NH_3 photo-oxidation to N_2 for all investigated metal-modified TiO_2 powders in comparison with both unmodified and Blank P25 TiO_2.

Pd-modified photocatalysts showed a similar trend (see Fig. 7), with a maximum of ammonia conversion observed, also in this case, for a 1.0 wt% loading, *i.e.*, for sample 1Pd. However, 0.5Pd and 2Pd were not as photoactive as Pt-modified powders with the same metal loadings (Fig. 6

and 7). Nevertheless, though less photo-active than 1Pt and 1Ag in ammonia conversion (Fig. 8), 1Pd exhibited the highest selectivity toward N_2, even slightly better than that of untreated P25. This feature makes Pd-modified TiO_2 an interesting platform for exploring environmentally friendly ammonia conversion into N_2. A S_{N2} value around 44 % was measured also for 0.5Pd, although it only showed a relatively low ammonia conversion.

A comparison between ammonia conversion and selectivity values measured for photocatalysts with the same loading (1.0 wt%) of different metal NPs is shown in Fig. 8. 1Ag was found to be the most active photocatalyst in terms of ammonia conversion, with a X_{NH3} value 1.5 times higher than that of bare P25, despite producing huge amounts of nitrite and nitrate ions, the latter being noxious species.

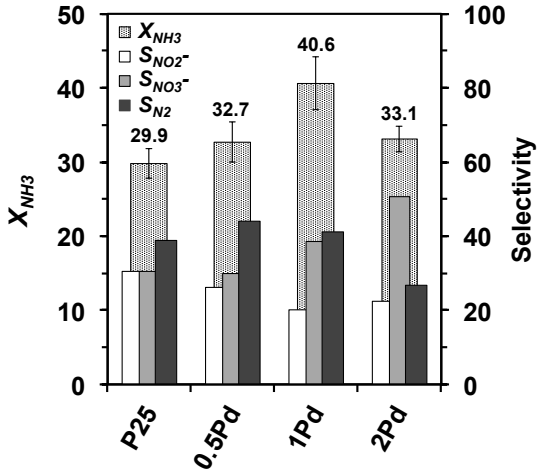

Figure 7 – Ammonia conversion and products selectivity measured after 6 h irradiation for Pd-modified photocatalysts with different NPs loadings.

In order to exclude any reaction due to the presence of silver nanoparticles as such and not involving TiO_2 band gap excitation, the extent of NH_3 oxidation was checked either *i)* in stirred water suspensions containing 1Ag powders under exactly the same conditions employed for the photocatalytic runs but in the absence of irradiation, and *ii)* in aqueous suspensions containing ammonia and 110 mg L^{-1} of silver particles, prepared by reduction of $AgNO_3$ with a stoichiometric excess of $NaBH_4$, both in the absence and in the presence of irradiation, under conditions otherwise identical to those employed in the photocatalytic runs. For all experiments, the concentration of ammonia remained unchanged, aside from a small amount that was stripped by the flow of air and collected within the trap (see Section 3.4.3), and no nitrite and nitrate ions were detected in the

aqueous phase, confirming that Ag NPs were (photo)active only when deposited on TiO_2.

As shown in Fig. 6-8, the conversion of ammonia followed the trend 1Ag > 1Pt > 1Pd > P25 > 1Au, which was also mirrored by an increase of selectivity to NO_3^-. Surprisingly, the presence of Au NPs on TiO_2 not only totally suppressed S_{N2}, but also lowered X_{NH3}. These results are unexpected since gold NPs deposited on titania usually induced beneficial effects for both down-hill [44,45] and up-hill [34,45,46] photocatalytic reactions, as also discussed through Chapter 4 and 5.

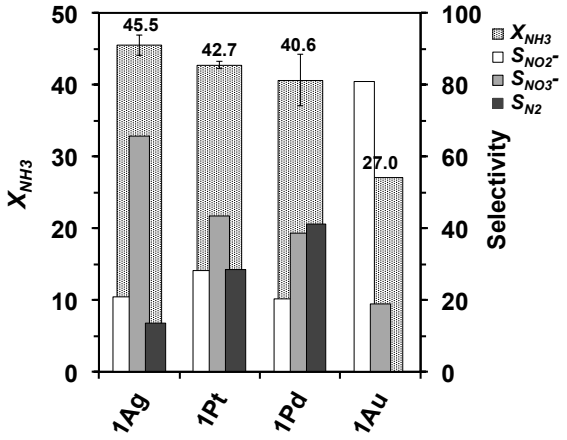

Figure 8 – Ammonia conversion and products selectivity measured after 6 h irradiation for different metal-loaded photocatalysts (metal NPs loading of 1 wt%).

The effect of metal NPs on S_{N2} can be discussed also in terms of Φ_{N2}, that is the apparent photon efficiency of NH_3 photo-oxidation into N_2 (see Table 3). Φ_{N2} can be calculated according to the following equation:

$$\Phi_{N_2} = \frac{3 \times S_{N_2} \times n_{NH_3\ abated}}{2 \times I \times t} \times 100 \qquad (1)$$

where S_{N2} is the selectivity to N_2 evaluated at the end of the runs (*i.e.*, after 6 h), $n_{NH3\ abated}$ represents the amounts (moles) of NH_3 that underwent photo-oxidation, I corresponds to the irradiation intensity and t is the irradiation time (6 h). In view of a real application of this process, both high X_{NH3} and S_{N2} are necessary. Therefore, the most promising materials would be Pd-modified powders (see Table 3) and, in particular, sample 1Pd, which exhibits a relatively high ammonia conversion (*ca.* 41 %) along with the highest apparent photon efficiency (*ca.* 5.8 %) in N_2 formation.

6.5.1 NH_3 Concentration vs. Time Profiles

As discussed in Section 6.4.5, when unmodified TiO_2 P25 is employed as photocatalyst, the concentration of nitrite ions increases progressively until reaching a plateau after *ca.* 4 h. This occurs when the rate of photocatalytic production of nitrites from ammonia becomes equal to the rate of nitrite oxidation into nitrate ions.

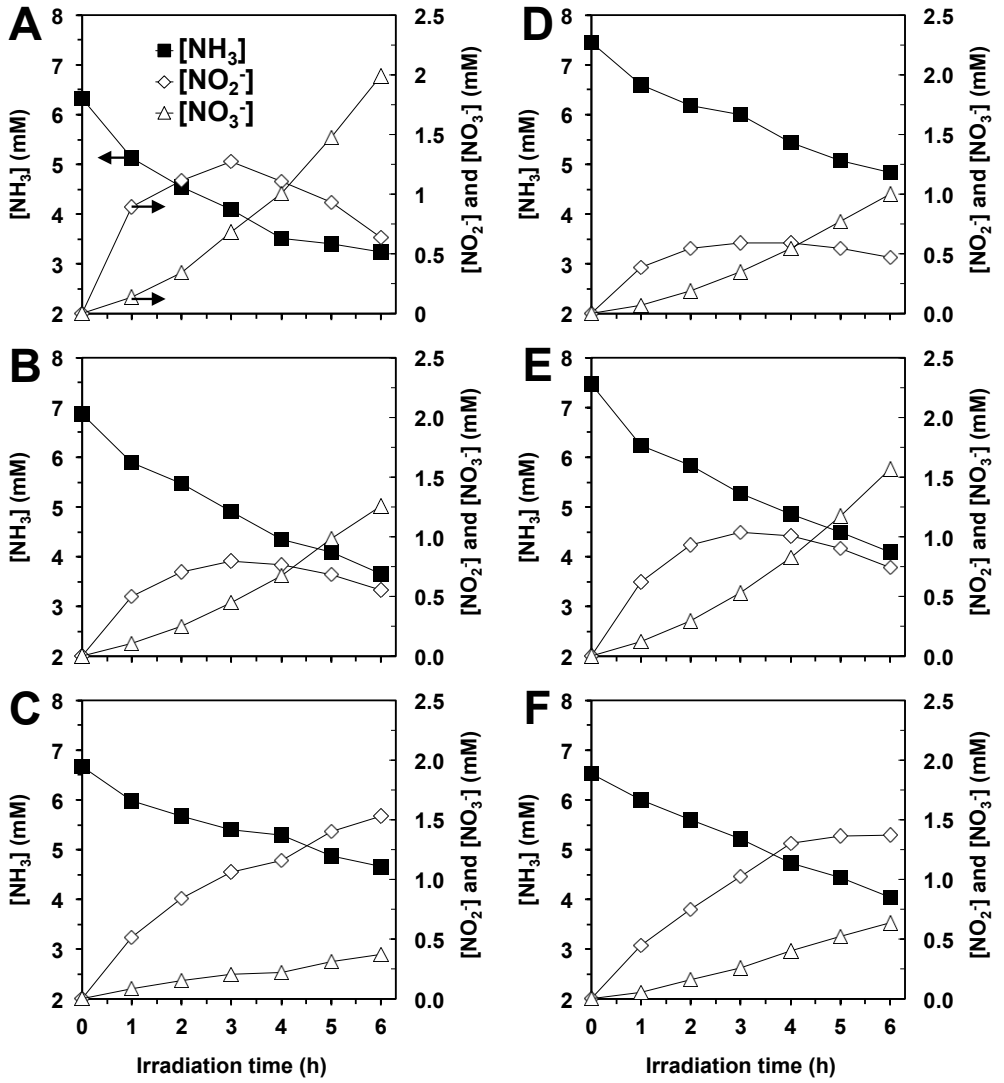

Figure 9 – Concentration of nitrogen-containing species *vs.* time profiles for different metal-loaded P25 TiO_2 powders: (A) 1Ag; (B) 1Pd; (C) 1Au; (D) 0.05Pt; (E) 1Pt; (F) 2Pt.

Some examples of concentration of nitrogen-containing species *vs.* irradiation time profiles are shown in Fig. 9 for different metal-loaded photocatalysts. These plots provide some useful information to understand the effects that different metal NPs deposited onto TiO_2 may have on the mechanism of NH_3 photocatalytic oxidation.

Ag-modified powders showed profiles quite similar to that observed for naked P25 TiO_2, indicating that ammonia underwent photo-oxidation to nitrite ions, the latter finally undergoing further photo-oxidation into nitrate ions (Fig. 9(A)). In other words, these steps occur as consecutive reactions and S_{NO2}- decreased during irradiation, whereas S_{NO3}- greatly increased in the same time. For 1Ag, S_{N2} value was almost constant during the run (around 10 %), though pretty lower than that obtained for naked TiO_2 P25 (~ 40 % after 6 h). Samples 1Pd and 1Pt exhibited concentration *vs.* time profiles similar to those observed for 1Ag (Fig. 9(B) and (E)). Overall, both 1Pd and 1Pt appeared less photo-active than 1Ag although the former, *i.e.*, 1Pd, produced lower amounts of oxidized anions, thus showing higher selectivity to N_2, as already pointed out in the previous section. Concerning the effects of different loading of Pt NPs, the concentration *vs.* time profiles shown in Fig. 9(D)-(F) confirm that a loading of Pt NPs of *ca.* 1.0 wt% guarantees best results in terms of ammonia abatement and nitrite into nitrate conversion.

Interestingly, gold-containing powders exhibited unexpected photocatalytic features (Fig. 9(C)), not only because X_{NH3} widely dropped down upon Au NPs deposition, but also because the concentration of nitrite and nitrate ions simultaneously increased during irradiation, with the concentration of NO_2^- being always higher than that of NO_3^-. Moreover, the concentration of nitrite ions continuously increased during the runs, while the selectivity to NO_2^- and NO_3^- remained almost constant, S_{NO3}- being around 20 %, S_{NO2}- *ca.* 80 % and S_{N2} dramatically suppressed.

These results clearly highlight that the type of metal NPs deposited on titania has wide effects on ammonia conversion and product selectivity, suggesting that different photocatalytic pathways may prevail in the presence of certain metal NPs rather than in the presence of others.

6.5.2 Photocatalytic Oxidation of Nitrite Ions

In order to rationalize the different shapes of the concentration *vs.* time profiles reported in Fig. 9, one of the step of ammonia photo-oxidation, *i.e.*, the photocatalytic conversion of nitrite into nitrate anions, was investigated separately, starting from $NaNO_2$ solutions at pH *ca.* 10.5, hence under the same experimental conditions employed in the photocatalytic oxidation of ammonia. The pH was adjusted by adding small amounts of a concentrated KOH aqueous solution.

Nitrite into nitrate photocatalytic oxidation occurred at almost constant rate for all investigated photocatalysts, with the total anions concentration in the

aqueous phase, *i.e.*, $\Sigma\{[NO_2^-]+[NO_3^-]\}$, only slightly decreasing (by less than 5 % in 6 h) during the experiments.

As an example, the concentration *vs.* time profile observed for 1Ag is shown in Fig. 10(A). These results excluded that N_2 could be produced by nitrite photocatalytic reduction in the absence of ammonia [42,42,47,48].

For unmodified P25, the photocatalytic oxidation of nitrite into nitrate ions occurred at constant rate and was also almost quantitative, though proceeding at a slightly lower rate compared to that measured with 1Ag.

Concerning Pt-loaded powders, the rate of photocatalytic conversion of nitrite into nitrate ions showed a bell-shaped trend with increasing the Pt loading (see Table 3), similar to that observed for ammonia photocatalytic oxidation (Fig. 6), with the highest rate measured for sample 1Pt. This indicates that Pt NPs on TiO_2 may contribute in activating titania in the same way (*e.g.*, by increasing the photoproduced charge separation) for both oxidation reactions.

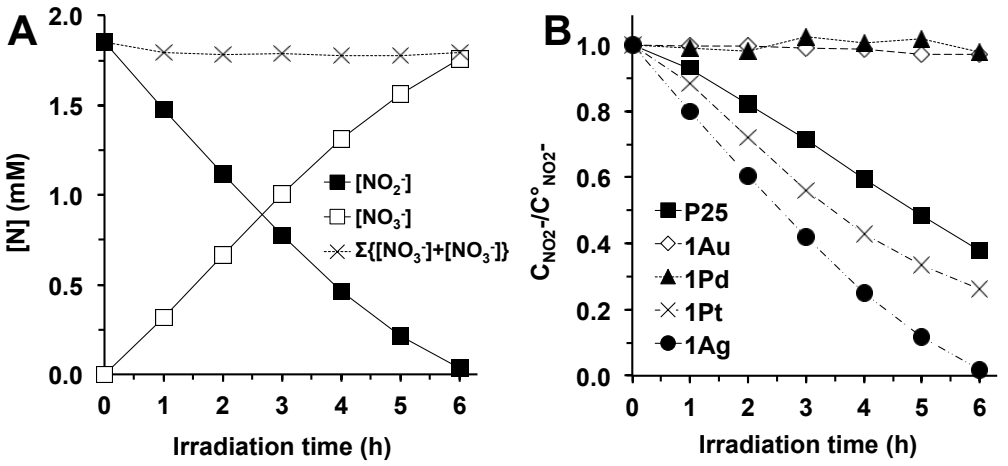

Figure 10 – (A) Nitrite and nitrate ions concentration *vs.* irradiation time profiles in aqueous suspensions initially containing nitrite ions at pH *ca.* 10.5 and 1Ag powders; (B) nitrite ions concentration profiles during irradiation for different photocatalysts.

On the contrary, the presence of Pd or Au NPs on TiO_2 unexpectedly suppressed the nitrite into nitrate photo-conversion (Fig. 10(B)), although nitrate anions were produced in detectable amounts during ammonia photo-oxidation experiments with both Pd and Au-loaded powders (Fig. 9(B) and (C)). One may thus conclude that ammonia photo-conversion into nitrate ions occurs in a single, complete oxidation step at the photocatalyst surface, without the formation of any intermediate, when Pd or Au/TiO_2 are employed as photocatalysts. This interpretation is also consistent with concentration *vs.* time profiles measured for 1Au (Fig. 9(C)), evidencing that nitrite and nitrate anions only form through parallel pathways during ammonia photocatalytic oxidation on Au-loaded powders.

6.6 Conclusion & Further Work

Generally, the photocatalytic oxidation of ammonia in TiO_2 aqueous suspension takes place through both parallel and consecutive reaction steps (see Scheme 1), leading to formation of different products.
N_2 formation might take place at the semiconductor surface through a pathway parallel to the main oxidation route, *via* a series of chain reactions directly involving ammonia in its activated form, *i.e.*, $(NH_2)_{ox}$. Species which have been supposed to form upon direct or indirect interaction of ammonia with *VB* holes at the photocatalyst surface comprise $H_2N{=}NH_2$ (hydrazine) and/or NH_2OH (hydroxylamine) [11,21,22,24-26,28,29,32]. Thus, it would be interesting to determine the extent of production of hydrazine and hydroxylamine since a better understanding of these reaction pathways may allow tuning the physico-chemical properties of the photocatalyst to selectively drive the process toward NH_3-into-N_2 conversion.

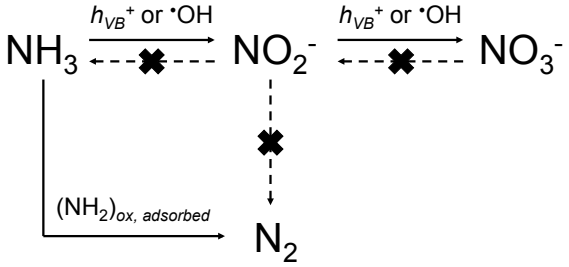

Scheme 1 – Pathways for the photocatalytic oxidation of ammonia.

Concerning ammonia photo-oxidation on metal-loaded TiO_2 photocatalysts, metal deposits enhance the separation of photo-generated charge carriers, by capturing *CB* electrons, thus making *VB* holes more available for reacting with NH_3 to form $(NH_2)_{ox}$ (this most likely does not occur with Au/TiO_2), as well as for producing nitrite and nitrate ions. Once formed, $(NH_2)_{ox}$ species may undergo several redox reactions with other nitrogen-containing species, finally yielding N_2.
Yet, also metal-induced adsorption effects should be taken into account. For instance, Pt NPs have a relatively strong adsorption affinity for ammonia and this specific feature is believed to affect NH_3 diffusion at the photocatalyst surface [31]. Thus, the selective formation of N_2 observed for Pt-modified TiO_2 can be explained in terms of specific adsorption of its precursors (*i.e.*, NH_3 and NH_x) on Pt deposits [14]. In this view, the ability of Pd NPs to adsorb derivatives of ammonia and to drive their oxidation toward the formation of N_2 should be investigated, since Pd-loaded powders exhibited

the highest S_{N2} values (even higher than that for unmodified P25). On the contrary, the poor adsorption of ammonia on Au NPs might be invoked to rationalize the unusual effects observed upon deposition of Au NPs on titania powders, which mainly consisted of a full suppression of N_2 formation.

In general, the results discussed through this chapter in terms of ammonia conversion, product selectivity and concentration profiles suggest that the presence of NPs of different metals at the TiO_2 surface, as well as the metal loading itself, drive the photocatalytic oxidation of ammonia through different paths, some of them occurring at the semiconductor surface (*e.g.*, direct oxidation mediated by *VB* holes) and some others taking place through indirect oxidation paths, *i.e.*, mediated by photo-produced $^{\bullet}OH$, $O_2^{\bullet-}$ and/or H_2O_2. The intermediates produced at the photocatalyst surface, containing nitrogen in different oxidation states, can combine or disproportionate, the former process most likely generating N_2. Indeed, metal NPs not only simply act as electron-traps, thus making the *VB* holes more prone to react with ammonia, but may also affect the mechanism of ammonia oxidation by interacting with (and/or stabilizing) photo-activated species and intermediates.

6.7 References & Notes

[1] M. Altomare, G.L. Chiarello, A. Costa, M. Guarino, E. Selli, Chem. Eng. J. 191 (2012) 394.

[2] "Photocatalytic treatment system and plant for reducing the nitrogen content in livestock waste" G.L. Chiarello, A. Costa, M. Guarino, E. Selli; PCT Int. Appl. (2010) WO 2010/086891.

[3] M. Altomare, E. Selli, Catal. Today 209 (2013) 127.

[4] J. Webb, H. Menzi, B.F. Pain, T.H. Misselbrook, U. Dämmgen, H. Hendriks, H. Döhler, Environ. Pollut. 135 (2005) 399.

[5] Northern Italy represents the area where more than the 60 % of the country's livestock resources is concentrated.

[6] C.E. Adams Jr., Environ. Sci. Technol. 7 (1973) 696.

[7] R.W. Melse, N.W.M. Ogink, W.H. Rulkens, Open Agric. J. 3 (2009) 6.

[8] Y.H. Ahn, Process Biochem. 41 (2006) 1709.

[9] M.R. Hoffmann, S.T. Martin, W. Choi, D.W. Bahnemann, Chem. Rev. 95 (1995) 69.

[10] H. Mozzanega, J.M. Herrmann, P. Pichat, J. Phys. Chem. 83 (1979) 2251.

[11] S. Yamazoe, T. Okumura, T. Tanaka, Catal. Today 120 (2007) 220.
[12] P.A. Kolinko, D.V. Kozlov, Appl. Catal. B: Environ. 90 (2009) 126.
[13] A. Bravo, J. Garcia, X. Domènech, J. Peral, J. Chem. Res. (Suppl.) (1993) 376.
[14] J. Lee, H. Park, W. Choi, Environ. Sci. Technol. 36 (2002) 5462.
[15] X. Zhu, S.R. Castleberry, M.A. Nanny, E.C. Butler, Environ. Sci. Technol. 39 (2005) 3784.
[16] S.M. Murgia, A. Poletti, R. Selvaggi, Ann. Chim. (Rome) 95 (2005) 335.
[17] I. Mikami, S. Aoki, Y. Miura, Chem. Lett. 39 (2010) 704.
[18] H. Kominami, H. Gekko, K. Hashimoto, Phys. Chem. Chem. Phys. 12 (2010) 15423.
[19] J.G. Chang, S.P. Ju, C.S. Chang, H.T. Chen, J. Phys. Chem. C 113 (2009) 6663.
[20] Q. Geng, Q. Guo, C. Cao, Y. Zhang, L. Wang, Ind. Eng. Chem. Res. 47 (2008) 4363.
[21] S. Yamazoe, T. Okumura, K. Teramura, T. Tanaka, Catal. Today 111 (2006) 266.
[22] S. Yamazoe, T. Okumura, H. Hitomi, T. Shishido, T. Tanaka, J. Phys. Chem. C 111 (2007) 11077.
[23] K. Teramura, T. Tanaka, S. Yamazoe, K. Arakaki, T. Funabiki, Appl. Catal. B Environ. 53 (2004) 29.
[24] M. Kaneko, G. Gokan, N. Katakura, Y. Takei, M. Hoshino, Chem. Commun. (2005) 1625.
[25] H. Yuzawa, T. Mori, H. Itoh, H. Yoshida, J. Phys. Chem. C 116 (2012) 4126.
[26] J. Nemoto, N. Gokan, H. Ueno, M. Kaneko, J. Photochem. Photobiol. A Chem. 185 (2007) 295.
[27] H. Kominami, H. Nishimune, Y. Ohta, Y. Arakawa, T. Inaba, Appl. Catal. B Environ. 111-112 (2012) 297.
[28] T. Shishido, K. Teramura, T. Tanaka, Catal. Sci. Technol. 1 (2011) 541.
[29] K. Teramura, T. Tanaka, T. Funabiki, Langmuir 19 (2003) 1209.
[30] J. Taguchi, T. Okuhara, Appl. Catal. A General 194-195 (2000) 89.
[31] H.H. Ou, M.R. Hoffmann, C.H. Liao, J.H. Hong, S.L. Lo, Appl. Catal. B Environ. 99 (2010) 74.
[32] M. Kaneko, H. Ueno, R. Saito, J. Nemoto, Catal. Lett. 137 (2010) 156.
[33] T. Tanaka, K. Teramura, K. Arakaki, T. Funabiki, Chem. Commun. (2002) 2742.
[34] G.L. Chiarello, M.H. Aguirre, E. Selli, J. Catal. 273 (2010) 182.
[35] G.L. Chiarello, L. Forni, E. Selli, Catalysis Today 144 (2009) 69.
[36] C. Bernardini, G. Cappelletti, M.V. Dozzi, E. Selli, J. Photochem. Photobiol. A Chem. 211 (2010) 185.

[37] G.L. Chiarello, A. Di Paola, L. Palmisano, E. Selli, Photochem. Photobiol. Sci. 10 (2011) 355.
[38] E.M. Bonsen, S. Schroeter, H. Jacobs, J.A.C. Broekaert, Chemosphere 35 (1997) 1431.
[39] D.W. Bahnemann, M. Hilgendorff, R. Memming, J. Phys. Chem. B 101 (1997) 4265.
[40] X. Zhu, M.A. Nanny, E.C. Butler, J. Photochem. Photobiol. A Chem. 185 (2007) 289.
[41] D.C. Hurum, K.A. Gray, T. Rajh, M.C. Thurnauer, J. Phys. Chem. B 109 (2005) 977.
[42] A. Zafra, G. Garcia, A. Milis, X. Domènech, J. Mol. Catal. 70 (1991) 343.
[43] A. Milis, X. Domènech, J. Photochem. Photobiol. A Chem. 72 (1993) 55.
[44] M.V. Dozzi, L. Prati, P. Canton, E. Selli, Phys. Chem. Chem. Phys. 11 (2009) 7171.
[45] M.V. Dozzi, A. Saccomanni, M. Altomare, E. Selli, Photochem. Photobiol. Sci. 12 (2013) 595.
[46] A. Naldoni, M. D'Arienzo, M. Altomare, M. Marelli, R. Scotti, F. Morazzoni, E. Selli, V. Dal Santo, Appl. Catal. B Environ. 130–131 (2013) 239.
[47] H.H. Ou, C.H. Liao, Y.H. Liou, J.H. Hong, S.L. Lo, Environ. Sci. Technol. 42 (2008) 4507.
[48] S. Chen, G. Cao, Desalination 194 (2006) 127.

7. Photocatalytic Water Splitting on TiO_2 Nanotubes

7.1 Overview

The photocatalytic splitting of water represents one of the most interesting processes in the current energy scenario since it provides an environmentally friendly fuel, *i.e.*, H_2, the combustion of which leads only to formation of water, and requires inexpensive and easily available resources, mainly comprising water, titania and solar light.
The photo-driven water splitting reaction was studied in this work on TiO_2 nanotubes arrays grown by electrochemical anodization on titanium substrates, the backsides of which, *i.e.*, the non-anodized surfaces, were covered by a sputtered thin layer of platinum. Such photo-electrodes were employed in a two-compartment photocatalytic cell allowing separate H_2 and O_2 production through water splitting.
The study aimed firstly at investigating the feasibility of scaling up the growth of nanotubes over a relatively wide surface. The effects of anodization time and thermal annealing on the structural properties and crystallographic features of the nanotubes, respectively, were investigated. Afterwards, the photocatalytic properties of the nanotube arrays were studied by measuring incident photon to current conversion efficiency (IPCE) spectra, photocurrent transients and by evaluating the amount of H_2 and O_2 evolved through water splitting in the two-compartment photocatalytic cell. The data and results presented in this chapter have been published in ref. [1].

7.2 Aim

Up to date, TiO_2-based materials are the most widely employed materials in photocatalysis [2], due to their relatively high efficiency, low cost, nontoxicity and, most importantly, (photo)chemical stability. However, conventional powder photocatalysts are not suitable for large-scale applications, not only because they exhibit fast charge carriers recombination [3], limiting photoactivity, and need to be recovered from the aqueous media after use, but mainly because they lead to production of H_2-O_2 mixtures, which must undergo subsequent separation and purification

treatments to attain high-purity hydrogen required in most of the applications [4].
Thus, there is an urgent need to develop and optimize devices, which exploit supported thin layer photocatalysts, to generate H_2 and O_2 streams (possibly separated from each other) through water photosplitting [3–11]. One-dimensional (*1D*) TiO_2 nanostructures, such as nanotubes (NT) arrays, meet these requirements, since they can be directly grown on support materials and also provide percolation pathways for photopromoted electrons [12,13], ensuring a more effective charge separation [14,15]. Furthermore, NT arrays, possessing high aspect ratio and surface area, guarantee enhanced photon absorption together with an extensive adsorption of reactants at the photocatalyst surface [16], with overall beneficial effects on photoactivity.
Among the different routes to prepare thin film semiconductor oxides, electrochemical anodization is surely one of the simplest and most versatile techniques to synthesize self-organized TiO_2 nano-architectures. In fact, the NT properties and morphology can be tailored by controlling experimental parameters such as anodization time, applied voltage, composition of the electrolyte and conditions of the thermal treatment [17].
In this study, a series of TiO_2 NT arrays grown by electrochemical anodization on large surface titanium substrate (*ca.* 10 cm^2) has been tested as photo-electrodes to separately produce H_2 and O_2 pure streams through photocatalytic water splitting in a two-compartments photocatalytic cell (described in ref. [8]), without any electrical bias and in the absence of sacrificial agents (*e.g.*, hole scavengers). The photocatalytic behavior of NT arrays has been discussed in relation to their photocurrent response, morphology and crystallographic features attained after different anodization times.

7.3 TiO_2 Nanotubes Characterization

7.3.1 Morphology

Typical top-view micrographs of the samples are shown in Fig. 1(A)–(F), where the effect of different anodization times on the morphology of the tubes can be appreciated. When performing SEM analysis, the morphological homogeneity of the anodic layers was always verified, before collecting representative images at different magnification.
Generally, it was observed that the thickness of the NT increased with anodization time, reaching values of several micrometers for long

experiments [15]. The as-received Ti disk exhibited a flat surface (Fig. 1(A)). After 20 min anodization (sample NT1, Fig. 1(B)) only small pores appeared within the TiO_2 surface. This is in line with the mechanism of NT growth, resulting from both formation of anodic oxide (passivation of titanium) and its controlled chemical dissolution (TiO_2 etching) [15].

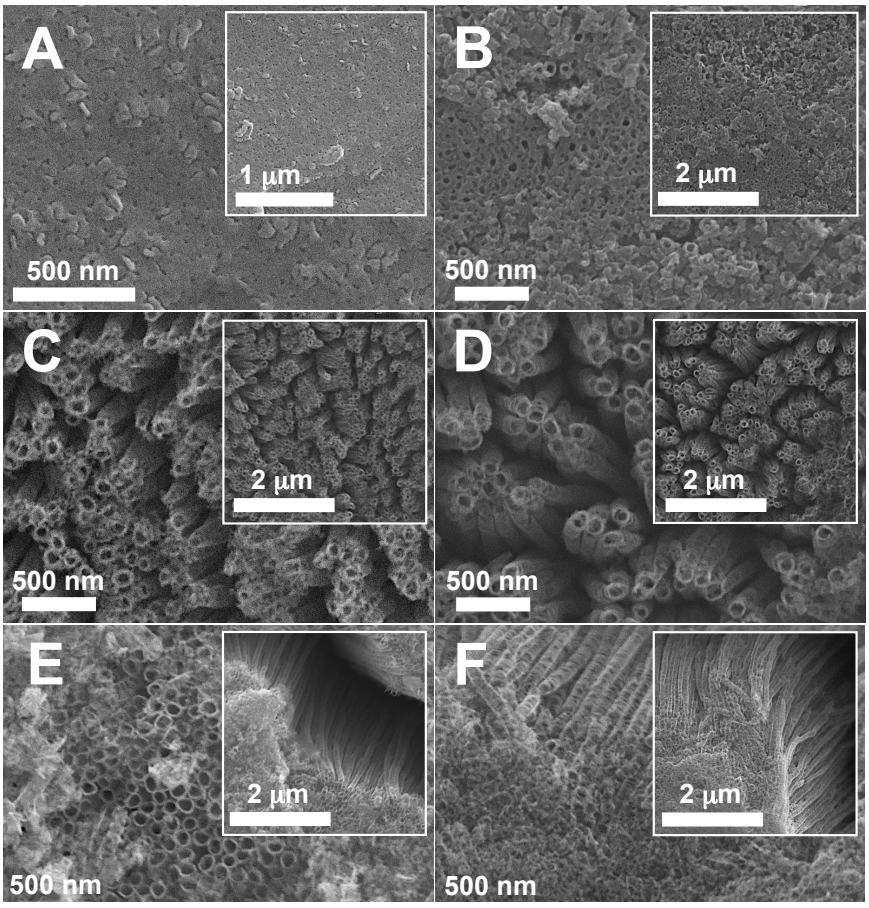

Figure 1 – SEM micrographs showing (A) the surface of a Ti disk prior to anodization and the NT arrays obtained after (B) 20 min, (C) 40 min, (D) 1 h, (E) 2.5 h and (F) 7 h-long anodizations. Insets: top views of the samples taken at lower magnification.

The 40 and 60 min-long anodization experiments (samples NT2 and NT3, see Fig. 1(C) and (D)) led to ordered nanotubular structures, grown homogeneously on the titanium substrate. For these samples, the layers of NT were a few micrometers thick. Longer anodization times (2.5 and 7 h, see Fig. 1(E) and (F)) led to the formation of NT bundles, with each bundle separated by deep cracks from the others. This morphology, characterized by NT clumped together at the top, results from the mechanical stress occurring during the slow formation of the anodic oxide layer, typically observed for anodization performed in organic electrolytes [16,18]. Fig. 1(C) and (d) show that tubes open at the top were obtained after 40 and 60 min-

long experiments. This morphology with high aspect ratio provided large surface area, suitable for efficient light absorption and photocatalytic performance. On the contrary, NT arrays obtained after 2.5 and 7 h (Fig. 1(E) and (F)) exhibited a non-homogeneous structure at the top, partially or almost totally covered by a thin, rough TiO_2 layer. During these experiments, steady state conditions (*i.e.*, constant current density) were on going, so that the thickening of the anodic layers occurred along with the thinning of the NT walls, especially at their top, where the NT underwent extensive etching being in contact for long time with the fluoride species contained within the electrolyte [15]. Thus, the structure possibly collapsed at the top as the NT walls became too thin to withstand their own weight, leading to the formation of an oxide layer that clogged the mouth of the tubes [19].

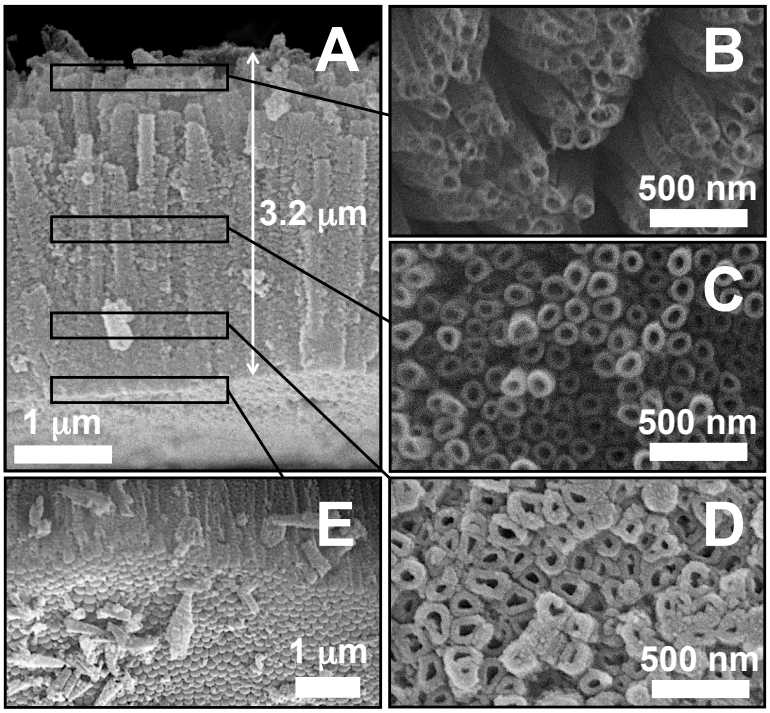

Figure 2 – SEM micrographs of the sample NT3 (60 min-long anodization) showing (A) the cross-section, the morphology (B) at the top, (C) at the middle, (D) near the bottom of the NT arrays and (E) their structure at the metal-metal oxide interface.

However, in spite of these remarkable differences in morphology, the tubes diameter (when visible and not clogged) was always around 120–130 nm for all NT arrays, regardless of the anodization time. This result is in agreement with previous works reporting that the diameter of the tubes is mainly related to the voltage applied during anodization [15,20].

Fig. 2(A) shows the cross-section of sample NT3, evidencing the typical columnar structure, with a layer thickness of *ca.* 3.2 μm. Fig. 2(B)–(D) show

SEM images taken at different heights along the NT layer. In particular, Fig. 2(B) shows that the tubes were clumped together at the top, while they were homogeneously packed and without cracks both at middle height and close to their bottom, as shown in Fig. 2(C) and (D), respectively. Moreover, the walls of the tubes become thicker toward the bottom of the anodic layer. This gradient of thickness is in agreement with the typical morphology observed for TiO_2 NT grown in organic electrolytes [15]. The underneath structure (*i.e.*, at the interface between titanium substrate and NT) is shown in Fig. 2(E) and evidences that NT were sealed by a hemispherical bottom.

7.3.2 Crystallographic Properties

As-formed TiO_2 NT arrays are typically amorphous and can be converted into anatase phase by annealing in air at temperatures higher than 280 ˚C. Anatase and rutile mixtures can be obtained at temperatures higher than 450 ˚C [22–25]. In this work, all anodic NT were annealed at 450 ˚C (air, 3 h).

Anodization time	Sample	Anatase phase			Rutile phase		
		a (Å)	*c* (Å)	wt%	*a* (Å)	*c* (Å)	wt%
20 min	NT1	3.7819	9.482	61.6	4.5888	2.9580	38.4
40 min	NT2	3.7811	9.4910	77.3	4.5890	2.9589	22.7
60 min	NT3	3.7831	9.4967	76.8	4.5913	2.9597	23.2
2.5 h	NT4	3.7824	9.4998	97.1	4.5919	2.958	2.9
7 h	NT5	3.7804	9.4927	99.3	4.592	2.955	0.7

Table 1 – Refined structural data obtained from XRD analysis of TiO_2 NT arrays produced by different anodization times.

In order to investigate the effect of the anodization time on the composition of the tubes upon annealing, XRD analysis was performed for the Ti disk and for the different NT arrays. The XRD patterns are collected in Fig. 3(A). The diffraction peaks of the pristine Ti disk correspond to metallic Ti. With increasing the anodization time, the intensity of Ti signals decreased, while the diffraction peaks of the anatase (*A*) and rutile (*R*) TiO_2 phases appeared, with the intensity of the former increasing with the anodization time. This is consistent with the thickness of TiO_2 NT layers that increases with the anodization time. The phase composition of the anodic oxides was determined by Rietveld analysis, by refining the diffraction data against the anatase, rutile and titanium structural models.

As an example, the Rietveld refinement of sample NT2 is shown in Fig. 3(B). Refined lattice parameters and weight fractions of all NT samples are reported in Table 1

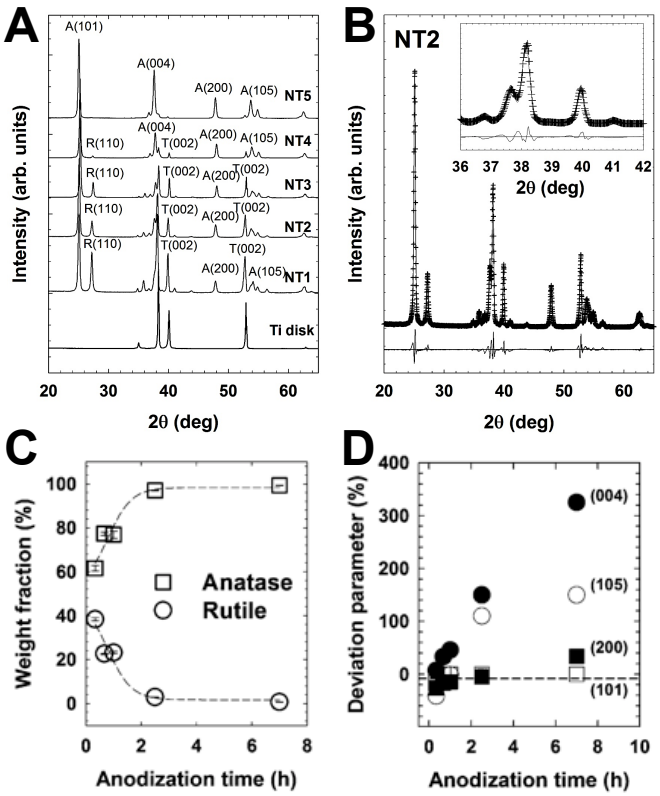

Figure 3 – (A) XRD patterns of Ti disk and of NT arrays, where the strongest reflections due to Ti (T), anatase (*A*) and rutile (*R*) TiO_2 phases are marked in each pattern; (B) measured (crosses) and calculated (continuous lines) diffraction patterns of sample NT2. The difference between the observed and the fitted patterns is displayed at the bottom of the panel. The inset of panel (B) shows a magnified view of the diffraction peaks at middle angles; (C) refined weight percent fractions of the anatase and rutile phases in all TiO_2 NT arrays; (D) corresponding deviation parameter *D*(hkl) of the anatase (004), (105), (200) and (101) reflections, plotted as a function of the anodization time. The dashed line in panel (D) marks the zero deviation for a random anatase powder.

A plot of refined weight fractions of anatase and rutile phases as a function of the anodization time is shown in Fig. 3(C). After a 20 min-long anodization, a 60:40 anatase-rutile mixed phase was obtained, while longer experiments led to an increase of the anatase content. In particular, the rutile phase almost disappeared (~ 3 wt%) in sample NT4 that was obtained by a 2.5 h-long anodization, whereas after 7 h (sample NT5) a nearly pure anatase layer was obtained. The fact that the phase composition of the

anodic oxides was dependent on the anodization time can be ascribed to the initial nucleation of a thin rutile layer (50–100 nm) at the Ti–TiO_2 interface [19], followed by formation of near pure anatase. In other words, rutile content was reasonably almost the same in all samples, whereas the amount of anatase phase increased with increasing the thickness of the NT layer, so that the percent amount of rutile became negligible in samples anodized for long time, *i.e.*, for relatively thick layers.

The average crystallite size of the TiO_2 NT, determined by applying the single peak method (*i.e.*, the Scherrer equation) to the (101) and (110) reflections of *A* and *R* phases, respectively, were almost identical for both phases and for all samples, increasing from 25 to 34 nm from samples NT1 to NT4, while a slightly lower value (~ 29 nm) was obtained for *A* phase in sample NT5.

The intensity of some reflections of the *A* phase increased with the anodization time more rapidly than others (Fig. 3(A)), this feature being ascribed to effects implying crystallographic preferential orientation, related to the anisotropic character of the TiO_2 microstructure. This effect was analyzed in terms of normalized intensities, which were determined by dividing the intensity of the peaks by the maximum intensity of the (101) reflection. The effect related to preferential orientations was thus quantified in terms of a percent deviation parameter (*D*), calculated as the percent difference between the normalized reflection intensities of the anodic oxides and those of a fully random orientation, according to Eq. 1:

$$D(hkl)(\%) = \frac{I(hkl)_S - I(hkl)_P}{I(hkl)_P} \times 100 \qquad (1)$$

where $I(hkl)_S$ is the normalized intensity related to the *(hkl)* peak of the sample and $I(hkl)_P$ is the normalized intensity of the *(hkl)* peak for the TiO_2 reference powder [21].

The *D(hkl)* values relative to the main anatase reflections are plotted as a function of the anodization time in Fig. 3(D). The intensity of the (200) reflection was in close agreement with that of isotropic anatase TiO_2, whereas the intensity of (105) and (004) reflections showed positive deviation from the randomly oriented powder, with the extent of the deviation increasing with increasing the anodization time. In particular, the *D*(004) parameter for sample NT5 (7 h) reached a value 3 times higher (D > 300 %) than that of a random orientation.

It's worth underlining that XRD data were collected in reflection mode, *i.e.*, by placing the anodic layers parallel to the sample holder. Thus, crystallographic planes parallel to the film surface mainly contributed to the diffracted intensities. According to SEM analysis and XRD data refinements,

a preferentially oriented anatase TiO_2 layer was formed at the top of the tubes after long anodization times (> 1 h), as well evidenced in Fig. 3(D) by the evolution of the *D*(004) parameter with the anodization time.
The formation of a preferentially oriented anodic oxide has been recently reported also by Lee *et al.* [27], who grew TiO_2 NT with specific crystallographic orientations by controlling the water content of the electrolyte used for the anodization experiments. However, the preferential crystallographic orientation observed in this study is most likely related to the anatase layer formed at the top of the NT (after long anodization time, Fig. 1(E) and (F)) rather than to the NT themselves.

7.4 Photocatalytic Production of H_2

The photocatalytic activity of TiO_2 nanotubes was evaluated by measuring the amount of H_2 and O_2 separately produced through water splitting in a photocatalytic cell herein briefly described in Section 3.6.4 (a full description of the device can be found in ref. [8]). All photocatalytic experiments were carried out without applying any electrical bias and in the absence of hole scavenger (*i.e.*, no organics were added to the electrolyte). Results are collected in Table 2.
Upon illumination of anodic NT layers, electron–hole pairs are generated. The photopromoted electrons migrate along the TiO_2 NT, *i.e.*, across the anodic film, and are transferred through the conductive titanium disk to the Pt film that is deposited on the opposite side of the photo-electrode (see sketch in Section 3.2.1). Meanwhile, photoproduced holes remain confined in the TiO_2 valence band. Photopromoted electrons reduce H^+, thus generating H_2 in the cathodic side of the cell, while the holes oxidize water to O_2 in the anodic compartment, as follows:

Generation of e^-–h^+ pair $\quad TiO_2 + h\nu \rightarrow e^- + h^+$

Cathodic reaction $\quad 2H^+ + 2e^- \rightarrow H_2$

Anodic reaction $\quad 2H_2O + 2h^+ \rightarrow O_2 + 4H^+$

The apparent quantum efficiency of H_2 production through photocatalytic water splitting (Φ_{H2}, see Table 2) was calculated according to Eq. 2:

$$\Phi_{H_2}\,(\%) = \frac{2 \times r_{H_2}}{I \times A} \times 100 \qquad (2)$$

where r_{H2} is the rate of H_2 production, I is the irradiation intensity on the TiO_2 NT arrays and A is the irradiated area (*ca.* 9.6 cm^2).
During irradiation, H_2 and O_2 evolved within the cathodic and anodic compartments, respectively, and accumulated within the burettes, which were outgassed through their upper stopcocks when required. Small traces of H_2 (always below 5 vol%) were detected in the O_2 stream, probably due to the *in situ* reaction of photopromoted electrons with water occurring also in the anodic side of the cell. On the other hand, H_2 was always found to evolve as pure gas within the cathodic side of the cell, *i.e.*, no traces of other gases were detected.

Sample	r_{H2} [a] (µmol h^{-1})	r_{O2} [a] (µmol h^{-1})	Productivity [b] (NL_{H2} m^{-2} h^{-1})	Φ_{H2} [b] (%)
NT1	38 ± 5	23 ± 2	0.87	6.9
NT2	80 ± 8	43 ± 4	1.9	15
NT3	43 ± 7	23 ± 5	1.0	7.9
NT4	23 ± 3	12 ± 2	0.53	4.2
NT5	29 ± 6	14 ± 4	0.67	5.4

Table 2 – Photocatalytic activity of TiO_2 NT arrays in terms of rates of H_2 and O_2 production (r_{H2} and r_{O2}), productivity of H_2 and apparent quantum efficiency Φ_{H2}. [a]Average values calculated over 3 consecutive photocatalytic runs. [b]Values based on the data collected during the third run.

In all photocatalytic tests, photo-assisted splitting of water into H_2 and O_2 occurred at almost constant rate and the H_2-O_2 ratio was always *ca.* 2, aside from an initial induction during the first 90 min of irradiation (see Fig. 4(A)). Moreover, the amount of overall H_2 evolved at the end of each experiment noticeably increased during consecutive runs with all NT arrays, as evidenced in Fig. 4(B), especially in the case of NT4. Considering all results, the photoactivity trend in water splitting was always NT2 >> NT3 > NT1 > NT5 > NT4, even after 18 h-long experiments. It's worth underlining that the r_{H2} and r_{O2} values reported in Table 2 are average values based on data collected over three consecutive photocatalytic runs, and this explains their relatively high uncertainty values.
Sample NT1 was characterized by a poor photocatalytic performance, probably because of its "immature" morphology, *i.e.*, it only exhibits scallop-shaped pores within the surface passivation layer and no nanotubular structure is formed yet (Fig. 1(B)). This low photoactivity might also be ascribed to its high rutile content (Fig. 3(C)). In fact, in view of photocatalytic

applications, TiO_2 anatase phase is usually preferred because it is characterized by higher electron mobility. Moreover, the anodic layer of sample NT1 is not expected to be thick enough to grant full light absorption. On the contrary, well-organized and top-open tubes, such as those obtained for samples NT2 and NT3 (Fig. 1(C) and (D)), exhibited higher water splitting ability. Their phase composition (*ca.* 80:20 anatase-rutile, quite similar to that of TiO_2 P25) might imply the formation of anatase-rutile heterojunctions, leading to improved charge transfer and photocatalytic properties, by enhancing the efficiency of e^-–h^+ separation [19].

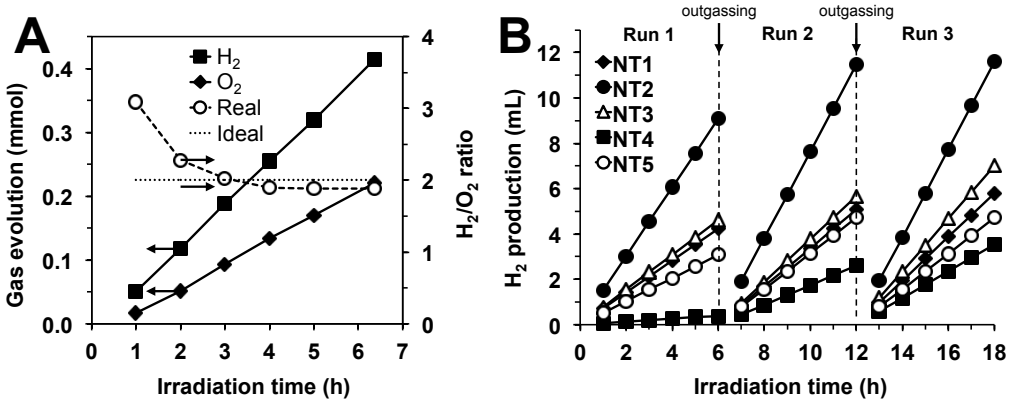

Figure 4 – (A) Photocatalytic production of H_2 and O_2 for sample NT2, along with the ideal (horizontal line) and measured (circles) H_2/O_2 ratio; (B) H_2 production during three consecutive 6 h–long runs with all NT arrays.

The photocatalytic activity of NT4 and NT5 was clearly lower compared to that of thinner films (Fig. 1(E) and (F)). Such a trend is most probably due to the detrimental formation of (004)-preferentially oriented anatase phase that covered (partially or even totally) the top of the tubes. This compact layer clogged the mouth of the tubes, thus reducing their surface area and consequently their photocatalytic activity. Moreover, although a thicker film may ensure full light absorption, it would exhibit an extended e^-–h^+ recombination at the same time, since *CB* electrons have to migrate over a long path through the NT before reaching the Pt-coated side of the photo-electrodes. The compact layer at the top of the tubes is also expected to decrease the conductivity of the film. In fact, it was recently reported that the (004)-preferentially oriented anatase phase is characterized by low density and mobility of photogenerated charge carriers [28,29].

Overall, the photocatalytic activity of the nanotubes reflects their morphology and phase composition, with NT2 showing the best performance in terms of H_2 production rate (*ca.* 83 mmol h^{-1} m^{-2}, corresponding to 1.9 NL h^{-1} m^{-2}, see Table 2). These results can be definitely attributed to the morphology of sample NT2 (open NT and proper thickness

of the film) along with its mixed anatase-rutile phase composition, granting full light absorption and limited e^-–h^+ recombination [10,20].

7.5 Photocurrent Measurements

Fig. 5(A) shows IPCE spectra recorded with all TiO_2 NT arrays. The curves were obtained according to the following equation (3), as reported in ref. [30]:

$$IPCE\ (\%) = \frac{1240 \times I_{SC}}{P_{light} \times \lambda} \times 100 \qquad (3)$$

where I_{SC} (A cm^{-2}) is the short circuit photocurrent density measured at a specific incident wavelength λ (nm) and P_{light} (W cm^{-2}) is the illumination power density at the same wavelength.

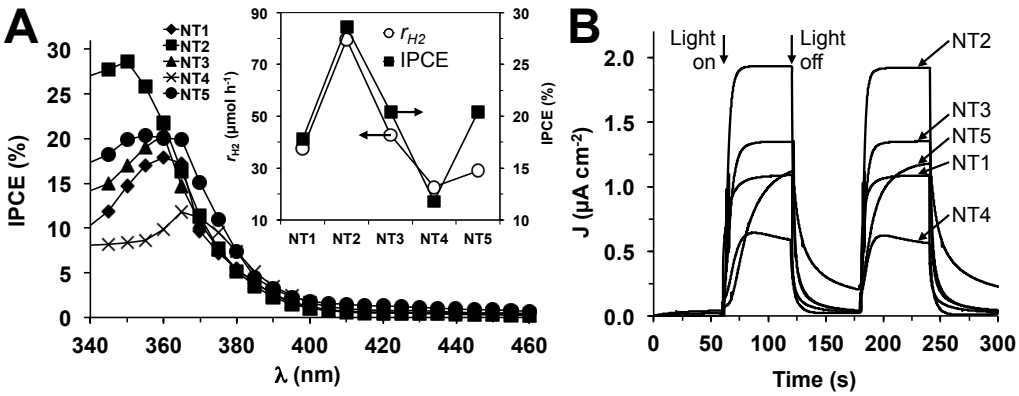

Figure 4 – (A) IPCE spectra, with the inset showing a comparison between the rate of H_2 production r_{H2} and the maximum IPCE value and (B) photocurrent transient signals recorded under chopped (60 s on–off) monochromatic irradiation, for all TiO_2 NT arrays obtained by different anodization times.

All NT layers showed an absorption edge (IPCE > 1 %) at *ca.* 400 nm, which is consistent with an energy band gap of around 3.1 eV, related to mixed anatase-rutile phase composition of the NT [18]. No difference of IPCE onset could be appreciated in relation to the different phase composition of the NT arrays. Moreover, IPCE spectra exhibited their maximum, all above 10 %, at different wavelengths, ranging from 350 nm for NT2 to 365 nm for NT4, this difference possibly owing to morphology and phase composition of the tubes. The anodic film grown by 40 min-long anodization, *i.e.*, sample NT2, was the most photoactive, exhibiting the highest IPCE value of ~ 28 %. The maximum IPCE trend followed the order NT2 > NT3 > NT5 > NT1 > NT4, with a significant variation of the IPCE maximum perfectly mirroring the

trend of photoactivity discussed in the previous section (see inset of Fig. 5(A)). Thus, the morphology and phase composition of nanotubes play a major role in determining their photocatalytic and photo-electrochemical behavior.

The shape of the photocurrent transient signals, recorded by 60 s-long light on–light off cycles, provided further information on the photoresponse dynamics, in relation to the structural features of the anodic films. As shown in Fig. 5(B), fast photocurrent rise and decay, resulting in square-shaped signals, were observed for samples NT1, NT2 and NT3, all consisting of well-aligned and top-open NT. For these arrays, the dark current was almost zero, while the response quickly reached a steady-state value upon illumination (1.0, 1.8 and 1.3 μA cm^{-2} for NT1, NT2 and NT3, respectively). Such a photoresponse indicates efficient charge separation and rapid electron migration toward the back contact [31].

On the contrary, a sort of capacitive behavior, consisting of an exponential raise and decay of the transient signal when light was turned on and off, was observed for samples NT4 and, in particular, NT5 (Fig. 5(B)). Although the two samples exhibited quite similar performance in photocatalytic water splitting (Table 2), sample NT4 showed a peculiar photoresponse curve (Fig. 5(A)) with the lowest IPCE, possibly due to the extended length of the NT and partial coverage at their top. On the other hand, NT5, fabricated after a longer anodization time compared to other films, essentially consisted of almost pure preferentially oriented anatase phase, able to fully absorb light and produce e^-–h^+ couples. This resulted in a relatively high IPCE signal (Fig. 5(B)). However, on the basis of time-resolved photoluminescence measurements, *CB* electrons generated within the (004) preferentially oriented anatase phase have low lifetime and mobility, as recently reported in the literature [28]. Thus, for sample NT5 that was anodized for excessively long time, photopromoted electrons were retarded in their migration along the TiO_2 layer because of extended trap-filling, predominantly occurring within the anatase layer grown at the top of the NT.

7.6 Conclusion & Further Work

Photo-active TiO_2 nanotubes/Ti/Pt electrodes were fabricated and employed for photocatalytic water splitting in a cell allowing the separate H_2 and O_2 production. Photo-anodes, *i.e.*, TiO_2 nanotubes, grown by conventional anodization approach, where short-circuited to the cathode, *i.e.*, thin sputtered layer of Pt, so that the photo-electrodes could be placed in the

frame separating the two compartments of the cell, where separate production of H_2 and O_2 occurred at the Pt-side and TiO_2 nanotubes-side, respectively, upon UV-light irradiation and in the absence of any electrical bias and holes scavenger. Aside from band gap excitation, only the chemical bias, *i.e.*, the ΔpH between the two compartments of the cell, assisted the photo-driven water splitting reaction.

The growth of TiO_2 nanotubes was studied to assess the feasibility of scale-up, *i.e.*, fabricating the tubes on relatively wide surfaces, rather than to investigate innovative electrolytes or experimental conditions. In fact, although the mechanism of growth and experimental conditions to fabricate TiO_2 nanotubes are well known, scaling-up of self-organizing anodization still represents a field to explore more in depth.

In this study, we observed that anodization conditions strongly affect the physico-chemical properties (*e.g.*, morphology and phase composition), as well as the photocatalytic and photo-electrochemical behavior of the tubes. Therefore, in view of possible large-scale applications, it is worth to tune the experimental conditions in order to grow ordered nanotube arrays, with a morphology (*e.g.*, features of the tubes, thickness of the film) ensuring the best photocatalytic and photo-electrochemical performance. Nevertheless, photocatalytic H_2 and O_2 production might be investigated also upon Vis-light irradiation, possibly by modifying the light absorption properties of the tubes through doping and/or deposition/incorporation/adsorption of Vis-light harvesting materials.

7.7 References & Notes

[1] M. Altomare, M. Pozzi, M. Allieta, L.G. Bettini, E. Selli, Appl. Catal. B Environ. 136-137 (2013) 81.

[2] X. Chen, S.S. Mao, Chem. Rev. 107 (2007) 2891.

[3] K. Fujihara, T. Ohno, M. Matsumura, J. Chem. Soc. Faraday Trans. 94 (1998) 3705.

[4] M. Kitano, M. Takeuchi, M. Matsuoka, J.M. Thomas, M. Anpo, Catal. Today 120 (2007) 133.

[5] M. Kitano, R. Mitsui, D.R. Eddy, Z.M.A. El-Bahy, M. Matsuoka, M. Ueshima, M. Anpo, Catal. Lett. 119 (2007) 217.

[6] M. Kitano, M. Matsuoka, M. Ueshima, M. Anpo, Appl. Catal. A General 325 (2007) 1.

[7] M. Matsuoka, M. Kitano, M. Takeuchi, K. Tsujimaru, M. Anpo, J.M. Thomas, Catal. Today 122 (2007) 51.

[8] E. Selli, G.L. Chiarello, E. Quartarone, P. Mustarelli, I. Rossetti, L. Forni, Chem. Commun. (2007) 5022.
[9] Y. Sun, G. Wang, K. Yan, Int. J. Hydrogen Energy 36 (2011) 15502.
[10] Y. Sun, K. Yan, G. Wang, W. Guo, T. Ma, J. Phys. Chem. C 115 (2011) 12844.
[11] R. Marschall, C. Klaysom, A. Mukherji, M. Wark, G.Q.M. Lu, L. Wang, Int. J. Hydrogen Energy 37 (2012) 4012.
[12] M. Law, J. Goldberger, P. Yang, Annu. Rev. Mater. Res. 34 (2004) 83.
[13] M. Grätzel, Inorg. Chem. 44 (2005) 6841.
[14] R. Jennings, A. Ghicov, L.M. Peter, P. Schmuki, A.B. Walker, J. Am. Chem. Soc. 130 (2008) 13364.
[15] P. Roy, S. Berger, P. Schmuki, Angew. Chem. Int. Ed. 50 (2011) 2904.
[16] G.K. Mor, O.K. Varghese, M. Paulose, K. Shankar, C.A. Grimes, Sol. Energy Mater. Sol. Cells 90 (2006) 2011.
[17] S. Rani, S.C. Roy, M. Paulose, O.K. Varghese, G.K. Mor, S. Kim, S. Yoriya, T.J. La Tempa, C.A. Grimes, Phys. Chem. Chem. Phys. 12 (2010) 2780.
[18] Y. Liu, R.S. Alwitt, K. Shimizu, J. Electrochem. Soc. 147 (2000) 1382.
[19] I. Paramasivam, H. Jha, N. Liu, P. Schmuki, Small 8 (2012) 3073.
[20] J.M. Macak, H. Tsuchiya, A. Ghicov, K. Yasuda, R. Hahn, S. Bauer, P. Schmuki, Curr. Opin. Solid State Mater. Sci. 11 (2007) 3.
[21] J.K. Burdett, T. Hughbanks, G.J. Miller, J.W. Richardson Jr., J.V. Smith, J. Am. Chem. Soc. 109 (1987) 3639.
[22] J. Yu, B. Wang, Appl. Catal. B Environ. 94 (2010) 295.
[23] O.K. Varghese, D. Gong, M. Paulose, C.A. Grimes, E.C. Dickey, J. Mater. Res. 18 (2003) 156.
[24] A. Ghicov, H. Tsuchiya, J.M. Macak, P. Schmuki, Phys. Status Solidi A 203 (2006) R28.
[25] J.M. Macak, S. Aldabergerova, A. Ghicov, P. Schmuki, Phys. Status Solidi A203 (2006) R67.
[26] J. Zhao, X. Wang, T. Sun, L. Li, Nanotechnology 16 (2005) 2450.
[27] S. Lee, I.J. Park, D.H. Kim, W.M. Seong, D.W. Kim, G.S. Han, J.Y. Kim, H.S. Jung, K.S. Hong, Energy Environ. Sci. 5 (2012) 7989.
[28] H.T. Tung, J.M. Song, S.W. Feng, C. Kuo, I.G. Chen, Phys. Chem. Chem. Phys. 12 (2010) 740.
[29] Y. Xu, M.R. Shen, Appl. Phys. A 94 (2009) 275.
[30] O. Enea, J. Moser, M. Grätzel, J. Electroanal. Chem. 259 (1989) 59.
[31] A. Mazzarolo, K. Lee, A. Vicenzo, P. Schmuki, Electrochem. Commun. 22 (2012) 162.

8. Ta-Doped TiO_2 Nanotubes

8.1 Overview

The fabrication of Ta-doped TiO_2 nanotubes and their application for H_2 production through photo-electrochemical splitting of water are herein described. Ta-doped TiO_2 nanotubes were fabricated by electrochemical anodization of Ti-Ta alloys. The anodic oxides were converted into crystalline materials by thermal treatment and the crystallographic phase composition of the nanotubes was studied in relation to the different annealing temperatures. Moreover, the effects of Ta content, phase composition and thickness of the anodic films on the photo-electrochemical properties of the nanotubes were investigated. Ta-doped nanotubes arrays exhibited enhanced water-splitting behavior compared to pure TiO_2 nanotubes. The data and results presented in this chapter have been published in ref. [1].

8.2 Aim

In view of improving the photocatalytic properties of TiO_2, pathway of nanostructuring [2,3] is one of the most often explored. One-dimensional (*1D*) architectures, *i.e.*, nanotubes, grant unidirectional percolation paths for photo-excited charge carriers and inhibit the e^-–h^+ recombination process [4-9], as discussed also in the previous chapter. Nevertheless, another promising way to improve the photo-electrochemical properties of a semiconductor is to introduce dopants such as Ru, Nb or Ta into its structure. Doping can improve either charge transfer or charge transport, and consequently reduce charge-carrier recombination [10-12].
Therefore, an elegant approach to combine the advantages of *1D* architectures with those given by doping would be the growth of self-organized nanotubes by anodization of Ti-based alloys. Recently, this was successfully demonstrated for anodic TiO_2 nanotubes (NT) doped with small amounts (< 0.1 at%) of Ru or Nb [2,13], for which strongly enhanced water-splitting behavior was observed. Promising results were also obtained for Ru-, Nb- and Ta-doped TiO_2 NT layers used for dye-sensitized solar cells (DSSC) [14-16]. The fabrication of self-organized Ta-doped TiO_2 nanotubes

and their application as photo-anodes are herein investigated. The layers were grown by electrochemical anodization of low-Ta-content (< 0.4 at%) Ti–based alloys and tested for H_2 production by photo-electrochemical (PEC) water splitting. The performance of NT arrays is discussed in relation to different parameters, namely, the content of Ta, the thickness of the anodic oxides, the annealing temperature and the crystallographic phase composition.

8.3 Characterization

Fig. 1 shows typical SEM micrographs of undoped and Ta-doped TiO_2 NT arrays. Fig. 1(A)–(D) show a comparison of the morphology of 7 μm thick layers. All NT had similar appearance, with an outer diameter of *ca.* 140-160 nm, regardless of both Ta content and layer thickness.

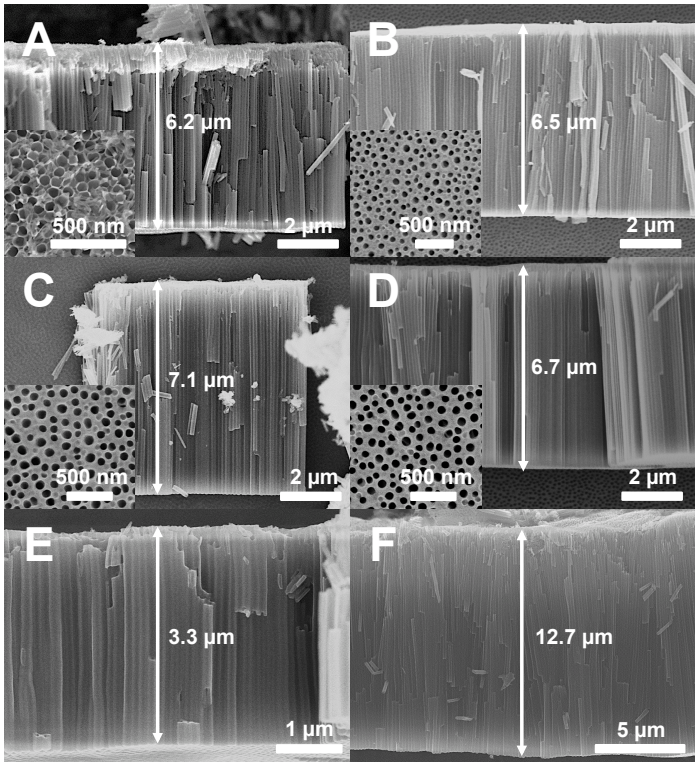

Figure 1 – SEM micrographs showing the cross sections of 7 μm (A) pure TiO_2 NT, (B) 0.03 at%, (C) 0.1 at% and (D) 0.4 at% Ta–TiO_2 NT. The insets show the top-view morphology of the layers. Micrographs (E) and (F) show 0.1 at% Ta–TiO_2 NT 3 and 12 μm thick, respectively.

The only minor difference was that Ta-doped films show slight remnants of an initiation layer at the top of the tubes (insets of Fig. 1(B)-(D)).

When as grown, the nanotubes structures were amorphous and their conversion into crystalline oxides was achieved by annealing in air at different temperatures (*i.e.*, 450, 550, 650 and 750 ˚C). Fig. 2(A) shows the XRD patterns for pure and Ta-doped TiO_2 NT arrays annealed at 650 ˚C (all 7 µm thick). Annealing at such high temperature led to NT conversion into both anatase and rutile phases. Moreover, one can notice that Ta doping slightly affected the anatase/rutile ratio, leading to an increase of the relative amount of rutile with increasing the Ta content.

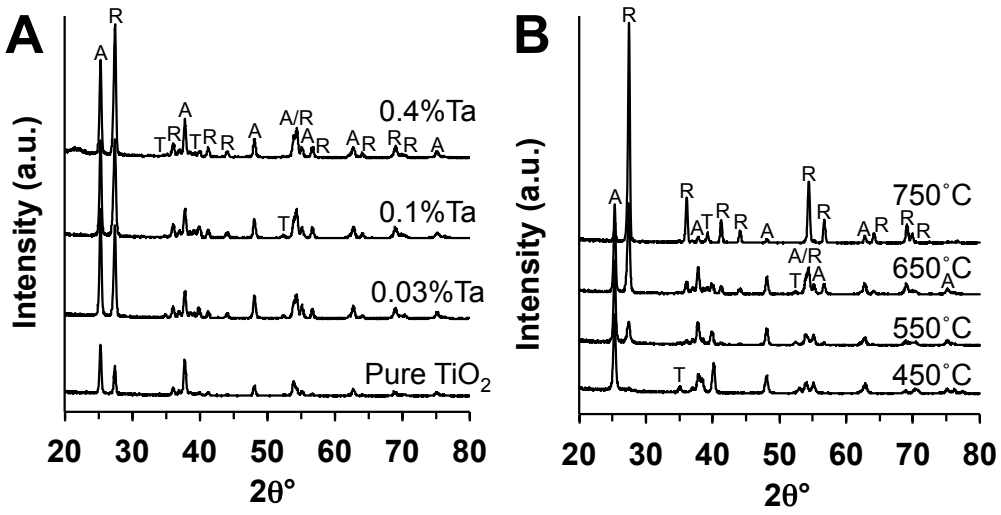

Figure 2 – XRD patterns for (A) 7 µm thick NT annealed at 650 ˚C with different Ta contents and (B) 7 µm thick 0.1 at% Ta–doped TiO_2 NT annealed at different temperatures (A = anatase, R = rutile and T = titanium).

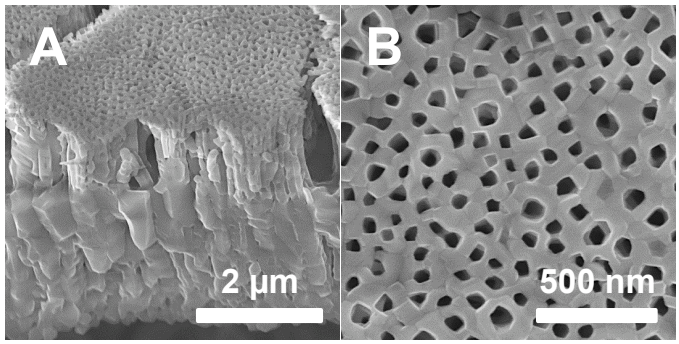

Figure 3 – SEM micrographs showing (A) cross-sectional and (B) top-view morphologies of 7 µm 0.1 at% Ta–doped TiO_2 NT annealed at 750 ˚C.

As illustrated in Fig. 2(B), the rutile phase was predominant compared to anatase when nanotubes underwent annealing at relatively high temperature (650 ˚C). This is ascribed to anatase-into-rutile phase transition occurring within the walls of the tubes and also to the nucleation of a compact rutile layer at the metal–metal oxide interface [17].

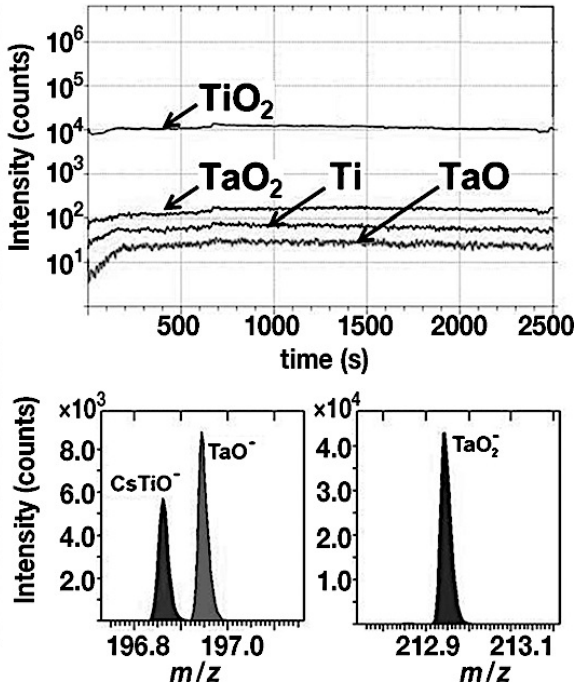

Figure 4 – TOF-SIMS analysis for 7 µm 0.1 at% Ta–doped TiO_2 NT annealed at 650 ˚C, showing the depth profile for Ti and Ta species (*m/z* of TaO_2, and TaO are 212.9 and 196.9, respectively). Spectra of the Ta-containing species are in the two lower panels.

The growth of such compact and thick rutile layers at 750 ˚C typically occurs along with the collapse of the nanotubular structure [2,17], as shown in Fig. 3. In contrast, annealing at 450 ˚C led to the formation of anatase nanotubes (with small amounts of rutile) with no loss of structural integrity.

For 7 µm thick layers grown on Ti–Ta alloys, neither peaks related to crystalline Ta oxide (*e.g.*, Ta_2O_5) nor shifts of TiO_2 reflections could be detected by XRD analysis, even after annealing at 750 ˚C. Interestingly, for Ti–Ta alloys, Ta oxide crystallization into β-Ta_2O_5 is reported to take place at approximately 700 ˚C [18]. Thus, the absence of Ta_2O_5 peaks can be attributed to the small amount of Ta in our samples or to its substitutional incorporation into the TiO_2 lattice.

However, the presence of Ta in the anodic films was confirmed by time of flight - secondary ion mass spectrometry (TOF-SIMS) analysis. As shown in the negative spectra in Fig. 4 (lower panels), two Ta-containing species,

characterized by *m/z* ratios of 196.91 (TaO^-) and 212.9 (TaO_2^-), were detected for 0.1 % Ta–doped TiO_2 NT annealed at 650 ˚C. Furthermore, the depth-profile analysis (Fig. 4) revealed an almost constant intensity of the Ta fragment peaks over a depth of approximately 1.5 µm, indicating a homogeneous distribution of the dopant within the nanotubes layer (the sputter rate, estimated by profilometry, was around 1 µm in 1600 s sputter time).

8.4 Photo-Electrochemical Water Splitting

The photo-electrochemical water splitting behavior under simulated sunlight conditions (AM 1.5 at 100 mW cm^{-2}) for 7 µm thick pure and Ta–doped TiO_2 NT is illustrated in Fig. 5(A). From the transient-photocurrent *vs.* potential curves of samples annealed at 650 ˚C, it is evident that the photocurrent density was dramatically enhanced even at low Ta concentrations (*i.e.*, 0.03 and 0.1 at%). On the other hand, the photoresponse dropped to a value comparable to that for pure TiO_2 for a Ta content of 0.4 at%. However, it is worth noting that Ta doping was not detrimental to photoresponse even under non-optimized conditions.

These results could be explained by the fact that photogenerated electrons must travel through the NT walls towards the back contact, in order to contribute to photocurrent. Thus, if Ta in the nanotubes is perceived as electronic doping, the high photocurrent density shown by TiO_2 NT arrays doped with low Ta concentrations (up to 0.1 at%) can be ascribed to improved electron conductivity [10]. In contrast, higher Ta contents (*e.g.*, 0.4 at%) led to a decrease of the photoresponse. If Ta is regarded as electronically active, this effect can be interpreted in terms of larger number of defects acting as recombination centers.

Fig. 5(B) shows the effects of annealing temperature on the photoresponse of 0.1 at% Ta–doped tubes. The highest photocurrent density was recorded with the sample annealed at 650 ˚C. Thus, our best results were achieved with Ta–TiO_2 NT arrays composed of a mixed anatase–rutile structure. Precisely, the photocurrent density was improved by increasing the annealing temperature from 450 to 650 ˚C, which also led to a significant increase of rutile content. Considering the trend of photoresponse, one may conclude that beneficial effects, in terms of charge transfer and electron conductivity, principally arose when small amounts of Ta were introduced into the rutile lattice. Moreover, as shown in Fig. 5(B) and (C), the photo-response was almost totally suppressed when Ta-doped nanotubes

underwent annealing at 750 ˚C. In this case, the collapse of the tubes, taking place at high temperature, is the most probable reason for the decreased photoresponse.

Fig. 5(C) shows the maximum photocurrent density (recorded at 430 mV) for pure and Ta–doped TiO_2 NT as a function of annealing temperature. Clearly, by increasing the annealing temperature from 450 to 650 ˚C, the photoresponse of 0.1 at% Ta–doped TiO_2 NT was nearly doubled, whereas it was dramatically decreased for all other layers. Indeed, for 7 µm tubes annealed at 650 ˚C, a Ta concentration around 0.1 at% was found to be optimal, whereas Ta doping did not provide a considerable benefit when NT arrays underwent low-temperature thermal treatment (*i.e.*, at 450 ˚C).

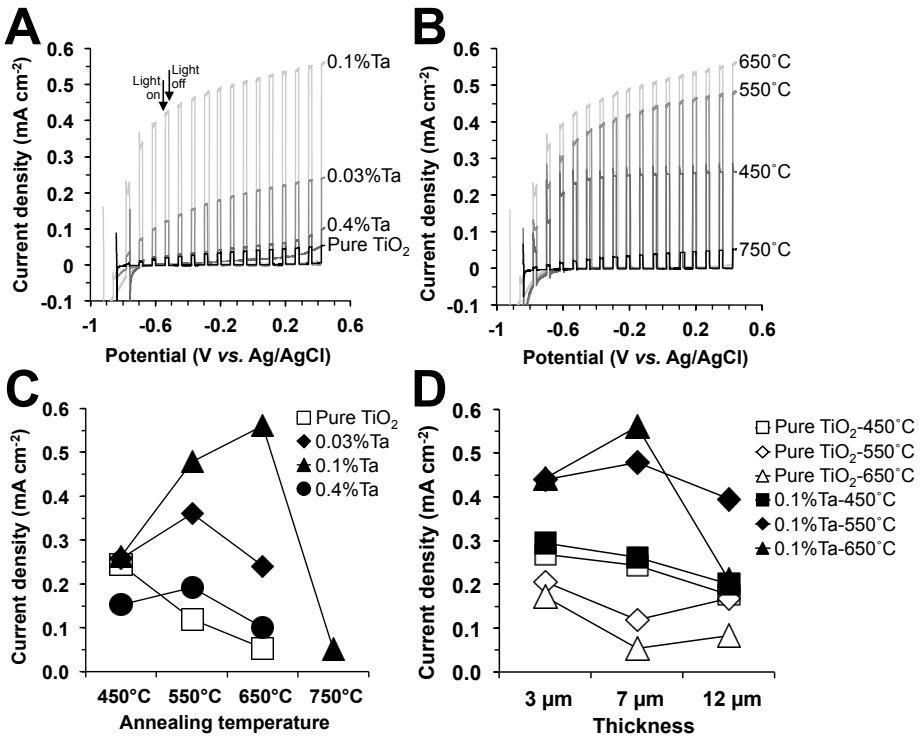

Figure 5 – Photo-electrochemical water splitting behavior of (A) 7 µm thick TiO_2 NT annealed at 650 ˚C with different Ta contents and (B) 7 µm thick 0.1 at% Ta–doped TiO_2 NT annealed at different temperatures; (C) maximum photocurrent density (recorded at 430 mV) for 7 µm TiO_2 NT with different Ta contents plotted against the annealing temperature; (D) maximum photocurrent density (recorded at 430 mV) for pure TiO_2 NT and 0.1 at% Ta–doped TiO_2 NT annealed at different temperatures, reported as a function of the thickness of the films.

For 7 µm thick 0.1 at% Ta–doped arrays annealed at 650 ˚C, successful H_2 and O_2 generation was confirmed by GC analysis. A current to H_2 and O_2 conversion efficiency of approximately 87 % was observed when holding the anodic layers upon illumination at 430 mV for 20 h. Although one would expect a current conversion efficiency of *ca.* 100 %, the slightly lower value

we observed might be due to little loss of evolved gas, *i.e.*, H_2 and O_2, occurred during the 20 h-long run.
Finally, Fig. 5(D) summarizes maximum photocurrent density (recorded at 430 mV) for pure and 0.1 at% Ta–doped TiO_2 NT arrays as a function of the film thickness. Aside from 0.1 at% Ta–doped NT annealed at 650 ˚C, the film thickness only slightly affected the photocatalytic performance of the anodic oxides within the investigated range. Only a mild decrease of the photoresponse was observed when increasing the NT length up to 12 μm. This trend can be ascribed to the competition between two opposing features, namely, the maximum light absorption (achieved with NT layers thicker than the penetration depth of light) and the diffusion length of charge carriers. Thus, 3 to 7 μm thick nanotubes generally exhibited a better water-splitting ability by allowing full-light absorption and limiting electron–hole recombination, as already observed [2,13]. However, by comparing the photoresponse for NT arrays with the same thickness, it is clear that 0.1 at% Ta-doped films always led to higher photoresponse than pure TiO_2 NT, regardless of the annealing temperature.

8.5 Conclusion & Further Work

Self-organizing anodization of Ti–Ta alloys was shown to be a straight-forward method for the single-step growth of Ta-doped TiO_2 nanotubes arrays. A fine control of Ta content in the tubes can be easily attained by tuning the concentration of the dopant within the alloy. Nevertheless, the Ta content within the anodic nanotube arrays was shown to be homogeneous. Compared to pure TiO_2 nanotubes, improved water splitting ability can be attained with Ta-doped tubes grown and crystallized under specific conditions (*i.e.*, Ta content of 0.1 at% and annealing in air at 650 ˚C). These results can be ascribed to an enhanced electrical conductivity of crystalline Ta-doped TiO_2 nanotubes composed of mixed anatase–rutile structure.
However, although the effects of the presence of Ta, as well as that of Nb or Ru, within TiO_2 structures have been already observed and studied for different applications [1,2,10-16], the physico-chemical properties of Ta-doped TiO_2 nanotubes must be investigated more in depth. For example, an X-ray absorption spectroscopy study might provide useful information to understand the crystallographic features of Ta-doped tubes, and to ascertain where Ta is located within the titania structure and its oxidation state. In other words, though enhanced properties of Ta-, Nb- and Ru-doped TiO_2 were corroborated in the last decade, it is still not well known whether Ta,

for instance, diffuses within the TiO_2 lattice as a dopant (and, if so, whether it occupies interstitial or substitutional positions) or it forms segregated clusters of Ta oxide (therefore generating mixed oxides and heterojunctions). It would be also interesting to understand whether doping and mixed oxide formation preferentially occur for different amounts of Ta within the alloy. Nevertheless, X-ray absorption spectroscopy studies might be performed *in situ* while growing the anodic films. By this approach, the concentration and chemical state of the different elements (*e.g.*, Ti and Ta) can be investigated and traced during the growth of nanotubes, possibly highlighting unknown aspects concerning the mechanism of tubes growth, doping and/or heterojunctions formation, possible preferential dissolution of certain elements and consequent accumulation of others within the anodic films. Last but not least, a better understanding of all these aspects might help to rationalize why the presence of rutile phase is needed for Ta-doped TiO_2 nanotubes in order to exhibit high water splitting ability.

8.6 References & Notes

[1] M. Altomare, K. Lee, M.S. Killian, E. Selli, P. Schmuki, Chem. Eur. J. 19 (2013) 5841.
[2] P. Roy, C. Das, K. Lee, R. Hahn, T. Ruff, M. Moll, P. Schmuki, J. Am. Chem. Soc. 133 (2011) 5629.
[3] J. H. Park, S. Kim, A. J. Bard, Nano Lett. 6 (2006) 24.
[4] M. Law, J. Goldberger, P. Yang, Annu. Rev. Mater. Res. 34 (2004) 83.
[5] R. Jennings, A. Ghicov, L. M. Peter, P. Schmuki, A. B. Walker, J. Am. Chem. Soc. 130 (2008) 13364.
[6] M. Grätzel, Inorg. Chem. 44 (2005) 6841.
[7] K. Zhu, T. B. Vinzant, N. R. Neale, A. J. Frank, Nano Lett. 7 (2007) 3739.
[8] P. Roy, D. Kim, K. Lee, E. Spiecker, P. Schmuki, Nanoscale 2 (2010) 45.
[9] P. Roy, S. Berger, P. Schmuki, Angew. Chem. Int. Ed. 50 (2011) 2904.
[10] P. Triggs, F. Lévy, Phys. Status Solidi B 129 (1985) 363.
[11] D. Morris, Y. Dou, J. Rebane, C. E. J. Mitchell, R. G. Egdell, D. S. L. Law, A. Vittadini, M. Casarin, Phys. Rev. B 61 (2000) 13445.
[12] Y. Furubayashi, Y. Yamamoto, K. Inaba, G. Kindo, Y. Hirose, T. Shimada, T. Hasegawa, Appl. Phys. Lett. 86 (2005) 252101(1).
[13] C. Das, P. Roy, M. Yang, H. Jha, P. Schmuki, Nanoscale 3 (2011) 3094.
[14] M. Yang, D. Kim, H. Jha, K. Lee, J. Paul, P. Schmuki, Chem. Commun. (2011) 2032.
[15] S. So, K. Lee, P. Schmuki, Phys. Status Solidi RRL 6 (2012) 169.

[16] K. Lee, P. Schmuki, Electrochem. Commun. 25 (2012) 11.
[17] I. Paramasivam, H. Jha, N. Liu, P. Schmuki, Small 8 (2012) 3073.
[18] W. Wei, S. Berger, N. Shrestha, P. Schmuki, J. Electrochem. Soc. 157 (2010) C409.

9. Au-Decorated TiO_2 Nanotubes

9.1 Overview

The growth of Au nanocluster-decorated TiO_2 nanotubes is herein discussed. Au-decorated tubes were grown by electrochemical anodization of Ti-Au alloys and were employed as photocatalytic materials for H_2 production from water-ethanol solutions, exhibiting widely enhanced photoactivity compared to either bare nanotube layers or compact anodic TiO_2 films decorated with Au nanoparticles. Moreover, parameters such as the concentration of Au within the alloys and the anodization time could be varied to tune Au nanoclusters dimensions and spacing between each other. The results presented in this chapter have been published in ref. [1].

9.2 Aim

As discussed in the previous chapter, one of the simplest, yet effective, ways to modify the properties of anodic TiO_2 nanotubes consist in the self-organizing anodization of Ti-X alloys, where X is typically another metal such as Nb, Ta or Ru that is present within the alloy in relatively small concentration. The additional metal undergoes simultaneous oxidation during the electrochemical anodization and is incorporated into the TiO_2 structure as secondary oxide or as a dopant (in substitutional or interstitial position), giving specific functionalities to nanotubes (*e.g.*, through doping, band gap engineering, formation of heterojunctions) [2-7].
The feasibility of forming nanotube structures from gold-titanium alloys is herein discussed. This approach resulted particularly interesting since noble metals (*e.g.*, Au, Pt) are not expected to undergo oxidation during the anodization process. Therefore, TiO_2 nanotube layers showing homo-geneous, well-defined and controllable decoration with elemental Au nanoclusters (Au NCs) can be fabricated, through anodization of Ti-Au alloys with Au concentration within a certain range.
Composite materials as Au NCs on TiO_2 are of large interest for photocatalytic H_2 production from renewable sources such as water-ethanol solutions [8-11]. In such processes, as discussed also in Chapters 4 and 5, TiO_2 acts as wide band-gap semiconductor able to absorb UV-light (hence,

generating e^--h^+ pairs) whereas, Au NCs act as co-catalyst, the absence of which would lead to only negligible H_2 production, especially when water splitting is performed under open circuit conditions (*i.e.*, without external voltage applied). In this context, noble metal co-catalysts on TiO_2 have two important roles, *i)* acting as H_2 recombination clusters and *ii)* inducing the bending of valence and conduction band at the surface of the semiconductor, thus facilitating electron-hole separation [10-17].
In terms of photocatalytic efficiency and in view of an economic use of Au, the distribution of Au NCs (*i.e.*, dimensions and spacing of Au NCs) is of utmost importance. Therefore, the effects of Au concentration (within the alloys) and anodization time on the dimension and distribution of Au NCs formed on anodic TiO_2 nanotubes have been investigated, in order to maximize the photocatalytic H_2 evolution from water-ethanol mixtures.

9.3 Characterization

Fig. 1(A)-(C) show SEM and TEM images of Au NCs-decorated TiO_2 nanotubes fabricated by anodizing 0.2 at% Au-Ti alloys in conventional ethylene glycol-based electrolyte containing 0.2 M HF and 1.0 M H_2O. The anodic layers were grown at 120 V for 2 h (the experimental procedure for the fabrication of Au-decorated nanotubes is fully described in Section 3.2.3). Clusters of Au with average diameter of ~ 4-6 nm and uniformly spread over the TiO_2 nanotube were formed. Selected area diffraction (SAD) pattern in Fig. 1(D), taken at tubes bundle with a high density of Au clusters, resulted consistent with the presence of crystalline Au^0. Moreover, anodic TiO_2 nanotubes are amorphous, as already discussed in Chapter 7 and 8, therefore no diffraction from crystalline TiO_2 can be observed in the SAD pattern.
To crystallize the tubes as anatase polymorph, the anodic films were annealed at 450 °C for 1 h in air. XRD patterns of annealed layers are shown in Fig. 2(A). XRD spectra for Au-containing tubes shown in Fig. 1 and annealed at 450 °C show a conversion of amorphous oxide into anatase phase, with also small amounts of rutile (Fig. 2(A)). Au peaks could be observed only for nanotubes grown on 0.2 at% Au-Ti alloys, this most likely because lower amounts of Au were below the XRD detection limit. SEM images of annealed tubes (Fig. 1(E)) showed, at a first sight, that no significant change of Au cluster size occurred. However, a quantitative evaluation (Fig. 1(G)) of more than ten TEM images revealed a little increase of the average Au particle size upon annealing, from *ca.* 6 to 8 nm. This can

be attributed to enhanced surface diffusion of Au at 450 °C. As expected, for higher Au concentration in the alloy, the density of clusters increased (a quantitative evaluation is shown in Fig. 1(F)). On the other hand, the average particle size was still comparable to that observed for lower Au content, *i.e.*, 4-6 nm.

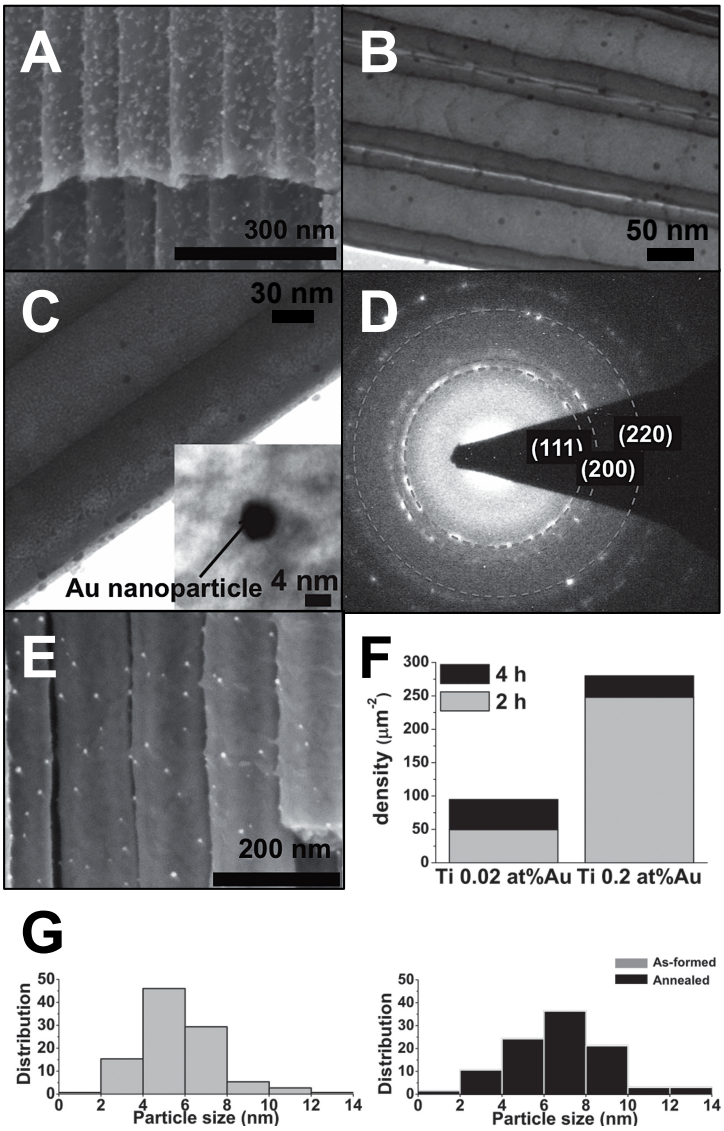

Figure 1 – (A) Cross-sectional SEM image and (B)-(C) TEM images of Au-decorated TiO_2 nanotubes formed on 0.2 at% Au-Ti alloys. Inset in (C) shows high-magnified TEM image of a Au nanocluster on TiO_2 nanotubes wall. (D) SAD patterns of as-formed Au-decorated TiO_2 nanotubes. (E) SEM image of Au-decorated TiO_2 nanotubes annealed at 450 °C. (F) Statistical decoration density as a function of anodization time and Au-content within the alloys. (G) Size distribution of Au particles on TiO_2 nanotubes.

Interestingly, extended anodization times led to higher density of clusters. This demonstrated that the density of Au NCs was actually related to the time the TiO_2 nanotubes were exposed to the electrolyte. In fact, since the electrolyte contained fluoride species that permanently mildly etched TiO_2 (to form soluble $[TiF_6]^{2-}$), the walls of the tubes are typically thinner at the top than at the bottom [18-20]. Therefore, one may conclude that by etching, larger amounts of elemental Au, originally embedded within the tubes, were exposed to the surface of the walls, where Au NCs likely formed by surface diffusion-nucleation process. In fact, TiO_2 needles ("grass", [18-21]) with a large amount of Au particles at the top of the anodic layers were obtained when anodizing for very long anodization time (Fig. A1 in Section 9.6).

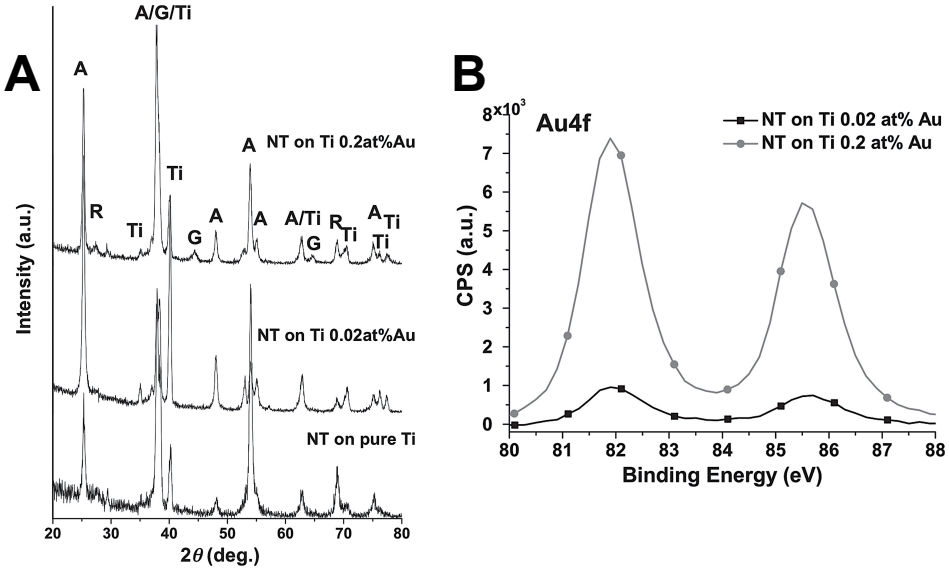

Figure 2 – (A) XRD patterns of annealed TiO_2 nanotubes grown on Au-Ti alloys with different Au-contents. The peaks are annotated as anatase TiO_2 (A), rutile TiO_2 (R), Ti metal (Ti) and Au (G). Annealing was carried out at 450 °C in air for 1 h. The thickness of the nanotubes layers was *ca.* 13 µm. (B) XPS spectra of Au 4f doublet detected for tubes grown on Au-Ti alloys with different Au-contents.

Yet, it is also noteworthy that for higher concentration of Au in the alloy, *e.g.*, higher than 1 at%, no TiO_2 nanotubes were formed but only Au nano-particles were directly released into the electrolyte during the anodization process. Therefore, also the loss of Au particles appeared more pronounced when increasing the concentration of Au in the substrates.

The presence of Au at the surface of TiO_2 NT was verified also by XPS analysis, the high-resolution spectrum showing the typical Au 4f doublet (Fig. 2(B)) with peak shape and binding energy values consistent with metallic Au [22]. Moreover, in order to assess the concentration of Au within the nanotube layers, energy dispersive X-ray (EDX) spectroscopy was performed (Fig. A2(A) and (B) in Section 9.6). For 0.02 and 0.2 at% Au-Ti

alloys, Au amounts of around 0.13 and 0.42 at% were detected within the anodic films, respectively, when anodization experiments were performed for 2 h. On the other hand, the concentration of Au considerably increased for extended anodization times (Fig. A2(B)), *i.e.*, the density of Au NCs depended not only on the Au content within the alloy but also on the anodization time.

9.4 Photocatalytic Production of H_2

The photocatalytic activity of Au nanoclusters-decorated TiO_2 nanotubes was studied by evaluating the H_2 production from water-ethanol solutions. The results were interpreted in relation to different Au loadings of the tubes (obtained by anodizing substrates with different Au contents) and different annealing temperatures (*i.e.*, different phase composition of the anodic films). All photocatalytic experiments lasted 6 h, were carried out under open circuit condition (that is, without applying any electrical bias) and under UV light irradiation at 325 nm, employing a HeCd laser (60 mW cm^{-2}). The production of H_2 was measured by gas chromatographic (GC) analysis (all details concerning experimental set-up and analytical methods are reported in Section 3.6.5).

As illustrated in Fig. 3(A), H_2 production on tubes grown from 0.2 at% Au-Ti alloys and annealed at 450 ˚C resulted steady over time, with an average production rate around 35.2 μL_{H2} h^{-1}. Moreover, the possibility of Au NCs release from the tubes into the liquid medium was excluded by performing stability tests. Thus, photocurrent measurements under open circuit voltage (OCV) conditions were carried out, without any photocurrent drop over time (Fig. A3 in Section 9.6), hence ensuring that Au NCs were strongly anchored at the tubes surface.

Additional preliminary experiments were performed to assess the effect of ethanol concentration in the water-ethanol solutions employed in the photocatalytic H_2 production on Au-decorated NT grown by anodizing 0.02 at% Au-Ti substrates. As shown in Fig. 3(B), the highest amount of hydrogen (136.5 µL after 6 h) was produced from 20 vol% ethanol-H_2O solutions, in full agreement with the results obtained employing water-methanol solutions [23].

The amount of H_2 produced on Au-modified tubes decorated with different loadings of Au NCs is reported in Fig. 3(C). Unmodified TiO_2 nanotubes and a compact anodic TiO_2 layer, the latter loaded with similar density of Au clusters, were also prepared and tested for the sake of comparison.

Regardless of the Au loading, Au-decorated tubes led to dramatically higher production of hydrogen compared to both unmodified tubes (6.95 µL of H_2 after 6 h) and compact anodic layer decorated with sputtered Au NPs (3.7 µL of H_2 after 6 h). Among the Au-decorated NT, the most photoactive materials were the tubes grown on 0.2 at% Au-Ti alloys, with a production of 217.7 µL of H_2 after 6 h, that was *ca.* 60 % higher than the production measured for nanotubes formed on 0.02 at% Au-Ti alloys (136.5 µL of H_2 after 6 h).

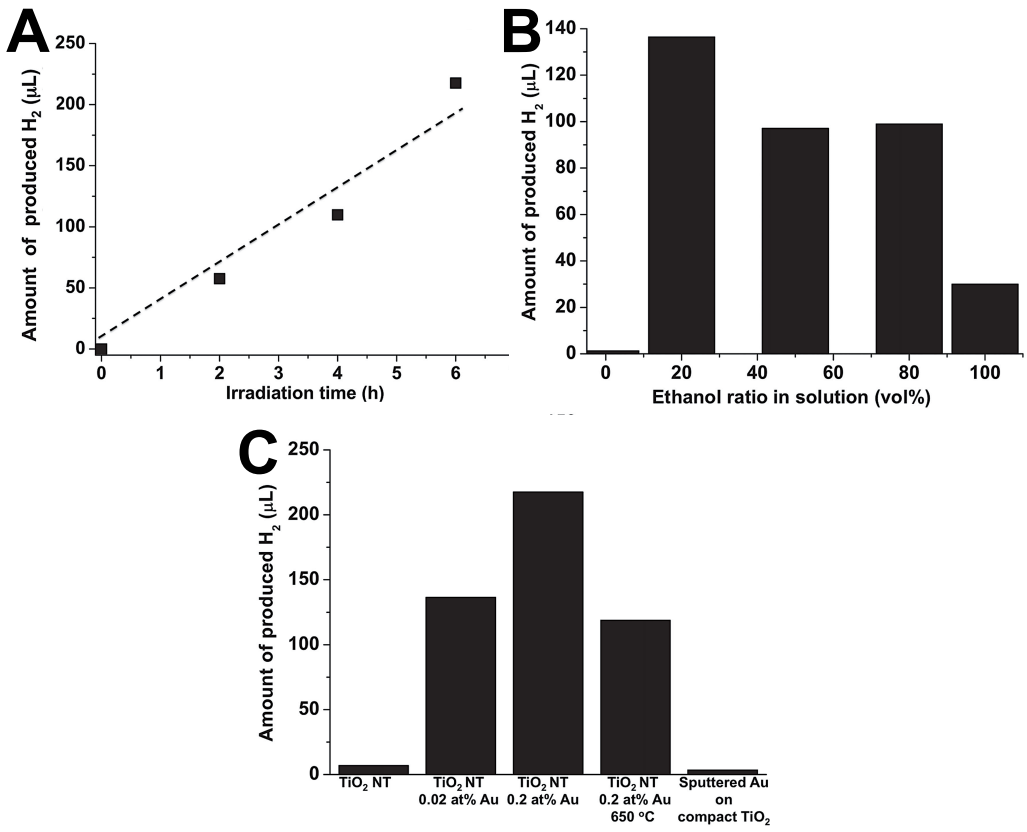

Figure 3 – (A) H_2 production over irradiation time from 20 vol% ethanol-water solutions for Au-decorated TiO_2 nanotubes grown on 0.02 at% Au-Ti alloys. The Au-decorated tubes were annealed in air at 450 °C for 1 h. (B) Photocatalytic H_2 production as a function of the concentration of ethanol within the water-ethanol solutions. The experiments were performed with Au-decorated TiO_2 nanotubes grown on 0.02 at% Au-Ti alloys. (C) Photocatalytic H_2 production from 20 vol% ethanol-water solution with different types of bare and Au-decorated TiO_2 anodic films. The thickness of nanotubes layer was *ca.* 13 µm. All experiments were carried out for 6 h under UV-light irradiation (325 nm HeCd laser, 60 mW cm^{-2}).

The effect of phase composition of the nanotubes, which is determined by the annealing temperature, on the amounts of produced H_2 was also investigated. Therefore, nanotubes layers grown on 0.2 at% Au-Ti substrates were annealed at 650 °C in order to convert the amorphous oxide into a

rutile rich structure (related SEM pictures and XRD pattern are shown in Fig. A4(B)-(D) in Section 9.6). Au-decorated rutile-rich nanotubes exhibited a production of 118.9 μL of hydrogen after 6 h, hence pretty lower than that measured for the film grown under same conditions but annealed at 450 ˚C, *i.e.*, anatase-rich tubes (Fig. 3(B)). This result is in agreement with general findings demonstrating that rutile typically exhibits faster electron-hole recombination and lower photoactivity compared to the anatase phase [24-26]. The comparison between compact TiO_2 film decorated with sputtered Au and nanotubes loaded with similar amount of Au NCs showed that high specific surface area, provided by nanotubes arrays, was necessary in order to attain high photocatalytic performance, in agreement with what expected for any process related to heterogeneous catalysis.

9.5 Conclusion & Further Work

Anodization of Au-Ti alloys was proved to be an effective way to grow Au nanoclusters-decorated TiO_2 nanotubes arrays in a single-step process. Generally, the Au crystals were 4-6 nm large and, most of all, they resulted homogeneously spread over the walls of the tubes. The decoration density (*i.e.*, the spacing between the clusters) could be finely controlled both by tuning the amount of Au within the alloy and by the anodization time. Au-decorated tubes were tested as for H_2 photocatalytic production from water-ethanol solutions. The results demonstrated that nanotubular structure combined with noble metal nanoparticles decoration triggered the hydrogen production rate. Yet, the hydrogen production was affected by the concentration of ethanol within the solution, the crystallographic features of the tubes and, most interestingly, by the Au decoration density.
In this context, a particular strength of this approach is the possibility of tuning the spacing between the Au clusters to an optimum value in order to boost the production of hydrogen. Considering the semiconductor-noble metal junctions, an optimum NM particle decoration density would be reached when the width of the space charge layers induced by neighboring noble-metal particles overlap with each other. Therefore, not only the absolute amount of loaded Au and the clusters dimensions, but also the spacing between the Au clusters must be taken into account in view of fabricating high-performance photocatalytic devices.
Another consideration must be oriented toward economical aspects concerning the use of expensive noble metals. In fact, the optimal density of Au nanoclusters decoration could be attained even by extended anodization

of low Au-content Ti alloys, since long anodization times were proved to increase the decoration density, this finding being an additional key strength of the process described herein.
Moreover, such accurate adjustment of cluster density represents an important advantage over other attempts to decorate nanotubes, such as by physical vapor deposition (PVD) or impregnation, where fine control of spacing and cluster size is much more difficult.
Nevertheless, the approach discussed herein, *i.e.*, co-catalyst decoration of TiO_2 nanotubes through anodization of Ti-based alloys, could be, in principle, easily transferred to a wide number of systems and applications, as corroborated by few preliminary, yet promising experiments performed with Ti-Pt and Ti-Ag alloys (see Fig. A5 in Section 9.6).

9.6 Appendix

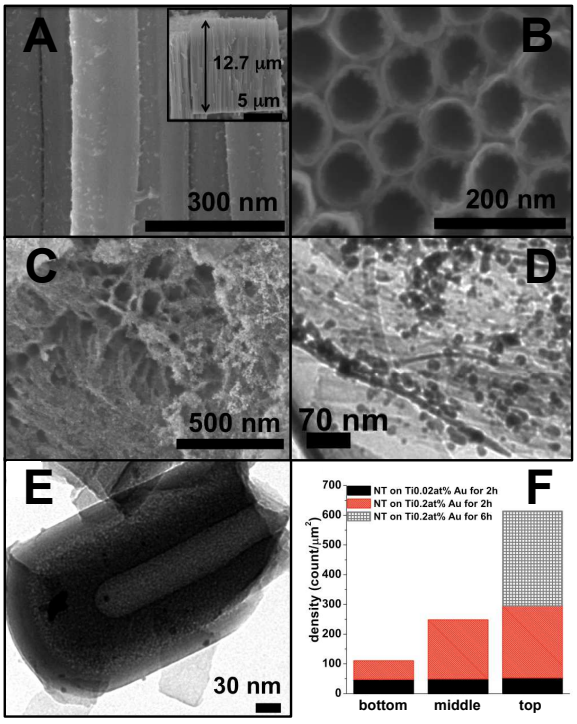

Figure A1 – (A) SEM Cross-section of Au-decorated TiO_2 NT grown on 0.02 at% Au-Ti alloys. The inset shows the thickness of the film. SEM images of (B) plane view and (C) top, and TEM images of (D) top surface and (E) bottom of Au/NT grown on 0.2 at% Au-Ti alloy. Anodization conditions: 120 V, ethylene glycol-based electrolyte containing 0.2 M HF and 1.0 M H_2O. (F) Statistical distribution of Au NCs on the tubes.

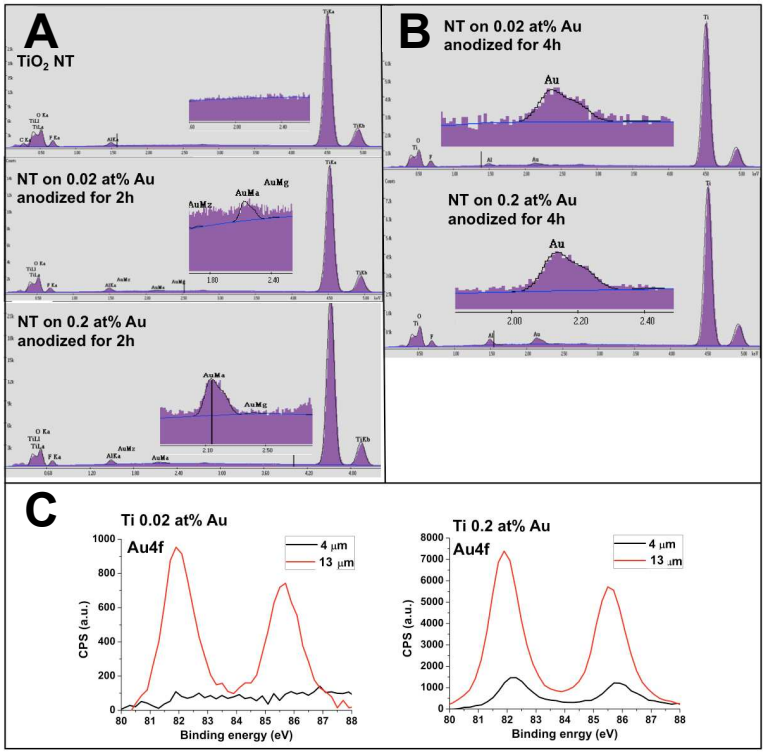

Figure A2 – (A)-(B) EDX spectra of bare and Au-decorated TiO_2 nanotubes grown on Ti-Au alloys. Anodization was carried out for (A) 2 and (B) 4 h. (C) XPS spectra of Au 4f doublet with a comparison for different thickness of the layers grown on Ti-Au alloys (*i.e.*, different anodization time). 4 μm thick TiO_2 nanotubes were formed by anodization at 120 V for 30 min in ethylene glycol-based electrolyte containing 0.2 M HF and 1.0 M H_2O.

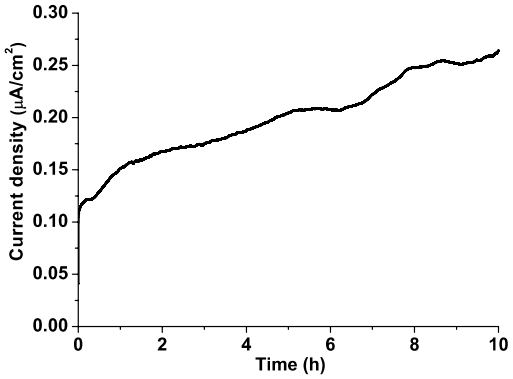

Figure A3 – Photocurrent density measured with 13 μm thick Au-decorated TiO_2 nanotubes from 20 vol% ethanol-water solution under open circuit voltage conditions. Au-decorated TiO_2 nanotubes were formed on 0.2 at% Au-Ti alloy.

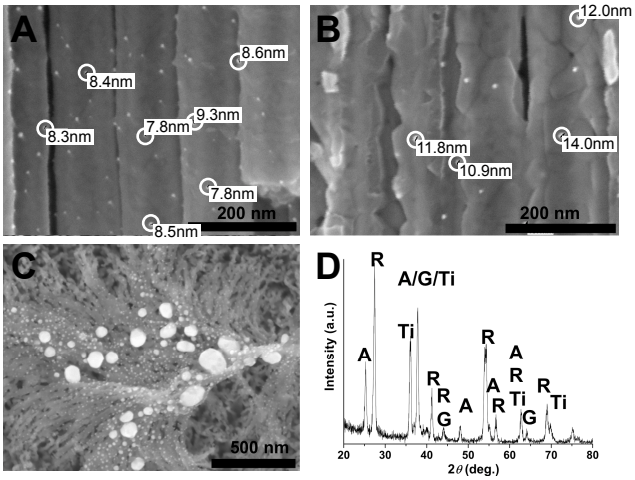

Figure A4 – (A)-(C) SEM images of Au-decorated TiO_2 nanotubes annealed at (A) 450 ˚C and (B)-(C) 650 ˚C in air. (D) XRD spectra of the layer shown in (B) and (C). Nanotubes were formed by anodization at 120 V for 2 h on 0.2 at% Au-Ti alloy in ethylene glycol-based electrolyte containing 0.2 M HF and 1.0 M H_2O. The layer thickness was *ca.* 13 µm.

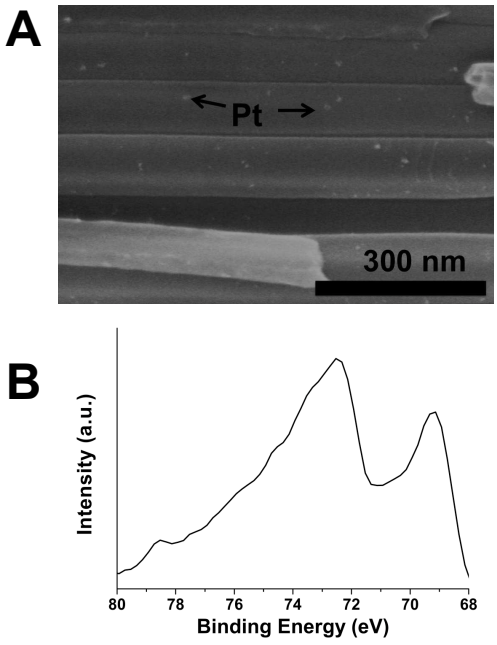

Figure A5 – Example of *in situ* Pt-decoration of TiO_2 NT. (A) SEM cross-section of Pt-decorated TiO_2 NT formed on 0.2 at% Pt-Ti alloy. (B) XPS spectra of the Pt 4f doublet for Pt-decorated TiO_2 nanotubes. Binding energy values are consistent with Pt^0.

9.7 References & Notes

[1] K. Lee, R. Hahn, M. Altomare, E. Selli, P. Schmuki, Adv. Mater. 25 (2013) 613.

[2] A. Ghicov, S. Aldabergenova, H. Tsuchyia, P. Schmuki, Angew. Chem. Int. Ed. 45 (2006) 6993.

[3] P. Roy, C. Das, K. Lee, R. Hahn, T. Ruff, M. Moll, P. Schmuki, J. Am. Chem. Soc. 133 (2011) 5629.

[4] M. Yang, D. Kim, H. Jha, K. Lee, J. Paul, P. Schmuki, Chem. Commun. 47 (2011) 2032.

[5] K. Lee, P. Schmuki, Electrochem. Commun. 25 (2012) 11.

[6] M. Altomare, K. Lee, M.S. Killian, E. Selli, P. Schmuki, Chem. Eur. J. 19 (2013) 5841.

[7] N.K. Allam, A.J. Pomcheri, M.A. El-Sayed, ACS Nano 5 (2011) 5056.

[8] B. O'Regan, M. Grätzel, Nature 353 (1991) 737.

[9] M. Murdoch, G.I.N. Waterhouse, M.A. Naddem, J.B. Metson, M.A. Keane, R.F. Howe, J. Liorca, H. Idriss, Nat. Chem. 3 (2011) 489.

[10] M.A. Naddem, M. Murdoch, G.I.N. Waterhouse, J.B. Metson, M.A. Keane, J. Liorca, H. Idriss, J. Photochem. Photobiol. A 216 (2010) 250.

[11] G.R. Bamwenda, S. Tsubota, T. Nakamura, M. Haruta, J. Photochem. Photobiol. A. 89 (1995) 177.

[12] A. Fujishima, X. Zhang, D.A. Tryk, Surf. Sci. Rep. 63 (2008) 515.

[13] A.M. Linsebigler, A. Lu, J.T. Yates, Chem. Rev. 95 (1995) 735.

[14] M.K. Seery, R. George, P. Floris, S.C. Pillai, J. Photochem. Photobiol. A 189 (2007)258.

[15] N. Sobana, M. Muruganadham, M. Swaminathan, J. Mol. Catal. A 258 (2006) 124.

[16] J. Kiwi, M. Grätzel, J. Phys. Chem. 88 (1984) 1302.

[17] K. Saito, A. Kudo, Dalton Trans. 42 (2013) 6867.

[18] P. Roy, S. Berger, P. Schmuki, Angew. Chem. Int. Ed. 50 (2010) 2904.

[19] A. Ghicov, P. Schmuki, Chem. Commun. (2009) 2791.

[20] S.P. Albu, P. Roy, S. Virtanen, P. Schmuki, Israel J. Chem. 50 (2010) 453.

[21] Needles-like TiO_2 structures, typical of extended anodization time, are formed by chemical etching of the nanotubes walls occurring to a large extent at the top of the anodic films, *i.e.*, at the locations that have been in contact with the electrolyte for relatively long time.

[22] A. M. Linsebigler, A. Lu , J.T. Yates, Chem. Rev. 95 (1995) 735.

[23] G.L. Chiarello, D. Ferri, E. Selli, J. Catal. 280 (2011) 168.

[24] R. Katoh, M. Mural, A. Furube, Chem. Phys. Lett. 461 (2008) 238.

[25] G. Rothenburger, J. Moser, M. Grätzel, N. Serpone, D.K. Sharma, J. Am. Chem. Soc. 107 (1985) 8054.

[26] D.P. Colombo, K.A. Russell, J. Saeh, D.E. Skinner, J.J. Cavaleri, R.M. Bowman, Chem. Phys. Lett. 232 (1995) 2.

10. Au Nanoparticles-Filled TiO_2 Nanocavities

10.1 Overview

A new photocatalytic platform fabricated by an innovative anodization approach followed by an Au dewetting step is discussed in this chapter. Titanium substrates were anodized in a hot H_3PO_4-HF electrolyte allowing the formation of TiO_2 nanocavities arrays exhibiting an unprecedented degree of self-ordering. Afterwards, these anodic nanocavities were covered by thin sputtered Au layers. The last step of the fabrication, *i.e.*, a specific thermal treatment, induced *i)* the crystallization of the amorphous anodic oxide into crystalline titania and *ii)* the self-ordering dewetting of Au, leading to the formation of sphere-shaped Au nanoparticles (NPs) within the TiO_2 nanocavities. Such a highly self-ordering dewetting process could not be attained with TiO_2 nanotubes grown by conventional approaches because of lack in structure regularity. The Au NPs-filled TiO_2 nanocavities were tested as photocatalysts for H_2 production from water-ethanol solutions, showing widely triggered photoactivity compared to compact TiO_2 films decorated with similar loadings of Au. These results revealed that structure and geometry of a photocatalyst represent a key point for improving the photocatalytic activity. The data and results presented in this chapter have been published in ref. [1].

10.2 Aim

By far, the most used semiconductor metal oxide in UV light-assisted photocatalysis is TiO_2. Though having a wide number of beneficial features, titania typically shows poor activity when used as a pure oxide for hydrogen production through photocatalytic splitting of water. Therefore, a few experimental conditions must be established in order to attain higher rates of H_2 production. For instance, the presence of methanol or ethanol leads to a widely enhanced H_2 production rate since the organic species, acting as hole scavenger, undergo efficient and quick photocatalytic oxidation to CO_2 by reacting (directly or indirectly) with *VB* holes, hence limiting the charge recombination process [2]. Other solutions imply the nanostructuring of the semiconductor (*i.e.*, fabrication of nanotubes [3]) or the deposition of noble

metal nanoparticles (NM NPs as co-catalyst [4]) at the photocatalyst surface, the former basically leading to high specific surface area materials, the latter providing effective charge carriers separation, since *CB* electrons are efficiently trapped by the noble metal deposits.

In the previous chapter, the fabrication of Au nanoclusters-decorated TiO_2 nanotube arrays was obtained by electrochemical anodization of Au-containing Ti-based alloys. Though a fine control of the Au nanoclusters dimensions and spacing was attained, TiO_2 nanotubes presented well-known characteristics in terms of morphology since they were grown through a conventional anodization approach.

On the other hand, other approaches (*i.e.*, chemical vapor deposition (CVD), impregnation, photo-deposition) typically lead to inhomogeneous deposition of NM particles, thus providing a comparably low control on the semiconductor geometry (noble metal nanoparticles location, size, and distribution). As a consequence, one would reasonably expect that a system characterized by a non-optimized morphology could exhibit a suboptimum photocatalytic efficiency given by a certain lack of control over the synthesis.

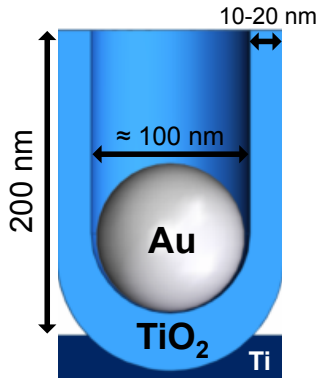

Figure 1 – Sketch of an ideal Au/TiO_2 photocatalytic nano-reactor for efficient UV-light driven processes.

An entirely new fabrication approach for growing highly defined Au NPs in TiO_2 nanocavities arrays is described in this chapter, along with the use of such arrays as efficient photocatalytic materials for H_2 generation from water-ethanol liquid mixtures.

The fabrication of these highly ordered surfaces relies on the synergetic overlay of two self-organizing processes. In a first step, self-organized TiO_2 nanotubes exhibiting unprecedented morphology (*i.e.*, a nanocavity-like structure) and long-range order were fabricated through an innovative anodization approach. Afterwards, these hexagonally patterned TiO_2 layers were used as platform for dewetting of Au thin layers, a process for which

the ideal geometry of the TiO_2 substrate was an absolute prerequisite for the self-ordering formation of Au nanoparticles.
Overall, the process discussed herein not only allowed a fine control of the size and distribution of the Au NPs but also led to the fabrication of a new generation of TiO_2 nanotubes with tunable properties for specific applications [1,5,6].

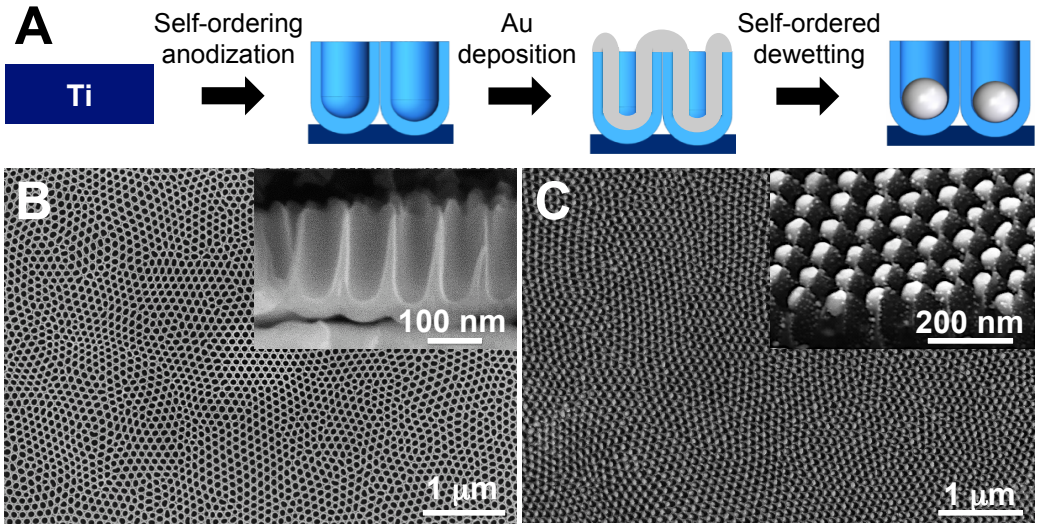

Figure 2 – (A) Fabrication of an array of Au nanoparticles embedded in TiO_2 nanocavities grown by self-organizing anodization. (B) Top view and cross-sectional (inset) SEM images of a highly ordered TiO_2 cavities arrays (individual cavity length *ca.* 200 nm, top width *ca.* 80 nm, wall thickness *ca.* 15 nm) grown on a Ti substrate. (C) Top view and cross-sectional (inset) SEM images showing the filling of the nanocavities with exactly one Au nanoparticle per cavity.

Moreover, these TiO_2 cavities would be ideal for photocatalytic applications and UV-light assisted reactions. In fact, the cavities, being *ca.* 200 nm deep and 80 nm in diameter, might provide a well designed photocatalytic reaction vessel (see Fig. 1) with a geometry that fulfills the requirements of absorption depth of UV-light (some 100 nm cavity length), diffusion range of radicals generated at the TiO_2 surface and injected into the environment (*e.g.*, 10 – 100 nm for $^{\bullet}OH$) and solid-state diffusion length (in the range of cavity wall thickness for photogenerated holes). In other words, the geometry of these TiO_2 vessels might allow the confinement of the entire reactive scenario essentially within each single nanocavity.

10.3 Fabrication & Characterization

The TiO_2 nanotubes discussed herein, the fabrication of which is reported in Section 3.2.4, were formed by an anodization approach where the self-organization was triggered by coupling a high rate of oxide growth together with a high rate of oxide dissolution [7-9], this combination of experimental conditions leading to an unprecedented level of ordering for anodic TiO_2 nanotubes.
The TiO_2 nanotubes arrays were grown in a hot H_3PO_4-HF electrolyte where the tube growth was tailored to a very short tube length so that each nanotube better resembled a nanosized cavity (see Fig. 1) rather than "conventional" anodic nanotubes, such as those described in Chapters 7-9.

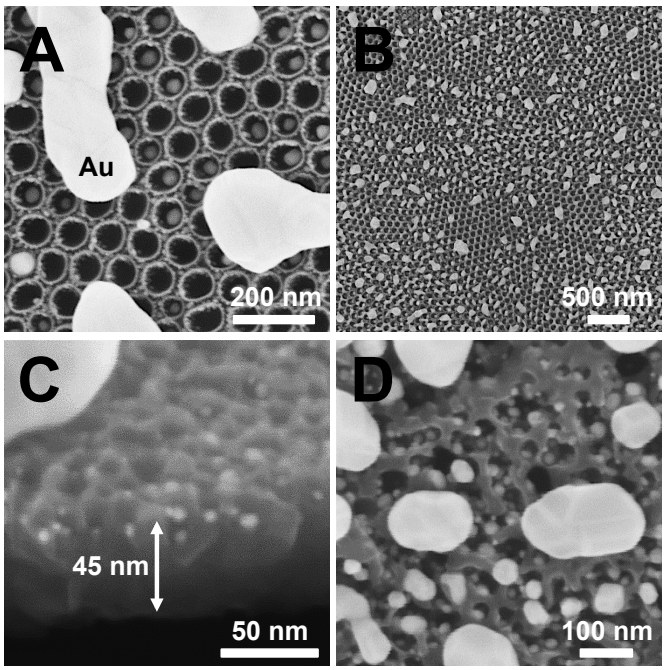

Figure 3 – Examples of non-ideal dewetting conditions: (A) too thick Au film (nominal thickness of 50 nm); (B) dewetting carried out with ideal thickness of the Au film and morphology of the substrate but in Ar atmosphere; (C) too short cavities (*ca.* 50 nm height); (D) not sufficiently ordered nanotubes surface (conventional nanotubes).

To achieve self-ordering deposition of the Au loading within the TiO_2 cavities, homogeneous Au thin layers (of different thickness) were firstly sputtered onto the nanocavity arrays. Afterwards, the formation of Au nanoparticles and the control of their dimensions and distribution were obtained by an optimized thermal dewetting process, as illustrated in Fig. 2.
As such, dewetting of metal thin films on a substrate is a method commonly used to form metallic particles spread on large areas [9-13]. If carried out on

a flat surface, the dewetting process results in metal islands with broad distributions of size and spacing. In this case, the dewetting process occurs through film rupture taking place at random defects (Fig. A1).
However, by using substrates exhibiting a periodic surface topography, *i.e.*, the TiO_2 nanocavities arrays described herein, the dewetting process could be controlled, since the highly ordered topography provided defined initiation sites for rupture events. A similar approach was investigated in the field of semiconductor technology by using litho-graphically structured Si/SiO_2 surfaces [14].

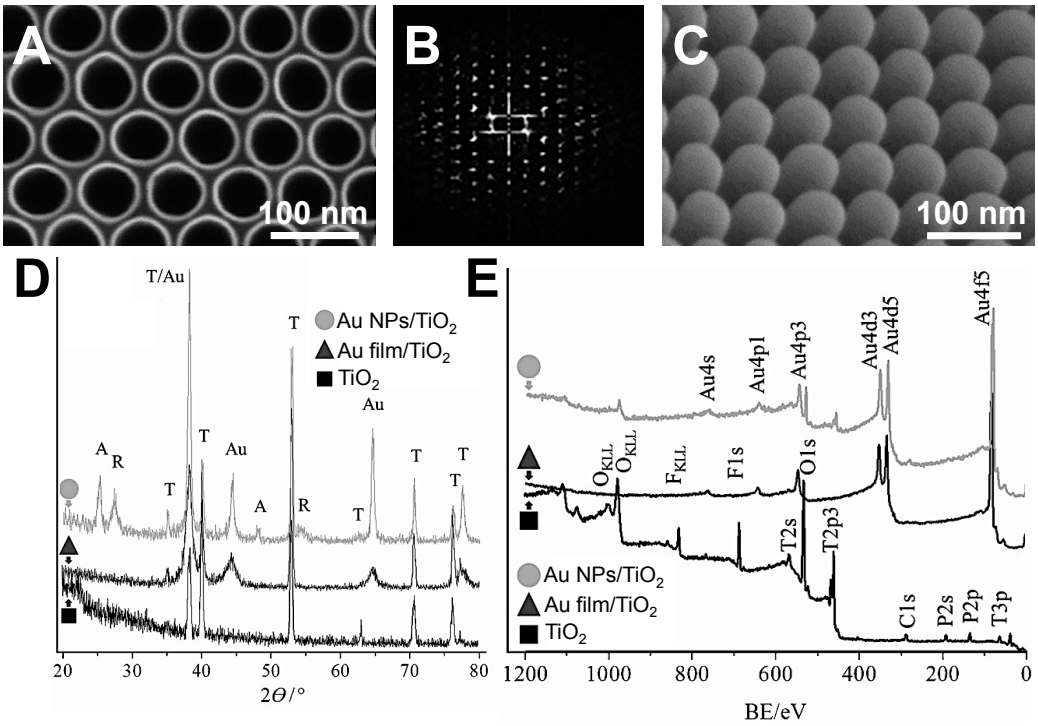

Figure 4 – (A) Top view SEM image of a highly ordered TiO_2 nanocavities arrays fabricated on a Ti metallic substrate by anodization in hot 3 M HF-H_3PO_4 electrolyte. (B) FFT conversion of SEM image shown in (A). (C) Metal replica fabricated by sputtering the ideal filling of the TiO_2 cavities. (D) X-ray diffraction patterns and (E) X-ray photoelectron spectra of as-formed TiO_2 nanocavities, Au-sputtered nanocavities and dewetted Au nanoparticles deposited within the TiO_2 nanocavities (T = Ti, A = anatase, R = rutile, Au = gold).

For an optimized self-organization of the Au NPs, spacing and height of the cavities were tuned in order to allow the formation of homogeneous films of Au that completely covered the anodic arrays. Also the thickness of the Au sputtered layers was precisely adjusted, since it was shown to strongly affect the final dimension and distribution of Au NPS after the dewetting process.
However, the most important parameter in view of fabricating highly ordered Au NPs-filled TiO_2 structures was the degree of self-organization of

the anodic cavities, which was required to be extremely high, otherwise dewetting occurred in a massively imperfect fashion (Fig. 3).
For the structures shown in Fig. 2(C), a 20 nm thick Au film was uniformly deposited on the anodic surface (Fig. 2(B)) and underwent subsequent dewetting by a thermal treatment carried out at 450 ˚C for 30 min in air. Such a treatment led to highly ordered TiO_2 nanocavities arrays filled with exactly one Au spherical-shaped particle per cavity, as shown in the inset of Fig. 1(C). A key strength of this approach was that the filling took place successfully over large surfaces (*i.e.*, in the range of some cm^2). In this context, it is also worth noting that the annealing atmosphere was of significant influence. In fact, when the annealing treatment was performed in Ar atmosphere, quite less ordered structures were obtained (Fig. 3(B)).

Structure	Concentration (at%)					
	C	Ti	Au	O	F	P
TiO_2	8.73	18.1	-	55.1	12.2	4.96
Au film/TiO_2	14.5	0.36	81.0	4.00	0.23	-
Au NPs/TiO_2	17.6	11.2	34.5	36.1	0.41	-

Table 1 – Concentration of different elements in terms of at% measured by X-ray photoelectron spectroscopy analysis of as-formed TiO_2 nanocavities, Au-sputtered nanocavities and dewetted Au nanoparticles deposited within the TiO_2 nanocavities.

Fig. 4 shows several aspects and features of the array formation after each individual step (*i.e.*, anodization, sputtering and dewetting processes). The regularity of TiO_2 nanocavities was properly assessed by fast Fourier transform (FFT) conversion of the SEM images (Fig. 4(A) and (B)). A comparison of the resulting FFT images obtained for various self-organized nanotubes formed by other (*i.e.*, conventional) methods is shown in Fig. A2 (see Section 10.6). The FFT images corroborated that the regularity of structures grown by the approach discussed herein was outstanding and clearly higher than that observed for conventional nanotubes. Another approach to assess the regularity of the structures consisted in depositing a sputtered metal layer on the anodic films until the complete filling-up of the cavities was attained. When the Ti/TiO_2 substrate was selectively etched off in HF, a highly ordered metal replica was left behind, exhibiting an extraordinarily regular patterned surface (see for example Fig. 4(C)).
XRD and XPS (Fig.4 (D) and (E)) showed that as-formed TiO_2 nanocavities consisted of amorphous titania, with typical P and F uptake. After Au

deposition, only the signal of Au was apparent from the top-view XPS analysis, indicating that Au was homogeneously deposited at the top surface of the cavities layers, forming a film that completely covered the anodic oxide. On the other hand, after thermal dewetting, top-view XPS analysis showed that the TiO_2 substrate became "visible" again (as it was before Au sputtering) due to exposure of the dewetted TiO_2 substrate (see inset in Fig. 4(E) and Table 1). Moreover, high-resolution XPS peaks of Au (reported in Fig. A3) proved that a strong interaction was established between the Au nanoparticles and the TiO_2 substrate since the Au XPS doublet appeared at higher binding energy (BE) compared to the BE values observed for Au layers of similar thickness that were sputtered-dewetted on a glass substrate [15].

As shown by the XRD analysis performed after the dewetting process (Fig. 4(D)), the thermal treatment carried out at 450 ˚C in air led, as desired, not only to the formation of isolated Au nanoparticles within the cavities but also to the conversion of the amorphous anodic oxide into a crystalline mixture of anatase and rutile TiO_2.

10.4 Photocatalytic Production of H_2

The photocatalytic behavior of the Au NPs-filled TiO_2 nanocavities was briefly investigated in hydrogen production through photoreforming of water-ethanol liquid solutions under UV-light irradiation (the photocatalytic set-up and analytical methods are described in Section 3.4.5 and were the same employed for the photocatalytic tests discussed in the previous chapter). Although the results obtained with this preliminary investigation were promising, as shown in the following paragraphs, a detailed study is now in progress.

In first experiments with Au-free TiO_2 films (either compact or in the form of nanocavities), no significant amount of H_2 could be detected, these results being in line with the results herein discussed in Chapters 4,5 and 9, which demonstrated that negligible H_2 evolution occurs with co-catalyst-free titania under open-circuit conditions.

Fig. 5(A) shows a comparison of H_2 amounts photoproduced after 9 h-long runs (from 20 vol% ethanol-water solution) on Au NPs-filled TiO_2 nanocavities fabricated as previously described and by depositing different nominal loading of Au (nominal loadings of Au are expressed herein as the thickness of the Au sputtered films). Clearly, Au loadings of 2-3 nm led to the

largest amount of photoproduced H_2. Moreover, Fig. 5(B) shows that H_2 evolution was steady over time, occurring at a rate of *ca.* 6 μL_{H2} h^{-1}.
The mechanical stability of the anodic films was also tested in order to exclude that, for instance, Au NPs could detach from the nanocavities, thus leading to a drop of photocatalytic efficiency. Therefore, photocurrent measurements under open circuit voltage (OCV), *i.e.*, bias-free conditions, were also performed, showing that no drop of current was recorded (see the inset of Fig. 5(B)). Thus, the stability of the current indicated that neither significant poisoning of the co-catalyst (Au NPs), nor other deterioration of the structure took place.

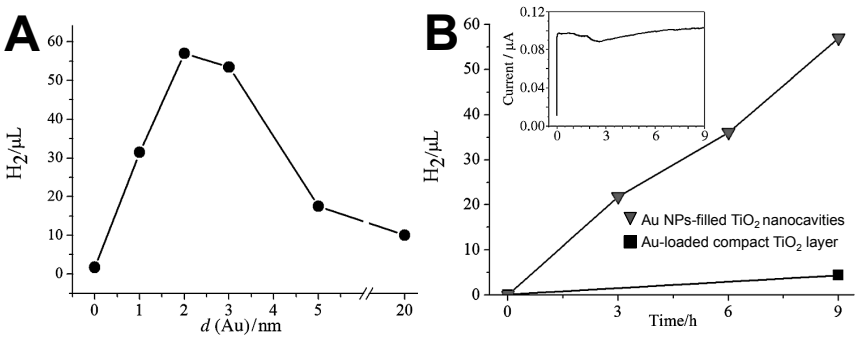

Figure 5 – Photocatalytic H_2 production from 20 vol% ethanol-water solutions under UV-light irradiation (9 h-long runs). (A) Amounts of H_2 evolved on Au NPs-filled TiO_2 nanocavities as a function of the Au layer thickness. (B) Amounts of evolved H_2 over irradiation time for Au NPs-filled TiO_2 nanocavities and a compact TiO_2 oxide loaded with similar amounts of Au and accordingly dewetted. Inset: photocurrent *vs.* irradiation time curve for Au NPs-filled TiO_2 nanocavities under UV light, without applied voltage in water-ethanol solutions.

Most interestingly, the effect of the photocatalyst geometry was remarkable, as shown in Fig. 5(B). In fact, a more than 30-fold increase of H_2 production was observed for Au NPs-filled TiO_2 nanocavities in comparison with an anodic compact TiO_2 layer loaded with similar amounts of Au and accordingly dewetted. Therefore, such an increase of photocatalytic activity observed for Au-loaded nanocavities might be attributed to the ideal photoreactor conditions and geometry outlined in Fig. 1.

10.5 Conclusion & Further Work

An entirely new self-organized strategy to create highly defined arrays of Au nanoparticles in TiO_2 nanocavities was developed. Both the individual steps of fabrication, namely, self-organizing anodization and self-ordered

dewetting, were relatively simple, cheap, yet scalable over large surface areas. More detailed studies on these Au/titania systems are in progress, with a particular attention to trigger the photocatalytic performance by tuning Au NPs size and distribution. Moreover, a key strength of this fabrication approach is its potential application to a wide range of self-ordered oxides and dewettable metals. Therefore, the process as such can be envisaged as an innovative pathway for producing highly efficient co-catalyst/photocatalyst systems when the control of the metal-metal oxide junctions is essential.

10.6 Appendix

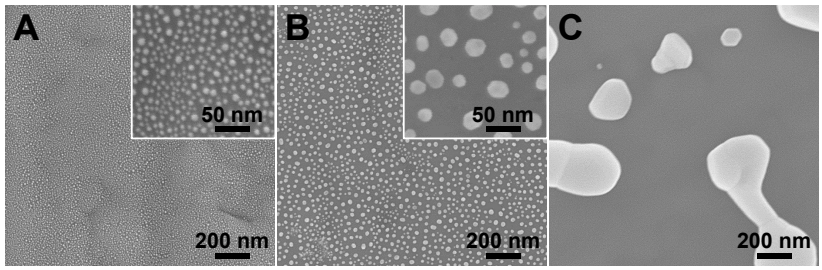

Figure A1 – Top view SEM images of dewetted Au films of different thickness sputtered on TiO_2 compact oxides: (A) 1 nm thick layer; (B) 2 nm thick layer; (C) 20 nm thick layer.

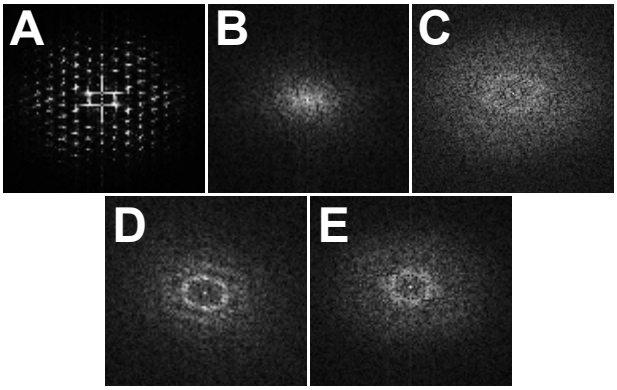

Figure A2 – FFT images of TiO_2 nanotubes formed by anodization in (A) a mixture of H_3PO_4 and 3 M HF at 15 V for 2 h (*i.e.*, highly ordered nanocavities herein described) compared with other conditions typically used for growing highly ordered TiO_2 nanotubes: (B) a mixture of ethylene glycol, 0.2 M NH_4F and 1 M H_2O at 60 V for 2 h [15]; (C) a mixture of glycerol, 0.27 M NH_4F and 40 vol% H_2O at 60 V for 1 h [16]; (D) a mixture of ethylene glycol, 0.135 M NH_4F and 2 vol% H_2O at 60 V for 30 min (2-step anodization) [17]; (E) a mixture of 1 M NaH_2PO_4 and 0.125 M HF at 20 V for 2 h [18].

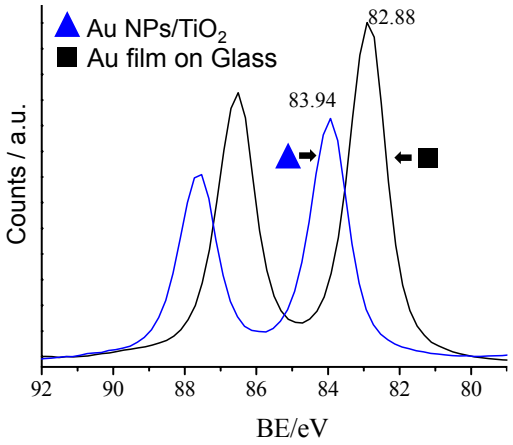

Figure A3 – XPS analysis showing the comparison between the Au signal (doublet) observed for Au sputtered films dewetted on TiO_2 nanocavities and on a glass substrate. According to the literature [14], the observed shift of the Au doublet may indicate a strong Au-TiO_2 interaction.

10.7 References & Notes

[1] J.E. Yoo, K. Lee, M. Altomare, E. Selli, P. Schmuki, Angew. Chem. Int. Ed. 52 (2013) 7514.
[2] P. Pichat, New J. Chem. 11 (1987) 135.
[3] I. Paramasivam, H. Jha, N. Liu, P. Schmuki, Small 8 (2012) 3073.
[4] G.R. Bamwenda, S.T Subota, T. Nakamura, M. Haruta, J. Photochem. Photobiol. A Chem. 89 (1995) 177.
[5] J.E. Yoo, K. Lee, A. Tighineanu, P. Schmuki, Electrochem. Commun. 34 (2013) 177.
[6] J.E. Yoo, K. Lee, P. Schmuki, Electrochem. Commun. 34 (2013) 351.
[7] S. Ono, M. Saito, H. Asoh, Electrochim. Acta 51 (2005) 827.
[8] K.R. Hebert, S.P. Albu, I. Paramasivam, P. Schmuki, Nat. Mater. 11 (2012) 162.
[9] S. Hong, T. Kang, D. Choi, Y. Choi, L.P. Lee, ACS Nano 6 (2012) 5803.
[10] C.V. Thompson, Annu. Rev. Mater. Res. 42 (2012) 399.
[11] Z.Q. Liu, W.Y. Zhou, L.F. Sun, D.S. Tang, X.P. Zou, Y.B. Li, C.Y. Wang, G. Wang, S.S. Xie, Chem. Phys. Lett. 341 (2001) 523.
[12] D. Wang, P. Schaaf, J. Mater. Sci. 47 (2012) 1605.
[13] M. Humenik Jr., W.D. Kingery, J. Am. Ceram. Soc. 37 (1954) 18.
[14] Z. Jiang, W. Zhang, L. Jin, X. Yang, F. Xu, J. Zhu, W. Huang, J. Phys. Chem. C 111 (2007) 12434.

[15] S. Berger, J. Kunze, P. Schmuki, A.T. Valota, D.J. Leclere, P. Skeldon, G.E. Thompson, J. Electrochem. Soc. 157 (2010) C18.
[16] J.M. Macak, P. Schmuki, Electrochim. Acta 52 (2006) 1258.
[17] J.M. Macak, S.P. Albu, P. Schmuki, Phys. Status Solidi RRL 1(2007) 181.
[18] S. Bauer, J. Park, J. Faltenbacher, S. Berger, K.V.D Mark, P. Schmuki, Integr. Biol. 1 (2009) 525.

Final Remarks

Metal/noble metal decoration, doping and nanostructuring of TiO_2 represent successful strategies to effectively limit the detrimental charge carriers recombination and trapping, hence allowing an overall enhancement of the photocatalysts performance.

The metal and noble metal nanoparticles deposited at the TiO_2 surface act as sink of conduction band electrons. This phenomenon not only leads to metal/semiconductor systems exhibiting advanced reduction ability (*i.e.*, higher efficiency in H_2 production), but also improves their oxidation power, as demonstrated in methanol and formic acid photocatalytic mineralization, and in ammonia photocatalytic oxidation. Particularly in the case of ammonia, the presence of a certain metal on TiO_2, with a certain loading, can precisely drive the reaction through a specific pathway rather than through others. In other words, photocatalysis can be exploited also in selective oxidation/reduction reactions, upon a precise tuning of the photocatalyst and co-catalyst properties.

The efficiency of charge carriers separation can be improved also by doping TiO_2 with other transition metals. In the case of Ta-doping, a better photocatalytic performance is attained because of increased electron conductivity. Therefore, this strategy appears extremely promising in view of photo-electrochemical applications, such as dye-sensitized solar cells and photo-electrochemical water splitting.

The nanostructuring of TiO_2 leads to materials with high specific surface area, which implies higher amounts of active sites for adsorption of reactant molecules and wider surface for light absorption. Nevertheless, especially from a photo-electrochemical point of view, one-dimensional nano-structured materials exhibit preferential pathways for charge carriers separation, hence leading to limited electron-hole recombination and improved photocatalytic activity.

Still concerning the nanostructuring of the semiconductor, a high level of self-ordering of TiO_2 nanotube arrays is attainable through electrochemical anodization, even when this approach is scaled up to surfaces of several tens of cm^2. Nevertheless, anodization of Ti-based alloys is a straightforward method to couple nanostructuring of TiO_2 and its chemical modification. A wide range of transition metals can be embedded within the TiO_2 lattice, giving to TiO_2 nanotubes specific properties and functionalities. Yet, when

the alloys contain a noble metal, TiO_2 nanotubes result decorated with highly dispersed noble metal nanoparticles. Key strengths concerning the anodization of Ti-based alloys are that *i)* the concentration of the dopant or noble metal within/on the nanotubes is simply and finely controlled by tuning its content in the alloy and *ii)* the resulting doping or noble metal nanoparticles deposition is extremely homogeneous.

Therefore, electrochemical anodization represents a simple and effective approach to attain highly ordered one-dimensional TiO_2 nanostructures, well attached on a conductive substrate and ready to be used either as photocatalytic thin film material (for which no specific separation treatment from the reaction media is needed) or as photo-anode in a photo-electrochemical set-up.

Abbreviations & Symbols

Acronyms

AOP	Advanced oxidation process.
BE	Binding energy / XPS analysis.
BET	Brunauer-Emmet-Teller theory / BET analysis.
BJH	Barrett-Joyner-Halenda / BET analysis.
CO	Compact (anodic) oxide layer.
DCPV	Desorption cumulative pore volume / BET analysis.
DR	Diffuse reflectance / optical absorption.
DSSC	Dye Sensitized Solar Cells / Grätzel type solar cells.
EDX	Energy dispersive X-ray spectroscopy.
EP	Electropolishing / electropolished substrate.
ESR	Electron spin resonance spectroscopy.
FA	Formic acid / HCOOH / HCO_2H.
FFT	Fast Fourier transform.
G	Gold reflections (XRD).
HAADF	High angle annular dark field / HAADF-STEM.
HR	High resolution / HRTEM.
ICP-OES	Inductively coupled plasma optical emission spectrometry.
IPCE	Incident photon to current conversion efficiency.
MO	Metal oxide(s).
NC	(metal) Nanocluster(s).
NM	Noble metal(s) / Gold / Palladium / Platinum.
NP	(metal) Nanoparticle(s).
NT	Nanotubes / TiO_2 nanotubes arrays.
OCV	Open circuit voltage.
PEC	Photo-electrochemical.
PO	Porous (anodic) oxide layer.
PVD	Physical vapor deposition.
SAD	Selected area (electron) diffraction analysis.
SEM	Scanning electron microscopy.
SHE	Standard hydrogen electrode / reference electrode / NHE.
SPR	Surface plasmon resonance / Au/TiO_2.
SSA	Specific surface area (determined by BET analysis).
STEM	Scanning transmission electron microscopy.
T	Titanium reflections (XRD).

TEM Transmission electron microscopy.
TOF-SIMS Time of flight – secondary ion mass spectrometry.
UV Ultraviolet light / electromagnetic radiation.
Vis Visible light / electromagnetic radiation.
XPS X-ray photoelectron spectroscopy.
XRD X-ray diffraction.

Roman Letters, Symbols & Abbreviations

1D One-dimensional structure / nanotube-like architecture.
A Anatase / XRD peak / TiO_2 crystallographic phase / active area.
B Brookite / XRD peak / TiO_2 crystallographic phase.
CB Conduction band / edge or potential of the conduction band.
d Thickness of the anodic oxide film.
D Deviation parameter / Crystallographic preferential orientation.
e^- Electron / photogenerated electron.
E Energy / electrochemical potential.
E_G Band gap energy.
f Growth factor of the anodic oxide.
F Electric field / driving force for solid-state diffusion of ions.
g Tensor value / electron spin resonance.
h Planck's constant.
h^+ Hole / photogenerated hole.
I Intensity of a signal / electric current / irradiation intensity.
J Current density / current intensity normalized *vs.* the active area.
k^0 Zero-order rate constant / kinetic of formic acid degradation.
m Atomic mass or molecular weight (g mol^{-1}).
M Metal atom.
M^{n+} Metal cation.
n Moles.
p Pressure or partial pressure.
P Power / power density of light irradiation.
r Rate of a given reaction / production rate.
R Rutile / XRD peak / TiO_2 crystallographic phase.
S Selectivity (%).
t Time / anodization time / irradiation time.
U Applied voltage / potential.
U_p Threshold voltage for anodic oxide formation.
VB Valence band / edge, position or potential of the valence band.

x	Molar fraction.
X	Conversion (%) / photocatalytic conversion of ammonia.
z	Charge of a species.

Greek Letters

α	Refers to Kα radiation / XPS / XRD.
Δ	Difference of two values.
θ	Angle / XRD.
λ	Wavelength / electromagnetic wave.
υ	Frequency / electromagnetic wave.
φ	Work function.
Φ	Apparent photon efficiency.

List of Publications

(Status of December 2013)

1. A. Palacios-Padrós, **M. Altomare**, A. Tighineanu, R. Kirchgeorg, N.K. Shrestha, I. Díez-Pérez, F. Caballero-Briones, F. Sanz and P. Schmuki, *"Growth of ordered anodic SnO_2 nanochannel layers and their use for H_2 gas-sensing"*, J. Mater. Chem. A **(2013)** accepted**.**

2. K. Lee, R. Hahn, **M. Altomare**, E. Selli and P. Schmuki, *"Intrinsic Au Decoration of Growing TiO_2 Nanotubes and Formation of a High-Efficiency Photocatalyst for H_2 Production"*, Adv. Mater. 25 **(2013)** 6133.

3. J.E. Yoo, K. Lee, **M. Altomare**, E. Selli and P. Schmuki, *"Self-Organized Arrays of Single-Metal Catalyst Particles in TiO_2 Cavities: A Highly Efficient Photocatalytic System"*, Angew. Chem. Int. Ed. 52 **(2013)** 7514.

4. **M. Altomare**, K. Lee, M.S. Killian, E. Selli and P. Schmuki, *"Ta-Doped TiO_2 Nanotubes for Enhanced Solar-Light Photoelectrochemical Water Splitting"*, Chem. Eur. J. 19 **(2013)** 5841.

5. N. Liu, H. Mirabolghasemi, K. Lee, S.P. Albu, A. Tighineanu, **M. Altomare** and P. Schmuki, *"Anodic TiO_2 nanotubes: Double Walled vs. Single Walled"*, Farad. Discuss. DOI: 10.1039/C3FD00020F **(2013)**.

6. **M. Altomare**, M. Pozzi, M. Allieta, L.G. Bettini and E. Selli, *"H_2 and O_2 photocatalytic production on TiO_2 nanotube arrays: Effect of the anodization time on structural features and photoactivity"*, Appl. Catal. B Environ. 136-137 **(2013)** 81.

7. A. Naldoni, M. D'Arienzo, **M. Altomare**, M. Marelli, R. Scotti, F. Morazzoni, E. Selli and V. Dal Santo, *"Pt and Au/TiO_2 photocatalysts for methanol reforming: Role of metal nanoparticles in tuning charge trapping properties and photoefficiency"*, Appl. Catal. B Environ. 130-131 **(2013)** 239.

8. **M. Altomare** and E. Selli, *"Effects of metal nanoparticles deposition on the photocatalytic oxidation of ammonia in TiO_2 aqueous suspensions"*, Catal. Today 209 **(2013)** 127.

9. M.V. Dozzi, A. Saccomanni, **M. Altomare** and E. Selli, *"Photocatalytic activity of NH_4F-doped TiO_2 modified by noble metal nanoparticle deposition"*, Photochem. Photobiol. Sci. 12 **(2013)** 595.

10. **M. Altomare**, G.L. Chiarello, A. Costa, M. Guarino and E. Selli, *"Photocatalytic abatement of ammonia in nitrogen-containing effluents"*, Chem. Eng. J. 191 **(2012)** 394.